

Biomechanical and microstructural characterization of porcine smooth muscle properties

*Von der Fakultät für Wirtschafts- und Sozialwissenschaften der Universität
Stuttgart zur Erlangung des akademischen Grades eines Doktors der
Philosophie (Dr. phil.) genehmigte Abhandlung*

vorgelegt von

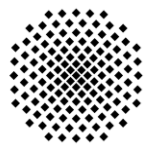
Mischa Borsdorf

Aus Baden-Baden

Hauptberichter: Prof. Dr. Tobias Siebert

Mitberichter: Prof. Dr. Oliver Röhrle

Tag der mündlichen Prüfung: 25.04.2022



Universität Stuttgart

Institut für Sport- und Bewegungswissenschaft

Abteilung für Bewegungs- und Trainingswissenschaft

2022

Abstract

Along with skeletal- and cardiac muscle, smooth muscle is one of the three muscle types within our body. Predominantly located in the walls of internal organs, smooth muscle tissue transports various contents across the body and regulates the inner pressure of the organs. Without our ability to control them voluntarily, smooth muscles autonomously ensure an effective operation of various vital body functions. They display unique structural, mechanical, metabolic, and regulatory features to be perfectly adapted to their specific tasks within the diverse body systems. The malfunctioning of smooth muscles may disturb the corresponding body function and consequently cause various health problems. With a more holistic and comprehensive understanding of smooth muscle structure and function, diseases and dysfunctions may be better prevented and their medical treatments may be improved and optimized. Hence, smooth muscle tissue represents a fascinating and highly valuable research topic from both a physiological and medical point of view.

The present thesis focuses on porcine smooth muscle tissue from the stomach and the urinary bladder, two central and essential organs of the gastrointestinal- and urinary system, respectively. Due to the same diet and structural similarities, the pig stomach is a suitable model to better understand the functional mechanisms of the human stomach. This thesis includes three studies built upon *in vitro* uniaxial tensile experiments and histological investigations of smooth muscle tissue strips, examining biomechanical and microstructural characteristics, respectively. The aim is to contribute to the state of knowledge about smooth muscles in general, to derive logical conclusions about the motility of the stomach and urinary bladder, and to acquire valuable input data for the development and validation of realistic, three-dimensional organ models.

Chapter 1 introduces the relevant context of the present thesis to facilitate a thematic entrance to the studies. The general introduction includes physiological background information about smooth muscle tissue, the stomach, and the bladder and an overview of the characteristic methodology of determining smooth muscle properties. Furthermore, the research questions and aims of the individual studies are presented.

In **Chapter 2**, the pig's urinary bladder was examined for locational and directional differences of smooth muscle properties. Investigations were conducted on smooth muscle strips from 6

locations (apex vs. body vs. trigone; ventral vs. dorsal) and 2 directions (longitudinal vs. circumferential orientation). The examined biomechanical (n=96) and microstructural (n=36) properties included the force-length- and force-velocity relationship, and the smooth muscle content and fiber orientation, respectively. The results showed that the maximum active stress of the bladder strips is higher in the longitudinal compared to the circumferential direction. This was in line with the histological investigation showing a higher smooth muscle content in the bladder strips in the longitudinal direction. However, normalization of maximum strip force by the cross-sectional area of smooth muscle fibers yielded similar smooth muscle maximum stresses (165.4 ± 29.6 kPa), independent of strip direction. Active muscle properties showed no locational differences. The trigone exhibited higher passive stress than the body. Moreover, the bladder exhibited greater passive stress in the longitudinal than the circumferential direction, which might be attributed to its microstructure (more longitudinal arrangement of muscle fibers).

In **Chapter 3**, layer-specific and direction-dependent model parameters for the active and passive stress-stretch characteristics of the stomach wall were experimentally determined using porcine smooth muscle strips. These were integrated into a proposed computational, three-dimensional model of the stomach, illustrating the excitation-contraction coupling on a whole organ level. The electrical activation of the smooth muscle cells (SMC) due to the pacemaker activity of the interstitial cells of Cajal (ICC) was modeled by using FitzHugh-Nagumo-type equations, which simulate the typical ICC and SMC slow wave behavior. The calcium dynamic in the SMC depends on the SMC membrane potential via a gaussian function, while the chemo-mechanical coupling in the SMC was modeled via an extended Hai-Murphy model. This cascade is coupled with an additional mechano-electrical feedback-mechanism, taking into account the mechanical response of the ICC and SMC due to the stretch of the stomach wall. In this way, the relaxation responses of the fundus to accommodate incoming food, as well as the typical peristaltic contraction waves in the antrum for mixing and transport of the chyme, have been well replicated in simulations performed at the whole organ level.

The study reported in **Chapter 4** examines whether the characteristic smooth muscle strip composition of multiple muscle layers influences the muscle properties in uniaxial tensile experiments, compared to strips that featured only one muscle layer. Uniaxial tensile experiments

are a standard method to determine the contractile properties of smooth muscles. Smooth muscle strips from organs of the urogenital- and gastrointestinal tract contain multiple muscle layers with different muscle fiber orientations, which are frequently not separated for the experiments. During strip activation, these muscle fibers contract in deviant orientations from the force-measuring axis, affecting the biomechanical characteristics of the tissue strips. This study aimed to investigate the influence of muscle layer separation on the determination of smooth muscle properties. Smooth muscle strips, consisting of longitudinal and circumferential muscle layers (whole-muscle strips [WMS]) and smooth muscle strips, consisting of only the circumferential muscle layer (separated layer strips [SLS]), have been prepared from the fundus of the porcine stomach. Strips were mounted with muscle fibers of the circumferential layer in line with the force-measuring axis of the uniaxial testing set-up. The force-length- (FLR) and force-velocity relationship (FVR) were determined through a series of isometric and isotonic contractions, respectively. Muscle layer separation revealed no changes in the FLR. However, the SLS exhibited a higher maximal shortening velocity and a lower curvature factor than WMS. During WMS activation, the transversally oriented muscle fibers of the longitudinal layer shortened, resulting in a narrowing of this layer. Expecting volume constancy of muscle tissue, this narrowing led to a lengthening of the longitudinal layer, which counteracted the shortening of the circumferential layer during isotonic contractions. Consequently, the shortening velocities of the WMS were decreased significantly. This effect was stronger at high shortening velocities.

Chapter 5 gives a general conclusion to the conducted studies and puts the acquired knowledge into a greater context. On the one hand, the differences in the methodology of the individual studies are elucidated and explained; on the other hand, the added value to our current understanding of smooth muscles, the stomach, and the urinary bladder is reviewed. Based on the yielded data and results of the studies, comparisons are made between the stomach and bladder's structure and function. Lastly, future prospects are discussed by proposing approaches to further improve our knowledge about smooth muscle physiology and suggest which investigations on the stomach and urinary bladder could be highly valuable for developing and extending new and current organ models, respectively.

Zusammenfassung

Neben Skelett- und Herzmuskulatur stellt glatte Muskulatur eine der drei Muskeltypen in unserem Körper dar. Überwiegend befindlich in den Wänden von inneren Organen transportiert glattes Muskelgewebe mehrere Inhalte durch den Körper und reguliert den inneren Druck der Organe. Ohne dass wir sie bewusst kontrollieren können, ermöglichen glatte Muskeln autonom einen effektiven Ablauf verschiedener lebenswichtigen Körperfunktionen. Sie zeigen außergewöhnliche strukturelle, mechanische, metabolische und regulatorische Eigenschaften, um ideal an die spezifischen Aufgaben der unterschiedlichen Körpersysteme angepasst zu sein. Eine abnormale Arbeitsweise von glatten Muskeln kann zu Störungen der betroffenen Körperfunktion führen und somit verschiedene Gesundheitsprobleme verursachen. Mit einem ganzheitlicheren und umfassenderen Verständnis der Struktur und Funktion von glatter Muskulatur könnten Krankheiten und Dysfunktionen besser verhindert werden, wie auch deren medizinische Behandlung verbessert und optimiert werden. Damit stellt glattes Muskelgewebe aus physiologischer und medizinischer Sicht ein faszinierendes und hoch wertvolles Forschungsthema dar.

Der Fokus der vorliegenden Thesis liegt auf glatter Muskulatur des Magens und der Harnblase, zwei zentrale und essentielle Organe des Gastrointestinal- bzw. des Urogenitalsystems. Aufgrund der gleichen Ernährung sowie struktureller Gemeinsamkeiten ist der Schweinemagen ein geeignetes Modell um die Funktionsmechanismen des menschlichen Magens besser zu verstehen. Diese Thesis umfasst drei Studien, welche auf *in vitro* uniaxialen Spannungsexperimenten und histologischen Untersuchungen beruhen, durch welche biomechanische bzw. mikrostrukturelle Eigenschaften bestimmt wurden. Ziel ist es, generell zum Wissensstand von glatten Muskeln beizutragen, logische Schlussfolgerungen über die Motilität des Magens und der Blase abzuleiten, und wertvolle Daten zur Entwicklung und Validierung von realistischen, drei-dimensionalen Organmodellen zu erheben.

Kapitel 1 stellt den relevanten Kontext der vorliegenden Thesis vor, um einen thematischen Zugang zu den Studien zu ermöglichen. Die allgemeine Einleitung beinhaltet Hintergrundinformation über die Physiologie von glattem Muskelgewebe, des Magens und der

Blase, wie auch einen Überblick darüber, mit welcher Methodik die Eigenschaften von glatten Muskeln typischerweise erhoben werden. Weiterhin werden die Forschungsfragen und Ziele der einzelnen Studien vorgestellt.

In **Kapitel 2** wurde die Harnblase vom Schwein darauf untersucht, ob Lokalitäts- und Richtungsunterschiede der Eigenschaften der glatten Muskulatur bestehen. Dazu wurden glatte Muskelstreifen von 6 Regionen (Apex vs. Körper vs. Trigon) und 2 Richtungen (longitudinal vs. umlaufend) untersucht. Die analysierten biomechanischen (n=96) Eigenschaften umfassten die Kraft-Längen- und Kraft-Geschwindigkeitskurve, während die mikrostrukturellen (n=36) Eigenschaften den Anteil glatten Muskelgewebes und die Faserorientierung beinhalteten. Die Ergebnisse zeigten, dass die maximale Spannung der Blasenstreifen höher in der longitudinalen Richtung war, im Vergleich zu der umlaufenden Richtung. Dies stimmte mit den histologischen Untersuchungen ein, welche einen höheren glatten Muskelanteil in den Streifen in longitudinaler Richtung ergaben. Die Normierung der maximalen Kraft der Streifen nach dem Querschnitt der glatten Muskelfasern hingegen resultierte in ähnlichen maximalen Spannungen (165.4 ± 29.6 kPa), unabhängig von der Orientierung der Streifen. Die aktiven Muskeleigenschaften zeigten keine lokalen Unterschiede. Das Trigon zeigte höhere passive Spannung als der Körper. Weiterhin zeigte die Blase größere passive Spannung in der longitudinalen als in der umlaufenden Richtung, was durch die Mikrostruktur begründet werden kann (überwiegende Ausrichtung der Muskelfasern in longitudinaler Richtung).

In **Kapitel 3** wurden an glatten Muskelstreifen vom Schwein schicht-spezifische und richtungsabhängige Modell-Parameter experimentell bestimmt, um die aktive und passive Spannungs-Dehnungseigenschaften der Magenwand zu charakterisieren. Diese wurden in ein erstelltes drei-dimensionales Computermodell des Magens integriert, welches die Erregungs-Kontraktions-Kopplung auf einem Gesamtorganlevel illustriert. Die elektrische Aktivierung von glatten Muskelzellen (smooth muscle cells [SMC]), was auf die Schrittmacher Aktivität der interstitiellen Zellen von Cajal (interstitial cells of Cajal [ICC]) basiert, wurde durch Gleichungen des FitzHugh-Nagumo-Modells modelliert, welche das typische Verhalten der sogenannten „langsamen Wellen“ („slow waves“) der ICC und SMC simulieren. Die Kalziumdynamik in den SMC ist abhängig vom Membranpotential über eine Gaußsche Funktion, während das chemo-

mechanische Koppeln in den SMC über ein erweitertes Hai-Murphy Model modelliert wurde. Diese Abfolge ist gekoppelt mit einem zusätzlichen mechano-elektrischen Feedbackmechanismus, welcher die mechanische Antwort der ICC und SMC durch Dehnung der Magenwand miteinbezieht. Dadurch wurde in den Simulationen auf Gesamtorganlevel gut repliziert, wie die Relaxationsantworten im Fundus zur Nahrungsaufnahme, und wie die typische peristaltischen Kontraktionswellen im Antrum zum Mixen und Transport des Speisebreis ablaufen.

In der Studie in **Kapitel 4** wurde untersucht, ob die typische Zusammensetzung von glatten Muskelstreifen aus mehreren Muskelschichten die Muskeleigenschaften in uniaxialen Experimenten beeinflusst im Vergleich zu Streifen, die nur eine einzige Muskelschicht beinhalten. Uniaxiale Spannungsexperimente sind eine Standard Methode zur Bestimmung kontraktiver Eigenschaften von glatten Muskeln. Glatte Muskelstreifen von Organen des Urogenital- und Gastrointestinaltrakts beinhalten mehrere Muskelschichten von unterschiedlicher Faserorientierung, welche oft für Experimente nicht getrennt werden. Während der Aktivierung der Streifen kontrahieren diese Muskelfasern in abweichende Richtungen der Kraftmessachse, was die biomechanischen Eigenschaften der Gewebestreifen beeinflusst. Diese Studie zielte darauf ab, den Einfluss der Muskelschichttrennung auf die Bestimmung von glatten Muskeleigenschaften zu untersuchen. Glatte Muskelstreifen, bestehend aus longitudinaler und umlaufender Muskelschicht (Gesamtmuskel Streifen; whole-muscle strips [WMS]) und Streifen bestehend aus nur der umlaufenden Muskelschicht (Getrennte-Schicht Streifen; separated layer strips [SLS]) wurden vom Fundus des Schweinemagens präpariert. Die Streifen wurden so in einen uniaxialen Aufbau eingehängt, damit die umlaufenden Muskelfasern entlang der Kraftmessachse verliefen. Die Kraft-Längen- und Kraft-Geschwindigkeits-Relation wurden durch mehrere isometrische bzw. isotonische Kontraktionen bestimmt. Die Muskelschichttrennung ergab keine Veränderung in der Kraft-Längen Relation. Allerdings zeigten SLS eine höhere maximale Verkürzungsgeschwindigkeit und einen niedrigeren Kurvenfaktor als WMS. Während der Aktivierung von WMS verkürzten sich die transversal gerichteten Muskelfasern der longitudinalen Schicht, was in einer Verengung dieser Schicht resultierte. Bei angenommener Volumenkonstanz von Muskelgewebe verursachte diese Verengung eine Verlängerung der longitudinalen Schicht, was der Verkürzung der umlaufenden Muskelschicht während isotonischen Kontraktionen

gegenwirkte. Folglich waren die Verkürzungsgeschwindigkeiten der WMS signifikant verringert. Dieser Effekt war stärker bei hohen Verkürzungsgeschwindigkeiten.

Kapitel 5 gibt eine generelle Schlussfolgerung zu den durchgeführten Studien und setzt das erworbene Wissen in einen größeren Kontext. Zum einen werden die Unterschiede der Methodologie der individuellen Studien erläutert und erklärt, zum anderen wird der Mehrwert zu unserem jetzigen Verständnis von glatten Muskeln, wie auch des Magens und der Harnblase inspiziert. Beruhend auf den erhobenen Daten und Ergebnissen der Studien werden Vergleiche zwischen der Struktur, wie auch der Funktion des Magens und der Blase gezogen. Abschließend werden Perspektiven diskutiert, indem zukünftige Ansätze vorgeschlagen werden, wie weiterhin unser Wissen über die Physiologie der glatten Muskulatur verbessert werden kann und indem Anregungen gegeben werden, welche Untersuchungen am Magen und der Blase von hohem Wert sein könnten für das Entwickeln und Erweitern von neuen bzw. aktuellen Organmodellen.

List of publications

The following publications are included in this thesis:

- I. **Borsdorf, M.**, Tomalka, A., Stutzig, N., Morales-Orcajo, E., Böl, M. & Siebert, T. Locational and directional dependencies of smooth muscle properties in pig urinary bladder. *Front. Physiol.* **10**, 63 (2019).
- II. Klemm, L., Seydewitz, R., **Borsdorf, M.**, Siebert, T. & Böl, M. On a coupled electro-chemomechanical model of gastric smooth muscle contraction. *Acta Biomater.* **109**, 163-181 (2020).
- III. **Borsdorf, M.**, Böl, M. & Siebert, T. 2021. Influence of layer separation on the determination of stomach smooth muscle properties. *Pflüger's Arch. – Eur. J. Physiol.* **473**, 911-920 (2021).

The individual publications have been formatted to fit a uniform style for this thesis.

Table of contents

Abstract	i
Zusammenfassung	iv
List of publications	viii
List of abbreviations and acronyms	xiii
List of figures	xv
List of tables	xvii
1 General introduction	18
1.1 Physiological background.....	20
1.1.1 Smooth muscles.....	21
1.1.2 The stomach	28
1.1.3 The urinary bladder	30
1.2 Methodological background.....	32
1.2.1 Experiments on biomechanical properties	32
1.2.2 Analysis of microstructural properties	34
1.3 Research questions and aims of the studies.....	35
1.3.1 Study I	35
1.3.2 Study II	36
1.3.3 Study III	37
2 Locational and directional dependencies of smooth muscle properties in pig bladder	39
2.1 Introduction	39
2.2 Materials and methods.....	42
2.2.1 Experimental set-up.....	42

2.2.2	Determination of muscle properties	43
2.2.3	Histological observation.....	44
2.2.4	Statistics	45
2.3	Results	46
2.4	Discussion.....	51
2.4.1	Detrusor muscle properties – comparison with the literature	53
2.4.2	Active urinary bladder properties – locational and directional dependencies	53
2.4.3	Passive urinary bladder properties – locational and directional dependencies ...	55
2.4.4	Functional and physiological relevance	55
2.5	Conclusion	56
2.6	Author contributions.....	57
3	On a coupled electro-chemomechanical model of gastric smooth muscle contraction	58
3.1	Introduction	58
3.2	Structural, functional, and bio-chemophysical aspects of stomach soft tissue.....	62
3.2.1	Structure of the stomach wall.....	62
3.2.2.	Gastric reservoir and antral pump - functional units of the stomach	62
3.2.3.	Electro-chemomechanical coupling process of gastric contraction	63
3.3	Materials and methods.....	68
3.3.1	Ethical approval.....	68
3.3.2	Tissue strip experiments.....	68
3.3.3	Statistics	70
3.4	Experimental results: direction-dependent, layer-specific stress responses	71
3.5	Continuum mechanical framework of gastric smooth muscle contraction	73

3.5.1	Kinematics.....	73
3.5.2	Governing equations	74
3.5.3	Constitutive equations.....	76
3.6	Results	82
3.6.1	Geometrical model of the stomach.....	84
3.6.2	Temporal evolutions of ϕ_{ICC} , ϕ_{SMC} , and Ca^{2+}	85
3.6.3	Influence of material characteristics on gastric muscle contraction	89
3.7	Discussion.....	94
3.7.1	Modeling the electro-chemomechanical contraction excitation process.....	95
3.7.2	Stomach mechanical properties.....	96
3.7.3	Functional aspects on relation to mechanical findings.....	99
3.7.4	Model limitations and outlook	99
4	Influence of layer separation on stomach smooth muscle properties	103
4.1	Introduction	103
4.2	Materials and methods.....	104
4.2.1	Experimental set-up.....	104
4.2.2	Determination of muscle properties	106
4.2.3	Histological observations	108
4.2.4	Statistics	108
4.3	Results	109
4.4	Discussion.....	112
4.4.1	Porcine smooth muscle properties – comparison with the literature	113
4.4.2	Influence of layer separation on smooth muscle properties	113

4.4.3	Relevance for studies on smooth muscle strips.....	116
4.5	Conclusion	117
5	General Conclusion.....	119
5.1	Differences in the methodology of determining smooth muscle properties.....	120
5.2	Locational and directional smooth muscle properties of the urinary bladder	122
5.3	Layer and direction dependent properties of the stomach wall	124
5.4	Uniaxial tensile experiments	125
5.5	Comparison between the stomach and bladder	126
5.6	Prospects	128
6	Bibliography	131
7	Author Contributions	152
8	Acknowledgements.....	156
9	Declaration.....	157

List of abbreviations and acronyms

Chapter 1

Abbreviation	Explanation
<i>curv</i>	curvature factor
CSA	cross-sectional area
F_{im}	maximum isometric force
FLR	force-length relationship
FVR	force-velocity relationship
ICC	interstitial cells of Cajal
L_0	optimum muscle length associated with F_{im}
MLCK	myosin light chain kinase
v_{max}	maximum shortening velocity

Chapter 2

Abbreviation	Explanation
L_S	slack length
p_{act}	maximum active stress
p_{pass}	passive stress at L_0
$SMC_{stretched}$	lengthwise stretched smooth muscle content
w_{asc}	width of the ascending limb
w_{desc}	width of the descending limb

Chapter 3

Abbreviation	Explanation
λ_{opt}	optimal muscle stretch
A_0	mean cross-sectional area
ECM	extracellular matrix
F_{max}	maximum active force
L	muscle length
P_{max}	maximum active stress
PP	plateau potential
RMP	resting membrane potential
SM	smooth muscle
SMC	smooth muscle cells
SW	stomach wall

Chapter 4

Abbreviation	Explanation
SLS	separated layer strips
WMS	whole-muscle strips

List of figures

Figure 1. Schematic organ wall samples from the stomach and the urinary bladder	21
Figure 2. Schematic depiction of a smooth muscle fiber	23
Figure 3. Representative force-length relationship of smooth muscle tissue	26
Figure 4. Representative force-velocity relationship of smooth muscle tissue	28
Figure 5. Ventral view of the porcine stomach	29
Figure 6. Ventral view of the porcine bladder	31
Figure 7. Exemplary depiction of a biomechanical characterization	33
Figure 8. Exemplary illustration of a histological analysis	34
Figure 9. Porcine urinary bladder anatomy and definition of locations	40
Figure 10. Muscle properties of longitudinal strips dissected from the dorsal body	47
Figure 11. The dependencies of muscle properties on location and direction	49
Figure 12. Direction- and region dependencies of muscle properties	49
Figure 13. Lengthwise section and cross section of a longitudinal strip	51
Figure 14. Gross anatomy of the stomach	61
Figure 15. Electro-chemomechanical and mechano-electrochemical coupling	64
Figure 16. Illustration of the membrane potentials of the ICC and SMC	67
Figure 17. Active stress-stretch responses of 10 gastric muscular tissue samples	70
Figure 18. Passive force-stretch and stress-stretch responses of 20 gastric tissue samples	72
Figure 19. Illustration of a porcine, geometric stomach model	86
Figure 20. Temporal progress of ϕ_{ICC} , ϕ_{SMC} , and Ca^{2+} at four different locations	87
Figure 21. Influence of mucosal layer's waviness on the SW mechanical behavior	90

Figure 22. Re-simulation, considering the pre-stretch of the mucosal layer	92
Figure 23. Tissue strip structure and location in the porcine stomach	105
Figure 24. Active muscle properties of whole-muscle strips and isolated layer strips	110
Figure 25. Influence of layer separation on muscle properties	111
Figure 26. Passive stress-length relationship	112
Figure 27. Schematic reconstruction of whole-muscle strips	114
Figure 28. Force-velocity relationship of whole-muscle strips and separated layer strips	115
Figure 29. Comparison of the force-velocity relationship	128

List of tables

Table 1. The number of investigated tissue samples	44
Table 2. Location dependency of muscle properties	48
Table 3. Summary of quantitative histological data	50
Table 4. Active and passive experiments conducted in this study	67
Table 5. Mechanical parameters for porcine SW tissue	83
Table 6. Material parameters for the calcium diffusion inside the SM tissue	84
Table 7. Material parameters for the electro-chemomechanical excitation	87
Table 8. Mechanical parameters of the mucosal layer	94
Table 9. The number of investigated tissue samples	107
Table 10. Influence of layer separation on the force-length relationship	109

1 General introduction

Muscles are soft, elastic tissues within the body of animals. Their main function is the muscle contraction, a complex process of force generation that enables all kind of movements of the organism. There are overall three different types of muscle tissue: skeletal-, cardiac-, and smooth muscle. All of these muscle types are crucial for survival and life in general. Skeletal muscle tissue is typically attached via tendons to the bones and is used for locomotion. Cardiac muscle tissue lies in the heart's wall and pumps blood through the vessels around the body. The subject of the present thesis are smooth muscles, which are primarily located in the walls of hollow inner organs and blood vessels. Smooth muscles, like cardiac muscle tissue, cannot be controlled voluntarily. Their autonomous contractions facilitate and regulate the movement of various contents within the body. Thereby, they are responsible for the normal and effective functioning of various vital body systems, including digestion, urination, blood circulation, reproduction, and respiration.

Each body system is characterized by a complex and distinctive way of operating. Hence, to be properly adapted for their specific tasks within the respective body system, smooth muscles display unique structural, mechanical, metabolic, and regulatory properties, which not only differ from skeletal- and cardiac muscle, but furthermore exhibit variations among each other. The physiological smooth muscle properties can be altered by disease ^{1,2}, injury ^{3,4}, or age ^{5,6}, by which malfunctions of the corresponding body functions and consequently health problems can arise. Comprehensive knowledge about the characteristic structure and function of smooth muscle tissue contributes to a deeper understanding of the body systems and improves the prevention and treatment of various dysfunctions and diseases ^{7,8}. Consequently, smooth muscle tissue represents a fascinating subject and highly valuable research topic from both a physiological and medical point of view ^{9,10}. Hence, for several decades, smooth muscles of different species and organs have been studied intensively from the tissue ¹¹⁻¹³ and cellular level ¹⁴, down to the molecular level ¹⁵. While a variety of aspects about their structure and function are thoroughly understood, there remain countless intriguing and important questions to be answered.

The stomach and the urinary bladder are two central and essential organs of their respective body system. Their walls consist of various multifunctional layers, including a mucosal, serosal, and muscular layer, which in turn features differently oriented smooth muscle fibers ^{12,16}. Hence, the stomach and urinary bladder walls constitute highly complex structures, requiring manifold research in order to fully comprehend how they function to fulfill their abundant, multifaceted tasks. Thereby, it is thrived to achieve progress in the medical treatment of these organs' diseases, which globally present serious health problems ¹⁷⁻²⁰.

The present thesis was developed as part of my work in 2 DFG-funded research projects with the aim of creating and validating a urinary bladder model (DFG SI 841/9-1, BO 3091/9-1) and a stomach model (DFG SI 841/12-1, BO 3091/18-1). The thesis focuses on active biomechanical smooth muscle properties of the stomach and urinary bladder, but also thematizes their passive mechanical- and microstructural characteristics. The aim is to advance the understanding of smooth muscles in general, as well as to put the findings in a greater context by deriving conclusions about the organs' regular functioning. Moreover, the intention is to acquire new and valuable experimental datasets, to serve as input for computational, three-dimensional organ models. These in turn enable a more realistic and holistic depiction of the whole organ and contribute to a better comprehension of these organs in health and disease and consequently advance their medical treatments.

As a prerequisite for the experiments, the smooth muscle tissue needed to be healthy and intact, as well as steadily available. Therefore, the organs of the domestic pig (*sus scrofa domesticus*) were used as subjects, as their bladder and stomach display structural and functional similarities to the respective organs of the human ²¹⁻²⁴, allowing for a valid knowledge transfer between species. Furthermore, these organs have related functions ^{25,26} and consist of a similar wall composition ^{12,16}, which enables insightful comparisons between them.

Chapters 2-4 each presents a scientific publication featuring *in vitro* experiments on tissue strips from either the stomach or urinary bladder. Investigating biomechanical and microstructural properties, the individual objectives were

- I. to examine whether the bladder exhibits different smooth muscle properties among its locations and orientations (**Chapter 2**),
- II. to determine layer-specific and orientation-dependent mechanical characteristics of the stomach wall, to be integrated into a proposed computational stomach model (**Chapter 3**), and
- III. to examine whether the commonly used method of determining smooth muscle properties through uniaxial tensile tests is dependent on the separation of the tissue strip's differently oriented muscle layers (**Chapter 4**).

Chapter 5 follows with a general conclusion in which the findings from the present thesis are reported and put into a greater context. The implications on organ modeling and the medical relevance are discussed. Moreover, the methods of the studies are reviewed, and the organs are compared to each other. Lastly, future prospects regarding the investigation of smooth muscle properties and organ biomechanics are analyzed.

1.1 Physiological background

Muscles are categorized as either striated (skeletal- and cardiac muscle) or non-striated (smooth muscle), as well as either under voluntary (skeletal muscles) or involuntary control (cardiac- and smooth muscle). The stomach and the urinary bladder are both lined by smooth muscle tissue, which acts as a motor for all their movements. They feature a similar wall composition (**Figure 1**) and share the function of storing and periodically emptying their respective content. However, the stomach has the additional task of digesting its content ²⁷, by which these organs operate in a distinct way. Due to the unique and multifaceted characteristics of smooth muscles, the bladder and stomach are able to fluently function and fulfill their tasks within their respective body systems.

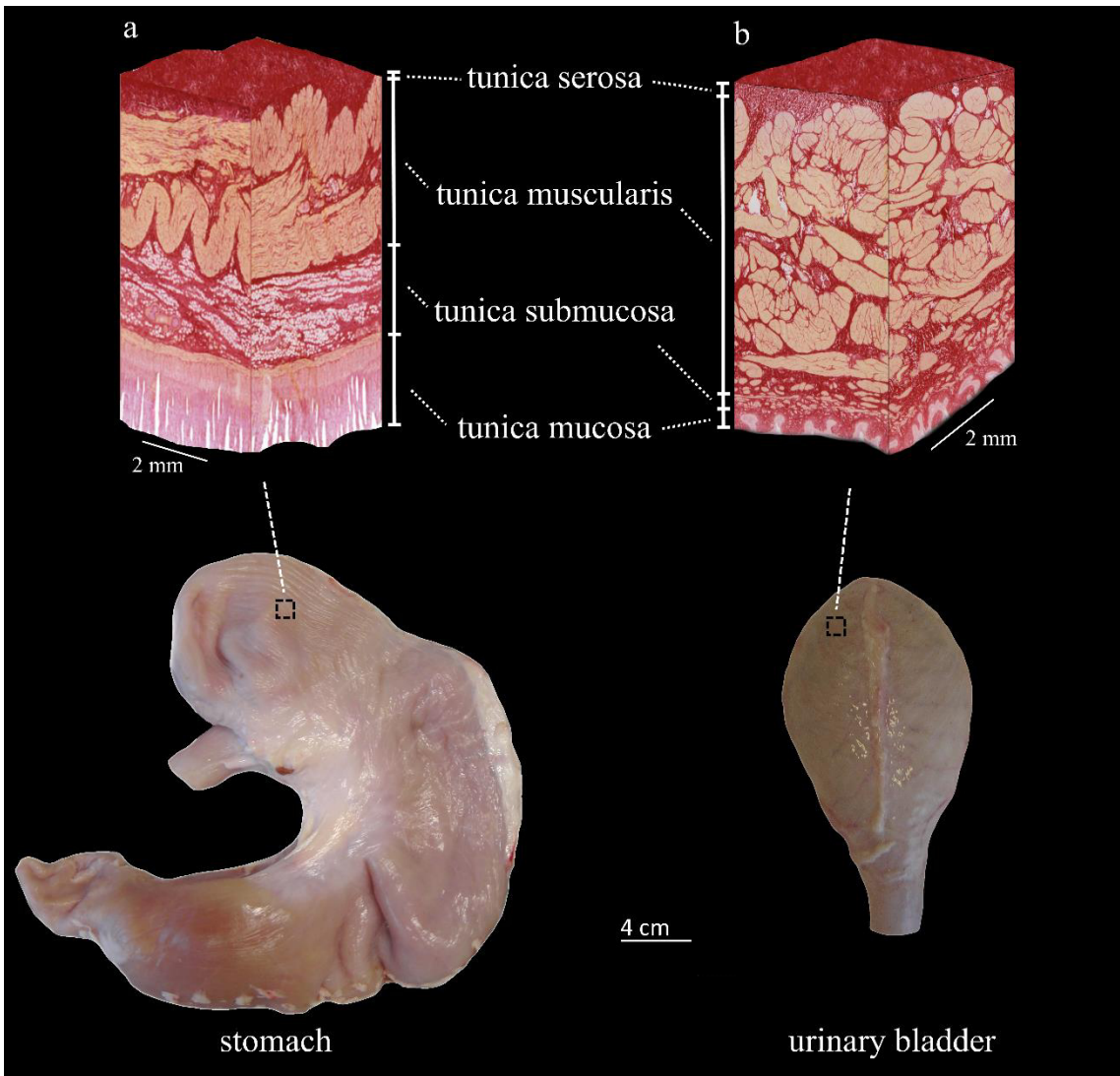


Figure 1. Schematic organ wall samples from the stomach (a) and the urinary bladder (b). The stomach wall sample is from Bauer et al. (2020) ¹⁶, reproduced with permission from Elsevier.

1.1.1 Smooth muscles

Smooth muscle tissue is named after its smooth appearance under a light microscope, opposed to skeletal- and cardiac muscles, in which striations are visible due to their orderly arrangement in sarcomeres. Smooth muscles are an aggregation of smooth muscle fibers, mechanically connected via intercellular junctions and embedded in an extracellular matrix of collagenous connective tissue. Organized in either bundles or layers, smooth muscle tissue is predominantly located in the

walls of hollow organs from the gastrointestinal-, urogenital- and respiratory system and in the walls of blood vessels.

Among their main tasks are

- (1) the transportation of solid and liquid materials through rhythmic, transient contractions (e.g., propelling the ingested food along the digestive tract),
- (2) the ejection of contents out of organs through rapid, coordinated contractions (e.g., expelling the urine out of the bladder),
- (3) the control of the inner pressure and diameter of tubelike organs through slow, sustained contractions (e.g., regulating the blood flow through the vessels),
- (4) the maintained closing of natural passageways through constant contractions, while only temporary relaxations allow contents to pass (e.g., by the urethral sphincter to keep the urine in the bladder).

Due to these distinct functions, individual smooth muscles display certain differences in structural biomechanical, regulatory, and metabolic properties. Nevertheless, on a cellular level, they exhibit a consistent cytoskeletal structure and contraction mechanism.

Smooth muscle cells

Smooth muscle fibers are slender, spindle-shaped cells with a single nucleus (**Figure 2a**). They vary in length between 50-400 μm and in diameter between 2-10 μm ²⁸. Each fiber contains a diagonal, web-like contractile machinery, consisting of the dense bodies and intermediate filaments as the structural components, as well as the thin actin- and thick myosin filaments as the contractile components. The dense bodies are either fastened to the sarcolemma or dispersed throughout the sarcoplasm, held by a framework of intermediate filaments. Analogous to the z-discs in striated muscles, the dense bodies mainly consist of the protein α -actinin and function as anchoring sites for the actin filaments. The myosin filaments are situated parallelly between the actin filaments to form together with the dense bodies the contractile units. In contrast to

sarcomeres in striated muscles, the contractile units in smooth muscles are not aligned in an orderly pattern but rather arranged in a lattice, oblique to the lengthwise axis of the fiber.

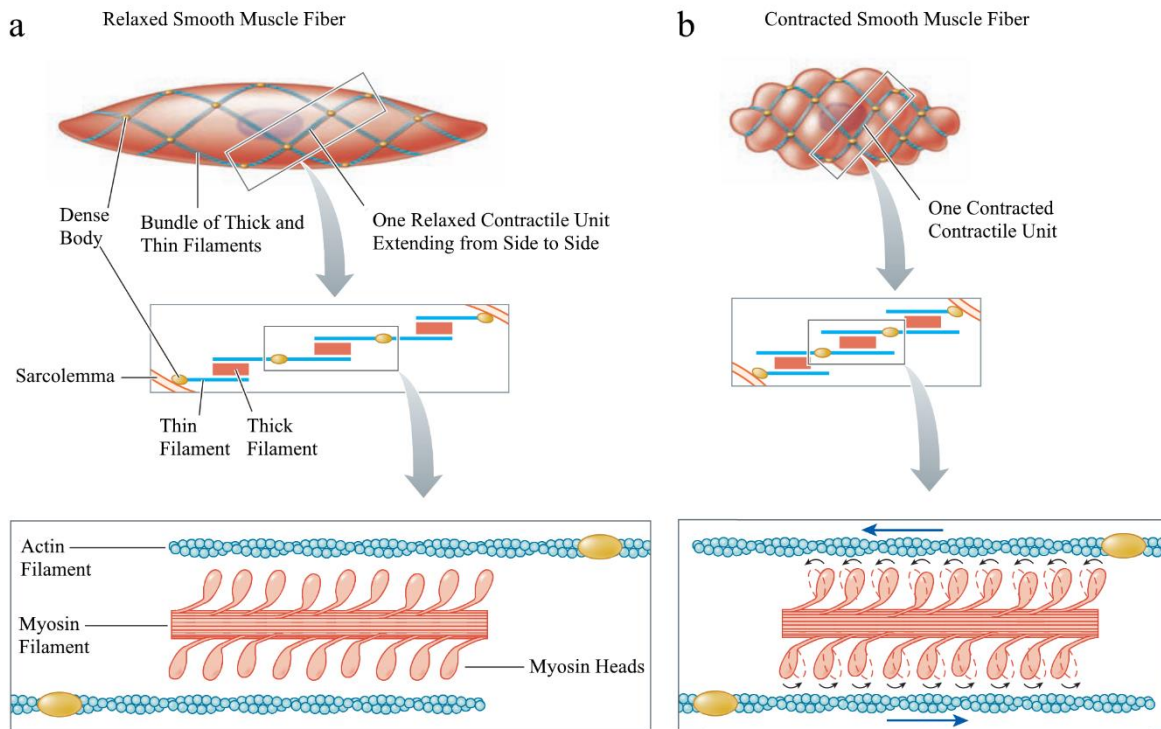


Figure 2. Schematic depiction of a smooth muscle fiber in a relaxed (a) and a contracted (b) state. Figure adapted and edited from Sherwood (2016) ²⁸, reproduced with permission from Cengage Learning.

The myosin filaments contain myosin heads, which extend to the surrounding actin filaments. Each myosin head has an actin binding site, which enables the formation of cross-bridges between the myofilaments, and an ATP-binding site, by which chemical energy can be transformed into mechanical work. When phosphorylated, the cross-bridges are able to perform so-called power strokes, pulling on the actin filaments and consequently shortening the muscle cell (**Figure 2b**). Unlike in striated muscles, the myosin heads are organized along the entire myosin filament and do not contain a central bare zone ²⁹. Furthermore, the myosin heads pull in the same direction along one side of the myosin and in the opposite direction along the other side, termed side-polarity ^{29,30}.

The contraction triggering Ca^{2+} is stored to a small extent in the sarcoplasmic reticula, as they are rather poorly developed in smooth muscle cells. Therefore, small invaginations, called

caveolae, are located along the sarcolemma, by which an influx of Ca^{2+} from the extracellular fluid is facilitated ³¹.

Smooth muscle contraction

Similar to striated muscles, the contraction mechanism of smooth muscles can be described by the cross-bridge theory ³² and the sliding filament theory ^{33,34}, whereas the excitation process underlies different principles. An increase in the cytosolic Ca^{2+} level initiates the contraction process. The Ca^{2+} binds with the regulatory protein calmodulin, which in turn activates the enzyme myosin light chain kinase (MLCK). Subsequently, the MLCK uses ATP to phosphorylate the myosin cross-bridges, which then perform power strokes ³². Through cyclic attaching and reattaching, with each cycle requiring one ATP molecule, the actin filaments are pulled along the myosin filaments ^{33,34}. Thereby, the dense bodies are moved towards each other, causing the smooth muscle fiber to generate force and to shorten. Muscle relaxation is realized by transporting Ca^{2+} back into the sarcoplasmic reticula or out of the cell, while the enzyme myosin phosphatase dephosphorylates the myosin cross-bridges.

The ATPase activity, and hence the contraction velocity of smooth muscle, is considerably lower compared to skeletal muscle. However, as their contractions consequently have a lower energy consumption, smooth muscles are in turn able to contract and maintain tone for longer periods of time. Based on their contractile kinetics, smooth muscle tissue is further classified as either phasic or tonic ³⁵. Whereas phasic contractions are fast and transient, tonic contractions are slow and tone maintaining. The peristalsis, which propels contents forward in the gastrointestinal tract, is a typical example for phasic contractions. In contrast, the smooth muscles in blood vessels characteristically contract tonically, maintaining pressure over prolonged periods of time and thereby controlling the diameter of the vessels to regulate the blood flow. This difference in contractile behavior can be mainly attributed to the specific expression of diverse myosin isoforms ³⁶ and the contrast in ATPase activity ³⁷.

Smooth muscle control

Smooth muscles are innervated by the autonomic nervous system and hence cannot be controlled voluntarily. The increase in cytosolic Ca^{2+} level and thereby the contraction of a smooth muscle fiber is initiated through membrane depolarization via neurotransmitters or hormones but can also be triggered by a mechanical stretch of the muscle cell³⁸. Smooth muscle tissue is distinguished between multi-unit and single-unit (also called visceral-) type. Multi-unit smooth muscles consist of fibers that are stimulated individually by single nerve endings. However, the fibers of single-unit smooth muscles are interconnected by gap junctions, forming an electrically coupled network called syncytium. Via these gap junctions, an action potential is transmitted between adjacent fibers, which ultimately causes a uniform contraction of the smooth muscle tissue. While multi-unit smooth muscles can be found in the eye or in the walls of large arteries, single-unit smooth muscles are more prevalent, as they are located in the walls of small blood vessels and of the hollow inner organs, except for the heart. Multi-unit smooth muscle contractions are exclusively activated through nervous stimulation (neurogenic). In contrast, single-unit smooth muscles can exhibit spontaneous contractions without any external nervous stimulation (myogenic). Non-muscular pacemaker cells, named interstitial cells of Cajal (ICC), initiate rhythmic oscillations (slow-waves) in the membrane potential of smooth muscle fibers^{39,40}. When reaching a membrane threshold potential either through additional neural or mechanical stimuli, an action potential is triggered and propagated, causing the muscle to contract. For example, in the gastrointestinal tract, the automatism of the rhythmic, peristaltic contractions underlies regular alternations between polarization and depolarization, initiated by mechanical stretches from the ingested and transported food.

Force-length relationship

A typical feature of muscles is the force-length relationship (FLR) (**Figure 3**), which describes the muscle's capacity to generate active and passive force in dependence of its length. The active FLR follows a typical bell-shaped course of the generated isometric force with an increase of

muscle length, characterized by a linear ascending limb, a force plateau, and a linear descending limb. The passive FLR typically follows a course resembling an exponential increase.

The active FLR is found in all muscle types and can be partly ascribed to the overlap between myosin and actin filaments⁴¹. At optimum muscle length (L_o), the myofilaments overlap optimally and the muscle generates its maximum isometric force (F_{im}). With longer muscle length, the myofilaments are pulled away from each other and the overlap decreases, resulting in a decline in isometric force generation. However, the decrease of force with shorter muscle length is not as clear. It has been proposed that the myosin filament spans the entire distance between two dense bodies, and with muscle shortening, the myofilament overlap decreases⁴². It has also been suggested that with shorter length, the contractile units become less aligned to the longitudinal axis of the cell and thereby transmit less force along the muscle fiber direction⁴³.

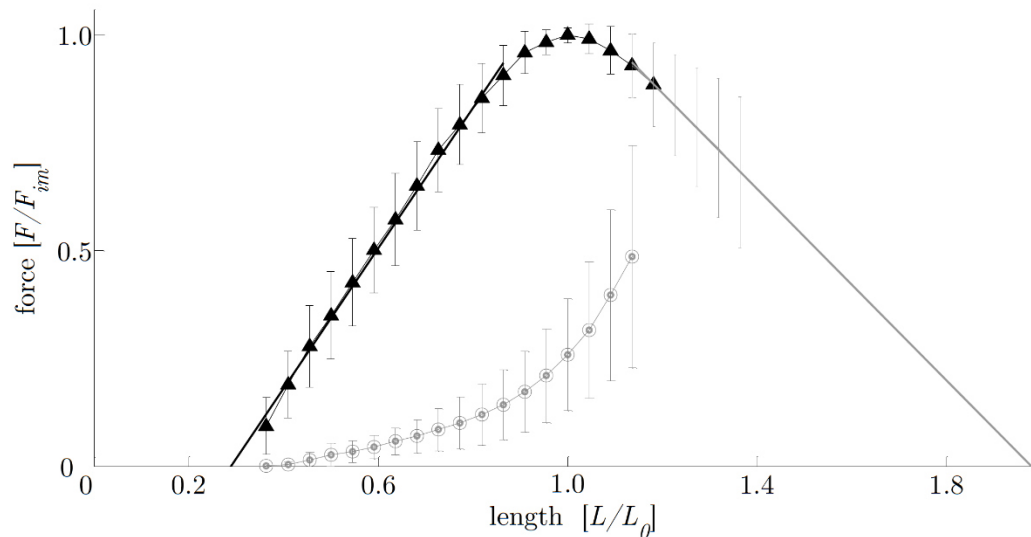


Figure 3. Representative force-length relationship of smooth muscle tissue. Depicted are the active (triangle) and passive (circles) isometric force-length relationships of longitudinal smooth muscle strips ($n=20$) from the fundus of porcine stomachs⁴⁴. The force- and length values are normalized to maximum isometric force (F_{im}) and optimum muscle length (L_o), respectively. Error bars indicate the standard deviation and the solid, straight lines illustrate the fitted linear ascending- and descending limbs. Figure adapted and edited from Tomalka et al. (2017)⁴⁴, permission to reproduce under the terms of the CC-BY license.

Smooth muscles display a wider FLR than striated muscles, which is especially important as many organs undergo huge deformations. Furthermore, they display plastic adaptations after resting on a muscle length for some time, attributed to rearrangements of the contractile units^{45,46} and an increased recruitment of myosin monomers⁴⁷. Thereby, for a short term, the active FLR is shifted^{42,48} and the smooth muscles retain the ability to contract forcefully at larger or shorter lengths.

Force-velocity relationship

Characteristically for all muscle types, the contraction velocity decreases with an increase of external load, as derived from Hill's studies on isolated, skeletal frog muscle⁴⁹. The course of the force-velocity relationship (FVR) is characterized by a hyperbolic shape described by the hill-shape model (**Figure 4**). Against a load of zero, the muscle exhibits its maximum shortening velocity (v_{max}). With increasing load, the shortening velocity progressively decreases until the muscle cannot overcome the external load and the shortening velocity is zero (isometric contraction). The curvature factor (*curv*) is a parameter that describes the shape of the FVR. A concentric contraction is described by the hyperbolic Hill equation⁴⁹

$$(F + a)(V + b) = c,$$

where F and V are the force and velocity, respectively, and a , b and c are constants. The curvature factor follows $curv = a/F_{im}$. A higher *curv* indicates a straighter course of the FVR.

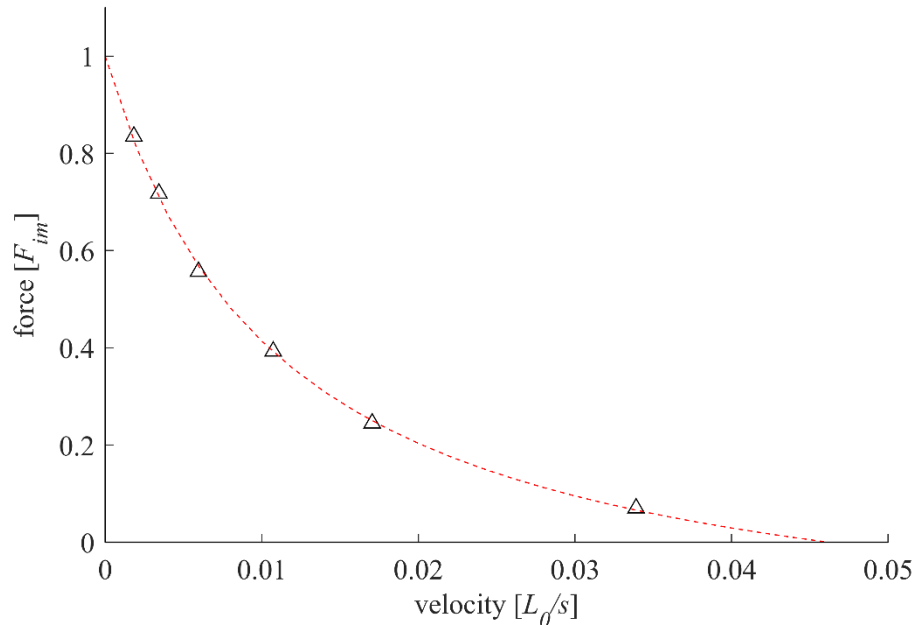


Figure 4. Representative force-velocity relationship of smooth muscle tissue – illustrated by a circumferential smooth muscle layer strip from the porcine fundus ($n=1$). The force- and length values are normalized to maximum isometric force (F_{im}) and optimum muscle length (L_0), respectively. Triangles indicate experimentally determined data points. The red dotted line illustrates the hyperbolic Hill-fit. With decreasing force against the muscle shortens, it's velocity increases in a hyperbolic way.

The FVR also has an eccentric portion, describing the muscle's force generation during lengthening⁵⁰. However, eccentric contractions are not thematized in this thesis, as they are not as physiologically relevant in smooth muscle as concentric contractions or as they are in striated muscle.

1.1.2 The stomach

The stomach is a j-shaped, hollow organ of the gastrointestinal tract. It lies in the upper left abdomen, connecting the esophagus cranially to the duodenum caudally. Its main functions are the storage, digestion, and propulsion of ingested food. As depicted in **Figure 5**, the stomach can be divided into three anatomical regions (from cranial to caudal)²⁵: The fundus (upper part, superior to the junction between stomach and esophagus), the corpus (big central region), and the antrum (bottom part). The lesser curvature and the greater curvature run along the medial, inner side and

the lateral outer side of the stomach, respectively. At the exit to the duodenum, the pyloric sphincter is located.

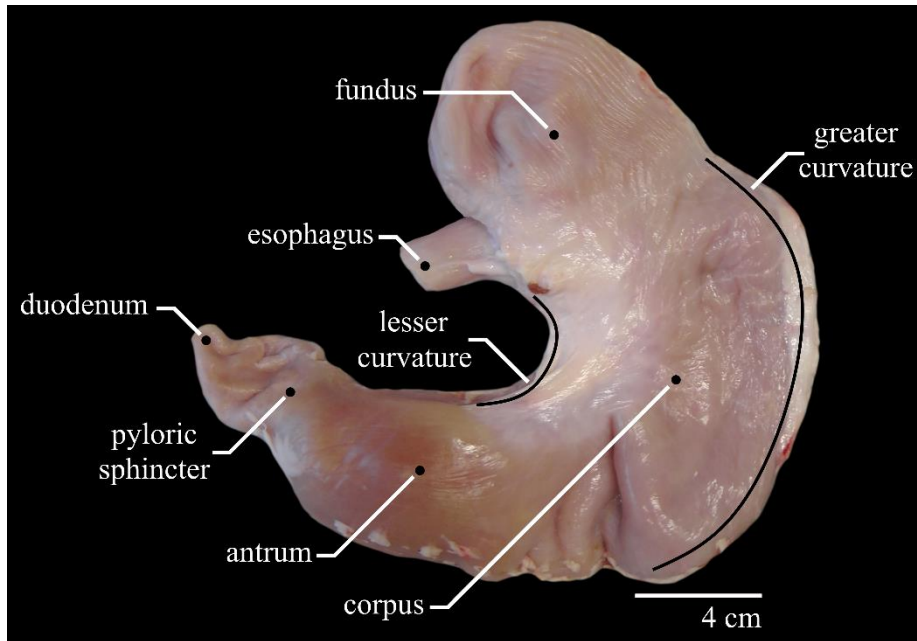


Figure 5. Ventral view of the porcine stomach. Depicted are the anatomical regions and distinctive structural features.

The wall consists of 4 layers (from the inside out) (**Figure 1a**): tunica mucosa, tunica submucosa, tunica muscularis, and tunica serosa. The mucosal component of the stomach secretes acids and enzymes⁵¹, necessary to chemically digest the food while also protecting the inner layers from the gastric juice. In the empty stomach, the mucosa exhibits folds called rugae, which increase the mucosal surface area and thereby enable greater expansions of the stomach. The tunica muscularis consists of multiple sublayers of single-unit smooth muscle fibers, which facilitate gastric motility through their ability to relax and contract. The gross structure of the stomach wall is consistent throughout all regions; however, the tunica muscularis in particular features certain variations¹⁶. In the fundus, it consists of two distinct, orthogonally aligned sublayers, with the outer sublayer oriented in the longitudinal (along the greater curvature) direction and the inner sublayer oriented in the circumferential (perpendicular to the greater curvature) direction. Further caudal, the tunica muscularis increases in thickness, being the thickest in the antrum with a predominant amount of smooth muscle fibers oriented in the circumferential direction.

This particular course can be derived from the separate functions between the cranial and caudal stomach. The fundus and the upper part of the corpus mainly serve as a reservoir for gastric content, while the lower part of the corpus and the antrum act as food grinder and propeller ⁵². Upon food ingestion, the tunica muscularis in the proximal stomach relaxes, by which the fundus is able to expand and accommodate food ^{53,54}. After storing the food for some time, it is transported further caudal through a gradual increase in muscle tone. In the antrum, the thick muscular layer pushes the gastric content through phasic peristaltic contractions towards the pyloric sphincter, which in turn closes and forces it backward, thereby grinding and mixing it with gastric juice ²⁸. Through this cyclic propelling and retropelling, the particles are eventually small and liquified enough that they pass through the pyloric sphincter and exit the stomach.

The stomach is innervated by the autonomic nervous system, whereas parasympathetic stimulation (e.g., via acetylcholine) increases muscle activity and sympathetic stimulation (e.g., via noradrenaline) inhibits the muscle. Furthermore, the stomach smooth muscle is regulated by the enteric nervous system through ICC's situated within and between the muscle layers as part of the myenteric plexus ⁵⁵. The ICC's produce slow waves in the membrane potential of stomach smooth muscle cells, which cause spontaneous peristaltic contractions in the antrum and lower corpus as soon as the membrane threshold is reached.

1.1.3 The urinary bladder

The urinary bladder is a hollow, distensible organ located at the base of the pelvic floor superior to the reproductive organs and ventral to the rectum. Along with the urethra as its outlet, the bladder is the main component of the lower urinary tract. It receives urine from the kidney via the ureters, temporarily stores it, and periodically expels it out of the body via the urethra. As depicted in **Figure 6**, the bladder consists of three anatomical regions (from cranial to caudal): the apex (dome), the body (central region), and the trigone (base).

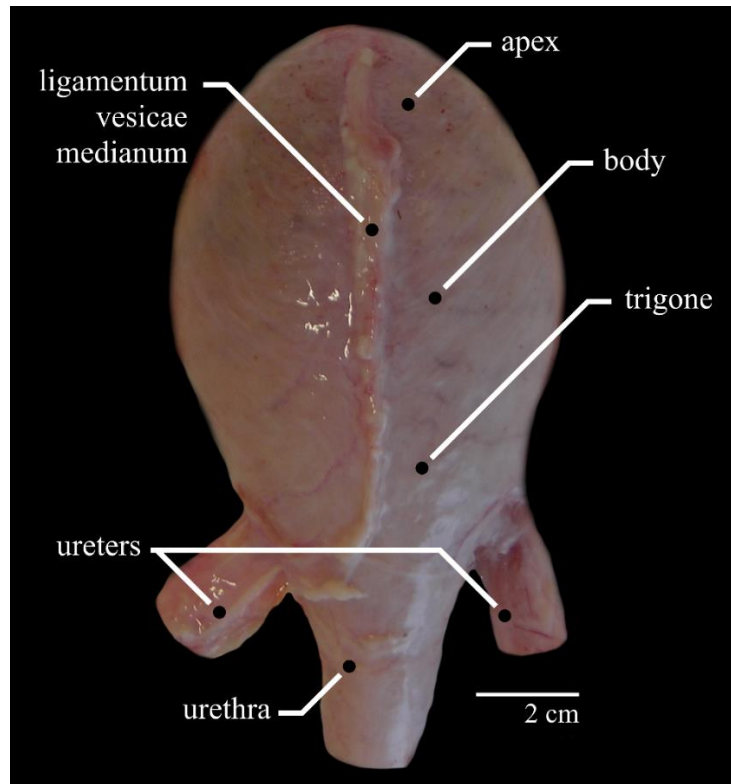


Figure 6. Ventral view of the porcine bladder. Depicted are the anatomical regions and distinctive structural features. Note: The ligamenta vesicae lateralia are not visible, as these are attached dorsally.

The bladder is fixated to the pelvis dorsolaterally via the ligamenta vesicae lateralia and ventrally via the ligamentum vesicae medianum. Laterally and medially at the trigone, the two ureters and the urethra connect to the bladder, respectively. The bladder wall consists of several layers (from the inside out) (**Figure 1b**): tunica mucosa, tunica submucosa, tunica muscularis (*M. detrusor vesicae*), and tunica serosa. While the mucosal component protects the detrusor from the urine and modulates afferent nerve- and detrusor activity in response to mechanical or chemical stress⁵⁶, the detrusor is responsible for the bladder's motility. It contains bundles or sub-layers of smooth muscle fibers which deviate in orientation, depending on the bladder's region and depth within the wall¹². The single-unit type smooth muscle fibers in the detrusor are interconnected via gap-junctions⁵⁷ to be able to contract synchronously upon activation.

Inhibited by sympathetic nerves, the detrusor muscle relaxes, by which the bladder is able to receive and store urine. At the same time, the urethral sphincter, which consists of smooth (internal urethral sphincter) and striated (external urethral sphincter) muscle tissue⁵⁸, remains in a

contracted state, keeping the urethral orifice closed. During the storage phase, the bladder maintains a constantly low inner pressure until a capacity threshold is reached ⁵⁹. Thereupon, tension-sensitive afferent nerves transmit impulses ⁶⁰, prompting the conscious urge to urinate, which can be postponed voluntarily through control of the external urethral muscle and certain pelvic muscles ⁶¹. Urination is eventually initiated by the parasympathetic micturition reflex ⁶¹, whereupon the detrusor generates high inner pressure through a coordinated, fast contraction. Accompanied by a simultaneous relaxation of the urethral sphincter, the bladder quickly reduces in volume and propels the urine out of the body. Subsequently, the urethral sphincter contracts again, and another cycle of filling and emptying starts over.

1.2 Methodological background

1.2.1 Experiments on biomechanical properties

A common method to investigate smooth muscle biomechanics are *in vivo* experiments, e.g., barostat inflations of the stomach ^{62,63} or cystometric analyses of the bladder ^{64,65}, which describe the organs' flow rate or volume-pressure behavior. Despite delivering practicable data that are particularly valuable for diagnosing medical conditions ^{62,66,67}, *in vivo* whole organ experiments are not suited to examine more specific characteristics, such as layer-, locational- or directional dependencies of smooth muscle properties. For such, *in vitro* tensile experiments are required, which present a typical method to adequately determine active biomechanical properties of not just smooth. ⁴⁴, but also skeletal- ⁶⁸ and cardiac muscle tissue ⁶⁹.

Using this method, smooth muscle tissue is typically removed from the organ of an anesthetized or freshly deceased organism and kept in a cooled, carbonated physiological nutrient solution to slow down the muscle tissue's degradation. Thereby, the muscle maintains the capacity to generate high forces for several hours after the organism's death and can still be activated externally through pharmacological- or electrical stimulation in the ensuing experiments. Muscle tissue strips are typically anchored on two ends via, e.g., clamps, hooks, or sutures, while one end is connected to a force transducer. The muscle tissue is characteristically fixated so that the muscle fiber orientation coincides with the force measuring axis, allowing for a precise detection and

quantification of muscle properties. **Figure 7** illustrates part of the experimental set-up used in this thesis as an example for a uniaxial testing apparatus by which biomechanical muscle properties, including the FLR and FVR, can be accurately determined.

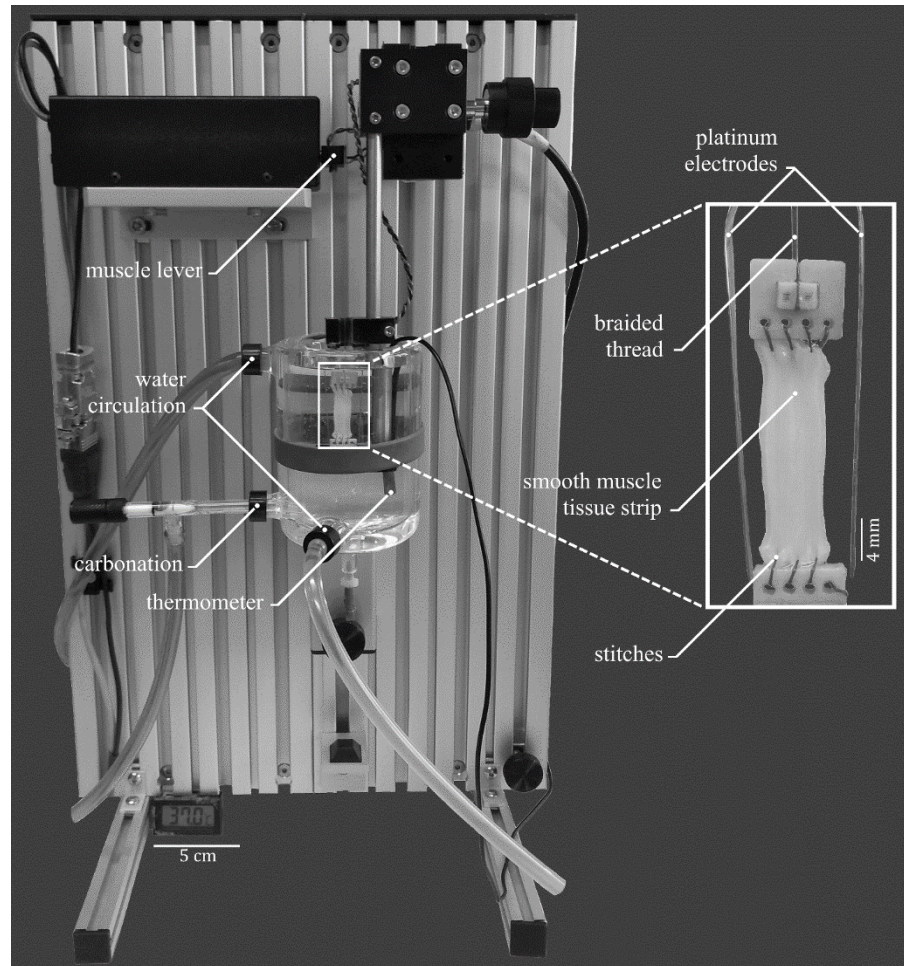


Figure 7. Exemplary depiction of an experimental set-up for the determination of biomechanical muscle properties. Shown is a part of the Aurora Scientific 1205A *in vitro* test apparatus (Aurora Scientific Inc., Aurora, ON, Canada). A smooth muscle strip is fixated vertically in a chamber filled with Krebs solution. The strip is threaded to rectangular blocks, of which the upper one is connected via a braided fishing line to the muscle lever, and the bottom one is clamped to a height adjustable stage. The muscle strip's force and -length are controlled and recorded by the muscle lever. Muscle contractions are initiated through transversal electric stimulations by platinum electrodes located laterally along the strip. Water, whose temperature is regulated externally by a circulation thermostat, is continuously flowing through the chamber wall to keep the temperature of the Krebs solution at a constant temperature. Moreover, in the solution is a thermostat to monitor the temperature and an injection that carbonates the solution throughout.

1.2.2 Analysis of microstructural properties

In organ walls, microstructural characteristics such as the amount of smooth muscle tissue or collagen, as well as the orientation of their fibers are of high interest, as thereby the results from biomechanical experiments can be connected to the underlying structure for a more comprehensive interpretation^{12,16,70}. Microstructural analyses are typically realized from digital pictures of histological sections of tissue samples. To obtain these, samples dissected from a certain location of the organ are either rapidly frozen or dehydrated and embedded in wax and subsequently sliced by a microtome. Using various coloring protocols, the sections can be stained to depict certain features, depending on the objective of the investigation. Analyses of smooth muscle proportion and -orientation have been realized, e.g., using Van Gieson's stain⁷⁰ or the picrosirius red staining^{12,16,44}, which tint muscle tissue and collagen in contrasting colors. **Figure 8** shows an example of histological cuts by which the orientation of the fiber bundles in bladder tissue has been investigated depending on their depth within the organ wall¹².

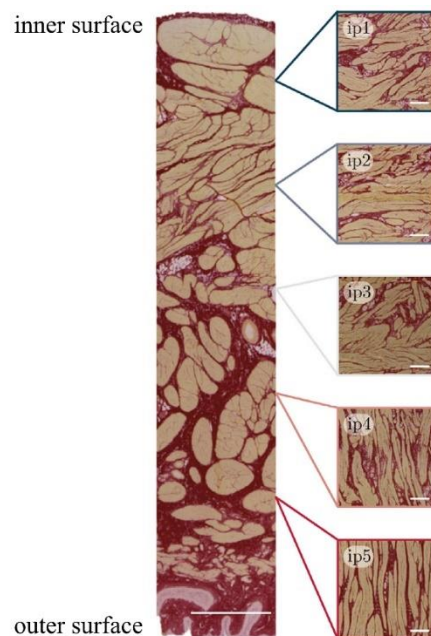


Figure 8. Exemplary illustration of a histological analysis of organ wall tissue as conducted by Morales et al. (2018)¹². Muscle tissue and collagen are stained yellow and red, respectively. Depicted is a cross-sectional slice from the porcine bladder wall. In-plane slices, ip1 to ip5, show the different orientations of smooth muscle fiber bundles from the innermost to the outermost location of the wall. The dominant fiber bundle orientation has been calculated from the structure tensor according to Rezakhaniha et al. (2012)⁷¹. The white bars are scaled to 1mm in length. Figure adapted and edited from Morales et al. (2018)¹², reproduced with permission from Elsevier.

1.3 Research questions and aims of the studies

Each of this thesis' studies focused on different research questions about stomach or bladder smooth muscle tissue. When answered, the respective questions each represent a valuable gain in knowledge about these organs' motility and a great contribution to their realistic computational modeling.

1.3.1 Study I - Locational and directional smooth muscle properties of the urinary bladder

Biomechanical properties of the urinary bladder have been the subject of numerous studies^{12,24,64,70,72-90}, of which various examined active smooth muscle properties such as the FLR^{72,73,75,76,85,88-90} and the FVR^{73,76,86,87,89,90}. Thereby, experiments were predominantly conducted on smooth muscle strips from a predefined bladder location, oriented either in the longitudinal or circumferential direction. Nevertheless, an organ may show locational and directional differences in biomechanical properties. For example, the vagina has been shown to exhibit regional differences in active⁹¹ and passive⁹² mechanical characteristics, or the stomach has been found to display locational and directional variations in its passive biomechanics^{16,93-96}. Due to the bladder's complex function, its composition of distinct regions, and its dissimilar attachment via the ligaments between the ventral and dorsal sides, it is crucial to investigate the bladder for locational and directional dependencies of biomechanical characteristics.

It has already been shown that the bladder features anisotropy and heterogeneity in its microstructure^{12,70,77,97}, particularly in the smooth muscle fiber orientation, as well as in its passive biomechanical characteristics^{12,70,75,77,79,80,98}. Nevertheless, the results on the latter are ambivalent. In contrast, studies on locational or directional dependencies of active muscle properties are scarce. One study investigated the FLR of tissue strips from one specific location directed in the longitudinal and in the circumferential direction⁷⁵, whereas another study compared the FLR and contractile responsiveness of longitudinal strips from the ventral and dorsal side⁹⁹. However, the FVR has not yet been compared between regions or directions, and no study has yet been conducted to systematically investigate muscle properties from multiple regions and multiple

directions. Due to the ambivalent results on passive bladder biomechanics and the limited knowledge about heterogeneity and anisotropy of active bladder biomechanics, further and more detailed examinations are required to adequately describe how the healthy bladder operates on a whole organ level. Therefore, this study focused on the following questions:

Does the urinary bladder display locational or directional dependencies of

- **active biomechanical properties?**
- **passive biomechanical properties?**
- **microstructural properties?**

The aim was to give new and broadening insights into bladder motility, to deliver novel and extensive datasets on the active behavior of the whole bladder, and to extend the existing knowledge about its passive mechanical behavior. The yielded data are intended to be integrated into three-dimensional, computational bladder models, by which the healthy active and passive bladder behavior can be simulated more holistically and realistically.

1.3.2 Study II - On a coupled electro-chemomechanical model of gastric smooth muscle contraction

Lately, computational, three-dimensional organ models, as for example for the uterus¹⁰⁰ or the bladder⁷⁵, have been developed, which are able to realistically depict certain mechanisms of the healthy organ. By manipulating the model's input parameters, simulations of diseased or dysfunctional tissue can be realized, which may help in the prediction, prevention, and treatment of various diseases. There exist several studies that proposed whole organ models of the stomach, simulating the electrophysiology¹⁰¹⁻¹¹¹ or the flow dynamics¹¹²⁻¹¹⁵, and to a lesser extent the electro-chemomechanical contraction process^{116,117}. However, the referenced models on the latter mechanism used various parameters and constants that were not identified experimentally. Hence, it is of importance to develop a whole organ model that simulates the electro-chemomechanical contraction process, incorporating experimentally acquired data. While active biomechanical properties of stomach smooth muscle have been determined in great detail⁴⁴, they have not yet been investigated for directional dependencies. Furthermore, passive biomechanical

characteristics have been examined several times ⁹³⁻⁹⁶, whereas investigations on the contribution of the different layers to the load-bearing process yielded ambivalent results ^{16,94,95}, which might be based on differences in the methodology. Thereby, conducting uniaxial tensile tests, the following questions were addressed:

- **What are the active biomechanical properties of stomach smooth muscle?**
- **What are the passive biomechanical properties of stomach wall tissue?**
- **Are there differences in biomechanical properties between the longitudinal and circumferential muscle tissue?**
- **What is the contribution of the mucosal layer to the overall load-bearing process in the stomach wall?**

The aim was to propose a three-dimensional model of the stomach, depicting the load transferring system and the excitation-contraction coupling process on a whole organ level, which integrates experimental data on the stomach's active and passive biomechanics.

1.3.3 Study III - Influence of layer separation on the determination of stomach smooth muscle properties

Uniaxial tensile experiments are a standard method to determine muscle properties of skeletal ⁶⁸, cardiac ⁶⁹, and smooth muscle ⁴⁴ (see **Chapter 1.2.1**). However, in contrast to striated muscle tissue, smooth muscles characteristically contain differently oriented muscle sublayers or fiber bundles ^{12,16}. Thereby, when testing on tissue strips that feature the whole muscle layer, the strip contracts not only in the direction of the measuring axis, but also in the transverse direction. Through force transmission between the muscle fiber bundles or muscle sublayers, similarly to myofascial force transmission in skeletal muscle ^{118,119}, a transversal shortening might affect the biomechanical properties of the tissue strips measured in the lengthwise direction.

Hence, the following novel questions come up:

- **Does the separation of the muscular sublayers influence the biomechanical properties of stomach smooth muscle tissue strips, compared to whole-muscle strips?**
- **What parameters of the FLR and FVR are affected?**
- **Does the magnitude of this effect depend on the contraction type?**

The intent of this study is to identify, characterize, and explain such an effect, which would impact the evaluation of past results from uniaxial experiments regarding the integration into organ and muscle models, as well as regarding the comparison between different studies in the literature. Furthermore, the gained knowledge of this study can help future studies in the choice of the methodological design, depending on their specific aim, whether they focus on the determination of either pure muscle properties or organ wall properties.

2 Locational and directional dependencies of smooth muscle properties in pig urinary bladder

2.1 Introduction

The urinary bladder is a hollow organ, which absorbs, stores and releases urine, and is thereby exposed to enormous deformation. The bladder (**Figure 9a**) is located at the base of the pelvic floor superior to the reproductive organs and ventral to the rectum. The bladder can be divided into three anatomical regions (from cranial to caudal): the apex (dome), the body (central region) and the trigone (base) (**Figure 9b**). The bladder wall consists of several layers (from the inside out): tunica mucosa, tunica submucosa, tunica muscularis (*M. detrusor vesicae*), and tunica serosa. The detrusor consists of sub-layers of smooth muscle cells, which are predominately arranged in longitudinal and circumferential orientation¹². The detrusor muscle is of special physiological and medical interest, as it provides contraction during micturition. It generates high inner pressure by a coordinated, fast reduction of bladder volume in order to successfully propel urine out of the body. The required muscle forces mainly depend on biomechanical properties such as the force-length- (FLR) and the force-velocity-relationship (FVR). Characterization of these biomechanical properties is essential to better understand bladder functioning. Age^{81,82}, disease⁶⁴ or injuries^{83,84} can alter the biomechanical properties of the bladder wall, resulting in certain bladder dysfunctions. The associated lower urinary tract symptoms represent a global health problem²⁰, whereby common methods of treatment such as bladder augmentation surgery or transurethral resection of the prostate have short- and long-term complications^{120–123}. The specific understanding of healthy urinary bladder functioning is a basic prerequisite to identify the causes of disease and to advance medical treatment. Realistic three-dimensional models can describe the function of whole organs in health and disease^{106,124}. Nonetheless, the development of a computational model requires the determination of characteristic passive and active biomechanical and physiological properties (FLR and FVR). For such investigations, whole bladder experiments are insufficient and *in vitro* tests on isolated tissue strips are required. These, in turn, are hardly possible to conduct on intact human bladder tissue. Alternatively, the examination of pig bladder strips is of special importance due to the structural and mechanical similarities to the human bladder^{23,24}.

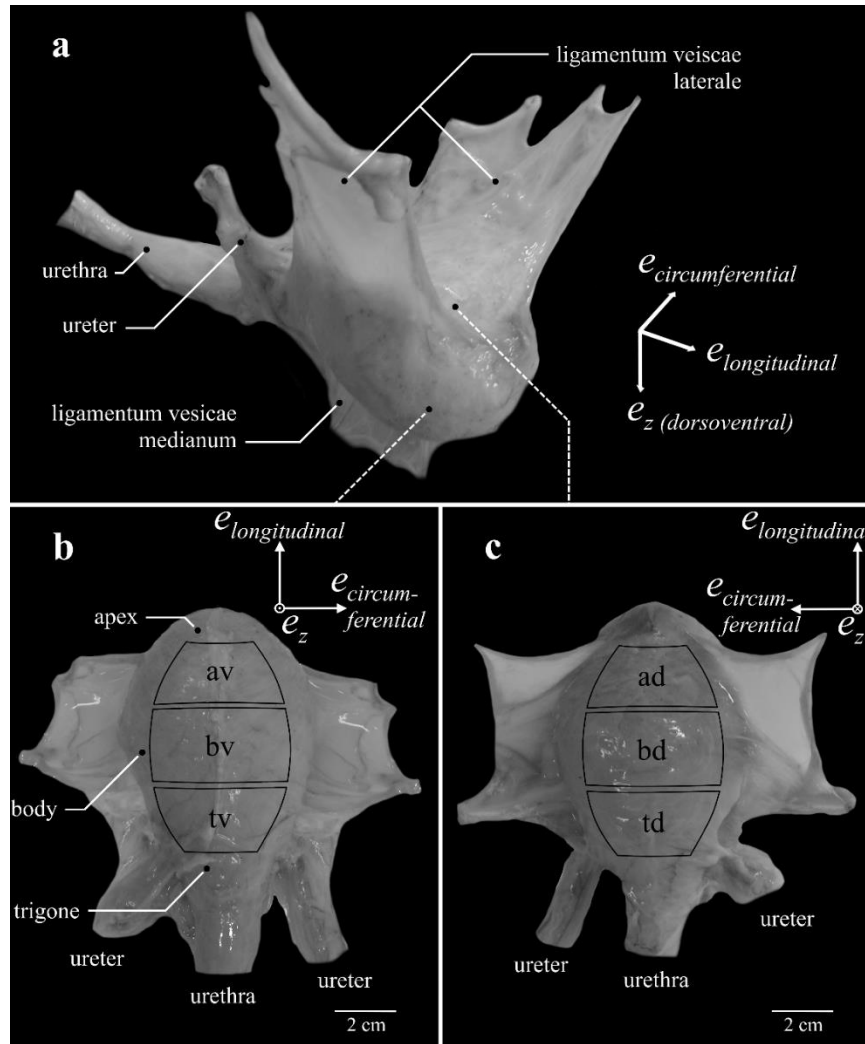


Figure 9. Porcine urinary bladder anatomy and definition of locations. A bladder filled with 300 ml Krebs solution is depicted (a) as it is suspended in the female pig. Note, only one ureter can be seen. (b) Ventral (av -apex ventral, bv - body ventral, tv - trigone ventral) and (c) dorsal (ad -apex dorsal, bd - body dorsal, td - trigone dorsal) views of the bladder with extended *ligamenta vesicae lateralia*. Curved black rectangles indicate the six locations from which tissue samples were dissected. Permission to reproduce figure under the terms of the CC-BY license.

Most studies on active and passive bladder properties determination have used single tissue strips removed from only one specific bladder region with a specific strip direction (longitudinal or circumferential)^{72–76,85–90}. Therefore, it is an important question whether there exist differences in tissue strip properties depending on location (heterogeneity) and/or depending on tissue strip direction (anisotropy).

Porcine urinary bladders were found to display anisotropic^{12,70,75,78–80} and heterogeneous^{12,70} passive behavior. The trigone showed higher passive stress than the body and the apex^{12,70}. Results on whether longitudinal or circumferential tissue direction exhibit higher passive stiffness were ambivalent^{12,70,75,78–80}. Histological investigations demonstrated regional microstructural differences concerning bladder wall composition^{12,70} and smooth muscle fiber orientation¹². It has been reported that the portion of the detrusor was decreased in the trigone and that smooth muscle fiber orientation was anisotropic on the ventral side of the bladder¹². Consequently, it might be assumed that the active properties vary accordingly. An elaborate investigation of contractile properties accompanied by histological analyses might reveal locational or directional dependencies and enable us to draw conclusions about the underlying force-generating mechanisms. In contrast to the series of studies examining location and direction dependent passive bladder properties, there exists only a limited number of studies examining active muscle properties. Seydewitz et al.⁷⁵ reported differences in maximum stress between longitudinally and circumferentially directed tissue strips taken from one bladder location (dorsal apex) only. Comparing tissue strips isolated from the ventral and dorsal side of the bladder, Longhurst et al.⁹⁹ found small differences in the contractile responsiveness of the strips but no differences between their force-length relations. Therefore, a systematic investigation of location and direction dependent active muscle properties is required for the development of more integrative and realistic urinary bladder models.

Therefore, the present study is the first to perform *in vitro* experiments on porcine bladder tissue strips, determining active biomechanical properties (such as FLR and FVR) of six distinct urinary bladder locations through uniaxial tests in both longitudinal and circumferential directions. Furthermore, passive characteristics were investigated in specific ramp-length experiments. Additionally, histological analyses were carried out to characterize the smooth muscle content, considering both locational and directional effects. To facilitate comparisons with a recent study on microstructural and passive mechanical differences of pig urinary bladder¹², we similarly distinguished between apex, body, and trigone, and the ventral (**Figure 9b**) and dorsal bladder (**Figure 9c**).

2.2 Materials and methods

2.2.1 Experimental set-up

The study was exempted from ethical committee review according to national regulations (German Animal Welfare Act), as urinary bladders of healthy, female domestic pigs (*Sus scrofa domestica*, age: ≈ 6 months, mass: ≈ 100 kg) were obtained from a slaughterhouse immediately after animal sacrifice. The experiments were conducted on 43 urinary bladders within 10 h after death. The experimental set-up, preparation, and handling of bladder smooth muscle tissue have previously been described in detail^{44,76}. An aerated (95% O² and 5% CO²) Krebs solution (25 mM NaHCO³; 1.2 mM NaH²PO⁴; 2.4 mM MgSO⁴; 5.9 mM KCL; 2.5 mM CaCl²; 117 mM NaCl and 11 mM C⁶H¹²O⁶; pH 7.4)¹²⁵ was used for storage of the tissue and realization of the experiments at temperatures of 4°C and 37°C, respectively. Similar to a recent study¹², the bladder was categorized into three regions (apex, body, and trigone) and two sides (ventral and dorsal), resulting in six locations (**Figure 9b** and **c**, apex dorsal [ad], apex ventral [av], body dorsal [bd], body ventral [bv], trigone dorsal [td], trigone ventral [tv]). The entire bladders were dissected along the ligamentum vesicae medianum. Subsequently, tissue strips (0.93 ± 0.24 g) of 16×8 mm were cut out of the designated locations (**Figure 9b** and **c**) either in the longitudinal (along the apex to trigone line) or circumferential direction. The strips were mounted vertically to a motor/force transducer (Aurora Scientific 305C-LR dual mode muscle lever system). The strip was suspended in a relaxed state at a very short length (clearly sagging). Then the strip was passively lengthened through an isokinetic ramp (5 mm/min) until a passive force of 5–10 mN was reached. After finishing the ramp, the strip was kept at this length, while the passive force development settles at a negligible baseline value (< 1 mN). The length of the strip, averaging 12.41 ± 2.08 mm, between clamp and attachment hooks was determined with a digital sliding caliper and was defined as slack length (L_s). Muscle contractions were induced by electrical stimulations (900 mA, 100 Hz, 5 ms)¹²⁵ for about 12 s. The muscle properties were determined after an equilibration period of 30 min and as soon as a stable force generation (deviation $< 5\%$ of active isometric force) was attained.

2.2.2 Determination of muscle properties

Uniaxial experiments were performed *in vitro* on 94 tissue strips ($n = 94$). **Table 1** summarizes the number of samples examined for each analyzed parameter. The protocols used to determine the FLR and FVR have been described earlier^{44,76}. Briefly, the FLR was investigated by a series of isometric contractions with increasing muscle length (L) until passive forces reached 50% of the maximum isometric force (F_{im}). The muscle length at F_{im} was defined as the optimal muscle length (L_0). The ascending- and descending limbs of the FLR were fitted using linear regression models ($f(x) = mx + b$, with $x = L/L_S$) to extrapolate to lengths of zero force generation. The respective distances to L_0 were defined as the width of the ascending- (w_{asc}) and descending limb (w_{desc}). The FVR was determined by isotonic contractions at L_0 against forces of 0.1–0.9 F_{im} . The data were fitted with Hill's hyperbolic equation⁴⁹ to yield the maximum shortening velocity (v_{max}) and the curvature factor $curv = a/F_{im}$ (damping increases with decreasing $curv$; a describes the force asymptote)¹²⁶. Between all contractions, recovery phases of 5 min were interposed and the “cycling-protocol” by Brenner¹²⁷ was applied.

The CSA was calculated by the product of the thickness and the width of the tissue strip at L_0 , assuming a rectangular cross-section. The active and passive isometric forces at L_0 were divided by the strip's CSA to calculate the maximum active stress (p_{act}) and the corresponding passive stress (p_{pass}), respectively.

Table 1. The number of investigated tissue samples of each group for the observed muscle properties and parameters. Permission to reproduce table under the terms of the CC-BY license.

			FLR					FVR	
			L_0	w_{asc}	w_{desc}	p_{act}	p_{pass}	v_{max}	$curv$
Number of samples	longitudinal	Trigone	ventral		6			7	
			dorsal		6			7	
		Body	ventral		6			6	
			dorsal		6			6	
		Apex	ventral		7			8	
			dorsal		6			11	
	circumferen- tial	Trigone	ventral		6			6	
			dorsal		6			6	
		Body	ventral		6			6	
			dorsal		6			6	
		Apex	ventral		6			6	
			dorsal		6			6	

2.2.3 Histological observation

Histological examinations were performed in accordance with previous studies^{44,76}. In total, $n = 36$ longitudinal and circumferential tissue strips from the designated locations (**Figure 9b** and

c) were cut out of one representative urinary bladder. Subsequently, the strips were stretched to 300% L_S (to be the strip length where F_{im} is generated) in the corresponding direction and fast frozen in an isopentane bath cooled with liquid nitrogen. A cryomicrotome was used to cut cross-sectional and lengthwise-sectional slices from the frozen samples, which were stained with Picrosirius Red staining protocol¹² and photographed using a digital microscope (Zeiss Smartzoom 5). The smooth muscle content was determined through a color threshold using an image editing software (ImageJ 1.49 v, National Institutes of Health, USA). Stretched muscle fibers in strip direction (which were expected to generate force) were clearly recognizable from lengthwise sections.

The thickness of stretched sublayers was measured from lengthwise sections (**Figure 13a**) and used to determine the amount of lengthwise-oriented muscle bundles in cross-sectional slices (**Figure 13b**). The area of stretched muscle fibers normalized to the CSA was defined as the force-generating smooth muscle content ($SMC_{stretched}$).

2.2.4 Statistics

For further statistical analyses, data of muscle properties were normalized as follows: (1) Force- and length values were divided by individual F_{im} and L_0 , respectively. (2) Velocity data were normalized to optimum muscle length and expressed in L_0/s . For comparison of pooled bladder locations, the strips were assigned according to their particular region to apex, body, or trigone (ABT) and to their position on the ventral or dorsal side of the bladder (VD) (**Figure 9b** and **c**). Additionally, the strips were differentiated according to their direction (longitudinal or circumferential). This results in 12 groups (3 ABT \times 2 VD \times 2 directions). The biomechanical properties were analyzed using seven parameters (L_0 , w_{asc} , w_{desc} , p_{act} , p_{pass} , v_{max} , and $curv$). Each parameter was investigated using a 3-way ANOVA (DIRECTION [longitudinal vs. circumferential] \times VD [ventral vs. dorsal] \times ABT [apex vs. body vs. trigone]). Additionally, $SMC_{stretched}$, which was observed through 36 strips from one bladder, was tested for significant locational and directional differences using an ANOVA with repeated measures and a paired t-test, respectively. The effect sizes were calculated using partial eta squared (η_p^2) and classified as

low ($\eta_p^2 = 0.01$), medium ($\eta_p^2 = 0.06$), and high ($\eta_p^2 = 0.14$)¹²⁸. Significant main effects or interactions were followed up by a Bonferroni *post-hoc* test. A significance level of $P < 0.05$ was used for all analyses. Statistical analyses were carried out using SPSS 23 (IBM Corp, Armonk, NY, USA).

2.3 Results

Typical FLR and FVR were shown (longitudinal strips from body dorsal) in **Figure 10**. The shape of the active isometric force-length relationship is similar for all groups investigated. Specifically, the FLR exhibits a linear ascending limb, a narrow bell-shaped plateau region, and a linear descending limb (**Figure 10a**). Thus, the FLR resembles an inverted parabola. The passive force-length dependency of the bladder tissue strip was characterized by an exponential increase of force with muscle length. The mean F_{im} of the bladder tissue strips was 1272.86 ± 201.47 mN ($n = 94$). Determining an average CSA of 36.65 ± 6.73 mm² of the whole bladder strips, this corresponds to p_{act} of 35.16 ± 6.82 kPa. Active force generation occurred at lengths between $0.43 \pm 0.41 L_S$ and $6.66 \pm 2.37 L_S$, corresponding to $0.138 \pm 0.135 L_0$ and $2.17 \pm 0.74 L_0$, respectively. F_{im} was reached at $3.07 \pm 0.28 L_S$, accompanied by passive forces of $27.15 \pm 9.14\%$ F_{im} , resulting in a mean p_{pass} of 9.26 ± 2.71 kPa. The tissue strips had an absolute length of 37.9 ± 4.83 mm at L_0 . The total FVR exhibited a typical hyperbolic shape (**Figure 10b**). The maximum shortening velocity was 2.68 ± 0.69 mm/s, corresponding to $0.071 \pm 0.017 L_0/s$. The mean *curv* was 0.371 ± 0.144 .

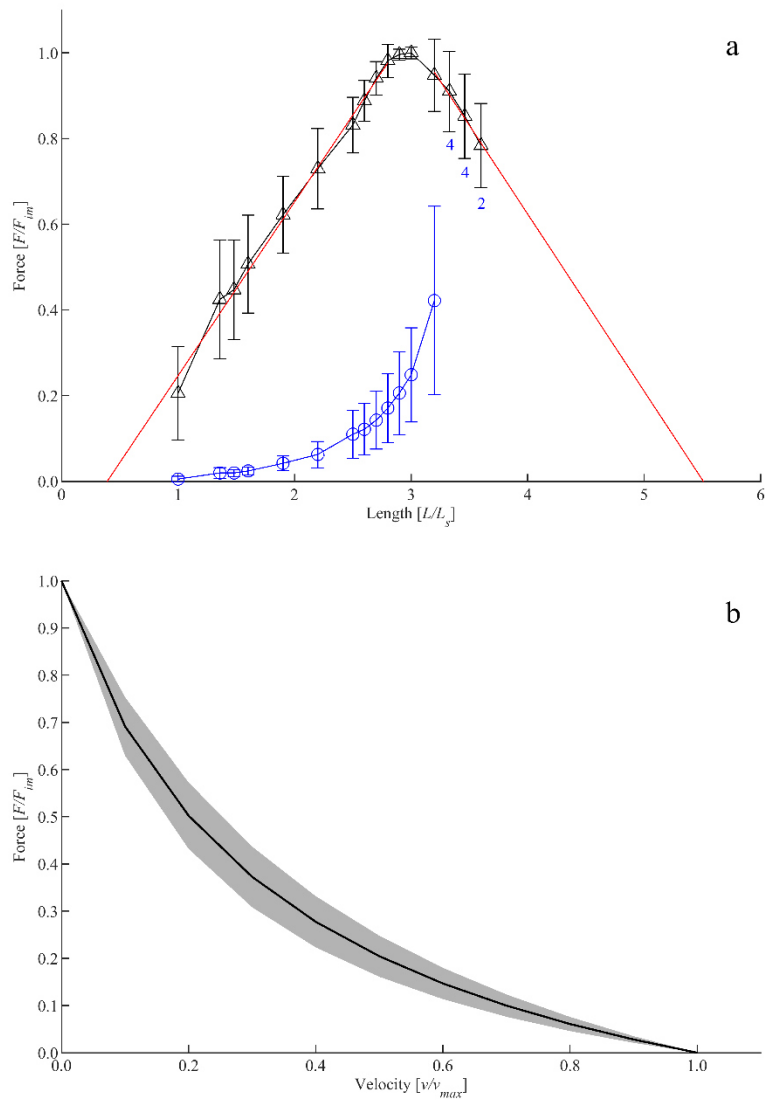


Figure 10. Muscle properties of longitudinal strips dissected from the dorsal body. (a) Force-length relationship. Length and force are normalized to slack length (L_S) and maximum isometric force (F_{im}), respectively. Triangles and circles depict mean values of active and passive isometric force, respectively. Whiskers indicate corresponding standard deviations. Red solid lines represent the ascending (f_1) and descending limb (f_2) of the force-length relationship, which were fitted by linear regression models following the equations: $f_1(x) = 0.4057x - 0.1594$ and $f_2(x) = -0.4138x + 2.279$, with $x = L/L_S$. Isometric force-length measurements comprise $n = 6$ tissue samples up to lengths of $3.2 L_S$; varying sample sizes were investigated at greater lengths (labeled with blue numbers below standard deviation bars on the descending limb). (b) Force-velocity relationship. Velocity and force values are normalized to v_{max} and F_{im} , respectively. Based on a series of isotonic contractions, force-velocity curves of $n = 6$ tissue samples were fitted using the typical Hill equation⁴⁹. The black curve and a grey area indicate mean values and standard deviations, respectively. Permission to reproduce figure under the terms of the CC-BY license.

The investigated biomechanical parameters for the 12 groups are presented in **Table 2**. No statistically significant differences were found between L_0 , w_{asc} , w_{desc} , v_{max} , and $curv$.

Table 2. Location dependency of optimal length (L_0), the width of ascending (w_{asc}) and descending limb (w_{desc}) of the force-length relationship, maximum shortening velocity (v_{max}), and curvature factor ($curv$) of the force-velocity relationship. Permission to reproduce table under the terms of the CC-BY license.

direction	location	L_0 [L/L_S]	w_{asc} [L/L_0]	w_{desc} [L/L_0]	v_{max} [L_0/s]	$curv$
longitudinal	tv	3.18 ± 0.36	0.95 ± 0.31	0.98 ± 0.52	0.073 ± 0.023	0.383 ± 0.149
	td	2.96 ± 0.33	0.81 ± 0.12	1.48 ± 1.21	0.066 ± 0.017	0.428 ± 0.155
	bv	3.08 ± 0.26	0.83 ± 0.09	0.90 ± 0.55	0.076 ± 0.019	0.328 ± 0.181
	bd	3.03 ± 0.20	0.89 ± 0.14	0.77 ± 0.16	0.072 ± 0.022	0.360 ± 0.120
	av	3.13 ± 0.37	0.93 ± 0.14	0.97 ± 0.28	0.062 ± 0.004	0.338 ± 0.090
	ad	3.08 ± 0.23	0.94 ± 0.15	1.56 ± 1.33	0.077 ± 0.027	0.341 ± 0.221
circumferential	tv	3.07 ± 0.29	0.83 ± 0.07	0.99 ± 0.19	0.061 ± 0.007	0.455 ± 0.131
	td	3.22 ± 0.19	0.79 ± 0.07	1.38 ± 1.18	0.069 ± 0.010	0.379 ± 0.102
	bv	3.09 ± 0.31	0.85 ± 0.08	1.03 ± 0.51	0.081 ± 0.019	0.405 ± 0.092
	bd	2.99 ± 0.25	0.82 ± 0.07	1.07 ± 0.38	0.077 ± 0.008	0.293 ± 0.135
	av	3.01 ± 0.24	0.84 ± 0.50	1.60 ± 0.77	0.068 ± 0.017	0.451 ± 0.156
	ad	2.98 ± 0.31	0.86 ± 0.13	1.32 ± 0.72	0.069 ± 0.008	0.314 ± 0.056
	Mean	3.07 ± 0.27	0.86 ± 0.14	1.17 ± 0.74	0.071 ± 0.017	0.371 ± 0.144

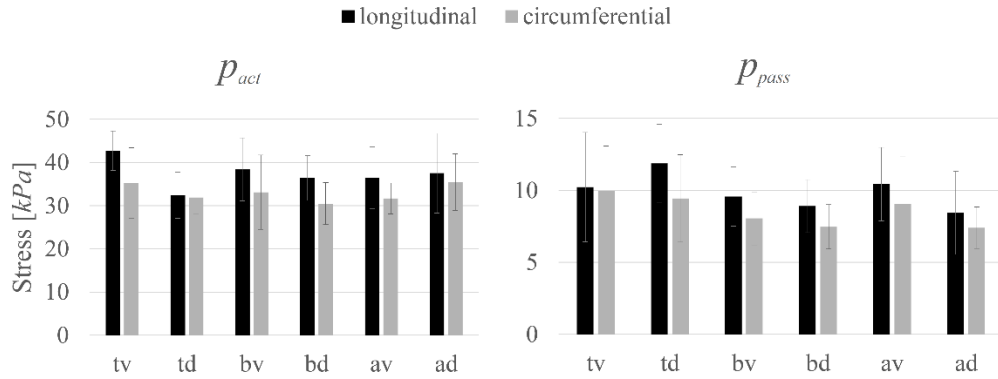


Figure 11. The dependency of maximum active isometric stress (p_{act}) and passive stress (p_{pass}) at optimal length (L_0) on location and direction. Mean values \pm standard deviations of longitudinal (black) and circumferential (grey) tissue samples are given. Permission to reproduce figure under the terms of the CC-BY license.

Location-specific differences in p_{act} and p_{pass} for longitudinally and circumferentially directed bladder strips are summarized in **Figure 11**. Tissue strips in the longitudinal direction exhibited a significantly higher p_{act} ($F_{1,61} = 8.206$, $P = 0.006$, $\eta_p^2 = 0.119$, **Figure 12a**) and p_{pass} ($F_{1,61} = 4.844$, $P = 0.032$, $\eta_p^2 = 0.074$, **Figure 12b**) than circumferentially directed strips. Furthermore, p_{pass} differed significantly between regions ($F_{2,61}=3.529$, $P=0.035$, $\eta_p^2 = 0.104$, **Figure 12c**). Strips from the trigone showed significantly higher p_{pass} than strips from the body ($P = 0.047$, **Figure 12c**).

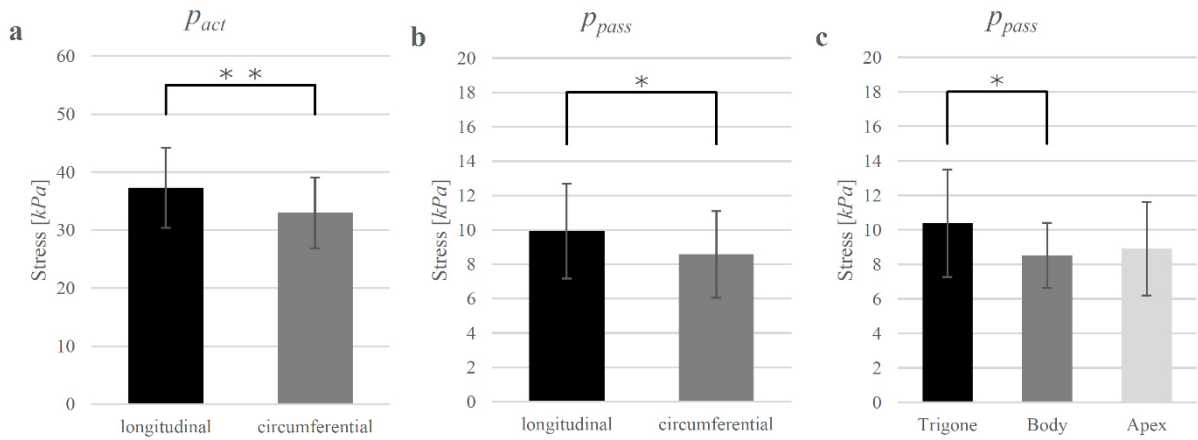


Figure 12. (a) Direction-dependency of maximum active isometric stress (p_{act}) and (b) passive stress (p_{pass}) at optimal length (L_0) and (c) region-dependency of p_{pass} . Mean values \pm standard deviations are given. Brackets and asterisks (*) mark significant differences in stress. Significance levels are marked as * for $P < 0.05$ and ** for $P < 0.01$. Permission to reproduce figure under the terms of the CC-BY license.

Examples of the lengthwise (**Figure 13a**) and cross-section (**Figure 13b**) of histologically stained bladder tissues (stretched to 300% L_s) are shown for one tissue strip (longitudinal direction from trigone dorsal). From inside to outside of the bladder wall, the tunica mucosa, submucosa, muscularis, and serosa are distinguishable. Longitudinal strips contained a significantly higher ($P=0.015$) amount of smooth muscle fibers in the strip direction ($SMC_{stretched} = 22.34 \pm 2.29\%$ CSA) than circumferential strips ($SMC_{stretched} = 20.63 \pm 1.97\%$ CSA) (see **Table 3**). There were no significant differences in $SMC_{stretched}$ between regions. Dividing the p_{act} of longitudinal (37.1 ± 6.91 kPa) and circumferential (33.0 ± 6.08 kPa) strips by their corresponding $SMC_{stretched}$ yielded no significant differences in active muscle stress (longitudinal 168.6 ± 30.0 kPa; circumferential: 162.2 ± 29.3 kPa; $P = 0.36$). Mean muscle stress of all strips was calculated to be 165.4 ± 29.6 kPa.

Table 3. Summary of quantitative histological data. The force-generating smooth muscle content ($SMC_{stretched}$) is the area of stretched muscle fibers normalized to the CSA. $SMC_{stretched}$ is illustrated exemplarily in Fig. 5b (green area). Permission to reproduce table under the terms of the CC-BY license.

strip direction	region	$SMC_{stretched}$ [%]	n
longitudinal	Trigone	23.1 ± 2.7	6
	Body	20.7 ± 1.8	6
	Apex	23.3 ± 1.6	6
circumferential	Trigone	20.5 ± 1.3	6
	Body	20.4 ± 2.6	6
	Apex	21.0 ± 2.1	6

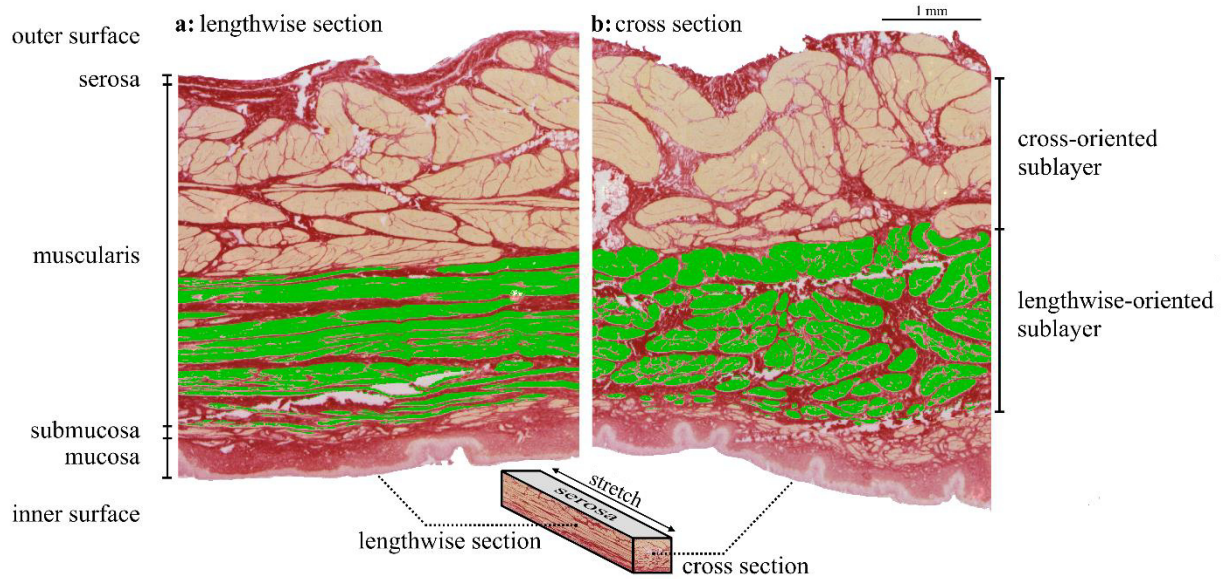


Figure 13. Lengthwise section (a: $e_{longitudinal} - e_z$ plane) and cross section (b: $e_{circumferential} - e_z$ plane) of a longitudinal strip (td) stretched to 300% L_S . In the lengthwise section (a) the lengthwise-oriented stretched muscle fibers are recognizable by their flat, thin shape and marked in green color. The thickness of the lengthwise-oriented sublayer was used to mark the corresponding sublayer in the cross-section (b). Thus, the area of the green colored fibers in the cross-section (b) corresponds to lengthwise-oriented muscle fibers, responsible for force generation in strip direction. $SMC_{stretched}$ is the ratio of the area of lengthwise-oriented muscle fibers and cross-sectional area of the whole strip. Note that the area of stretched muscle fibers (green) appears smaller than that of non-stretched fibers. This is due to a lengthwise stretch of the strip to 300% L_S . In this example (longitudinal strip, td), the lengthwise- and cross-orientated sublayers correspond to sublayers of longitudinal and circumferential smooth muscle fibers, respectively. Permission to reproduce figure under the terms of the CC-BY license.

2.4 Discussion

To our knowledge, this is the first systematic study investigating active and passive biomechanical as well as histological properties of pig urinary bladder tissue for locational and directional dependencies. Hence, active and passive uniaxial experiments have been performed *in vitro* on whole tissue strips to determine the FLR and FVR at six locations and in two directions.

Although passive characteristics of tissue strips were measured over a large length range (**Figure 10**), only one parameter, p_{pass} , was considered for the statistical examination of locational and directional differences in passive behavior. This parameter was determined at L_0 and, thus,

was related to F_{im} and maximal actin-myosin filament overlap. As L_0 did not differ between groups, p_{pass} is a valid parameter to compare passive stiffness between groups.

To study $SMC_{stretched}$, several tissue strips from each location and both directions were histologically examined at L_0 . It should be noted that this method categorized smooth muscle content in a dichotomous matter as smooth muscle cells were either aligned to the stretch or in opposition to it, resulting in non-specification of the angle of orientation. Although these strips were excised from only one bladder, the results are in agreement with former histological studies¹² and, thus, were suitable for calculation of pure muscle stress and interpretation of mechanical properties. Although biaxial tests can mimic *in vivo* bladder wall deformation in two dimensions, anisotropy can still be adequately detected through uniaxial experiments by measuring in two orthogonal directions.

The urothelium, an epithelial lining at the inner surface of the hollow organs of the urinary tract, consists of approximately 3-5 cell layers corresponding to about 3% of total bladder wall thickness in the rat¹²⁹. Thus, a negligible effect of the urothelium on passive whole bladder wall properties is expected. However, the urothelium has a modulating effect on smooth muscle contraction and relaxation¹³⁰. In the present study experiments were conducted on whole tissue strips without removal of the urothelium to ensure functional integrity. Several studies using electrical field stimulation of bladder tissue strips reported, that the urothelium inhibited the contractile response¹³¹⁻¹³³ whereas others found no influence on muscle contraction^{134,135}. Consequently, the influence of the urothelium on smooth muscle tone should be considered when interpreting force generating mechanisms. However, as the potential inhibiting effect of the urothelium on smooth muscle contractility was found in multiple bladder regions¹³¹ this modulating effect might be negligible, when investigating locational and directional differences in biomechanical properties of tissue strips from multiple bladder regions.

An advantage of passive parameters determined within this study, compared to the series of studies^{70,79,80} on passive bladder tissue is that the experiments were conducted on the functionally intact tissue (which was approved by the performance of active muscle contractions over the complete period of experiments) at physiological temperatures of 37°C.

2.4.1 Detrusor muscle properties – comparison with the literature

Considering $SMC_{stretched}$, the mean maximum stress of the pig detrusor muscle was about 165 kPa and in agreement with maximum stress values typically generated by smooth muscles^{85,136–139}. When dividing strip force by whole strip CSA – as frequently performed in tissue strip studies – the mean p_{act} (35.2 ± 6.8 kPa) is similar to the stress values observed in previous porcine bladder experiments^{90,125}. However, the p_{act} values in this study are higher compared to a previous study on porcine bladder strips using the same set-up⁷⁶. This discrepancy can be explained by the determination of the CSA at L_S ⁷⁶ in contrast to L_0 (present study). As tissue strip is stretched less at L_S compared to L_0 , CSA is larger at L_S , resulting in lower p_{act} values. However, as F_{im} is produced at L_0 , normalization to $SMC_{stretched}$ at this length is recommended.

Optimal muscle length L_0 of $3.07 \pm 0.28 L_S$ was similar compared to other studies on the detrusor muscle from pig^{73,75,76} and other mammals⁷². The extrapolated range at which the muscle produces forces (0.138 to $2.17 L_0$) was slightly higher than usually found in smooth muscles (typically ranging within 0.2 to $2 L_0$ ^{43,44,140,141}). However, maximal shortenings below $0.2 L_0$ have also been reported for rabbit urinary bladder⁸⁵ or dog tracheal muscle¹⁴². The FLR exhibits a typical bell shape as reported by previous studies on smooth muscles. Passive forces at L_0 of about 27% F_{im} comply with previous experiments on smooth muscles^{44,76,141}. Mean $curv$ factor (0.371 ± 0.144) is within the range of 0.1 – 0.5 normally found in smooth^{44,76,86,141–143} and skeletal muscles¹⁴⁴. The average v_{max} of $0.071 \pm 0.017 L_0/s$ is within the range of values of 0.04 – $0.35 L_0/s$ observed in visceral smooth muscles from the pig^{44,73,76,86,145}.

2.4.2 Active urinary bladder properties – locational and directional dependencies

The detrusor muscle, regardless of location and direction, exhibited a homogeneous shape of the FLR, demonstrating no differences in either w_{asc} , w_{desc} or L_0 (**Figure 10a**). Moreover, the FVR did not differ as v_{max} and $curv$ were similar across all investigated groups (**Figure 10b**). This is in contrast to the results of Pel et al.¹⁴⁶, who report differences in v_{max} (about 20%) and $curv$ (about 50%) of muscle fiber bundles, dissected from the outer and inner layer of the porcine detrusor

muscle (apex). These differences might be based on the different methods used. In the study of Pel et al.¹⁴⁶, FVR was determined by a series of isokinetic ramps at different shortening velocities, and velocity values were plotted against force values at the end of the ramp. At this point, the rate of force decrease was still very large, which might strongly influence measurements and, thus, fitting of v_{max} . Furthermore, FVR data include the force range of 1 to 0.2 F_{im} corresponding to a velocity range of 0 to 0.5 v_{max} , which impedes the determination of v_{max} and $curv$. In contrast, FVR was determined in the present study by performing a series of isotonic and isometric contractions^{76,144} covering a larger force range (1 to 0.1 F_{im}) corresponding to a larger velocity range (0 to 0.7 v_{max}), and therefore, allowing a more valid determination of $curv$ and v_{max} .

On the other hand, the p_{act} values investigated in this study showed dissimilarities, whereby higher values were observed in the longitudinal direction. A recent study analyzed the FLR of isolated detrusor strips from the dorsal apex and also observed higher p_{act} in longitudinal direction⁷⁵. These results can be explained by our histological analysis, yielding a higher amount of $SMC_{stretched}$ in the longitudinal direction compared to the circumferential direction. Normalization of active forces by the CSA of fibers in line with the strip direction yielded no differences of muscle stress between longitudinally and circumferentially oriented smooth muscle fibers. Smooth muscle fibers can be categorized into fast “phasic” or slow “tonic” types³⁵, which differ, among other properties, in contractile kinetics^{147,148}. The outcomes of this study imply that the detrusor muscle consists predominantly of the “phasic” smooth muscle type, which is in agreement with Boberg et al.³⁶, whereby the distribution between “phasic” and “tonic” muscle fibers is uniform across the bladder.

Morales et al.¹² examined the microstructure of tissue strips at L_S from identical locations of porcine urinary bladder in detail. They observed an inner and outer sublayer of smooth muscle fibers of almost similar thickness and a section in between, showing the high dispersion of orientation. Furthermore, these authors determined a more perpendicular alignment of muscle fibers on the dorsal side, but a more oblique orientation with a longitudinal predominance on the ventral side. A rather longitudinal arrangement of smooth muscle cells is in agreement with our observations of higher p_{pass} , p_{act} , and $SMC_{stretched}$ in the longitudinal compared to circumferential direction (**Figure 12**). Although the oblique and predominantly longitudinal muscle fiber

orientation was observed ventrally ¹², we did not find any significant differences in the muscle properties between the ventral and dorsal side.

2.4.3 Passive urinary bladder properties – locational and directional dependencies

We found higher p_{pass} in the trigone compared to the body (**Figure 12c**). Collagen is the major contributor for passive stress in the bladder at high stretch levels ⁸². Several studies examined the relation between passive bladder properties and collagen content and collagen orientation for different bladder regions. Morales et al. ¹² explained higher passive forces in the trigone by increased collagen content. This finding was further supported by Korossis et al. ⁷⁰, reporting an increased network of collagen in the trigone.

Our data show higher p_{pass} in the longitudinal than in circumferential direction (**Figure 12b**). Some studies observed higher passive stress values in longitudinal ^{12,70,78} and others in circumferential ^{75,79,80} directions. The corresponding amount and orientation of elastin and collagen were mainly discussed to interpret the findings. Differences in the methodology of previous studies, however, make comparisons rather difficult. A detailed overview of this discrepancy has been made recently ⁷⁵. Morales et al. ¹² have concluded that higher passive stress examined on longitudinal tissue preparations can be explained by the rather longitudinal smooth muscle orientation. Our results of higher p_{pass} in the longitudinal direction agree with this observation. However, a recent study conducted uniaxial tests on isolated detrusor strips and observed circumferential strips to show greater passive stress values ⁷⁵, performing isokinetic ramps.

2.4.4 Functional and physiological relevance

The detrusor muscle shows no differences in contractile properties across the porcine bladder and might be interpreted as one phasic muscle, which contracts uniformly to void urine over a short period.

At the same time the urethra, which on the other hand has been shown to contain tonic smooth muscle fibers^{145,149}, relaxes during micturition, and contracts afterward, thereby initiating a new filling process. Unlike the stomach, which autonomously stores, digests, and transports its content, the urinary bladder is (as a complete organ) either in the process of being filled or being emptied. Thus, there seems to be no requirement for functional or locational differences of the detrusor muscle on the whole organ level.

Nonetheless, a predominant longitudinal orientation of smooth muscle cells might not only induce higher stiffness of the bladder along the apex to trigone line but also increase active stress. *In vivo*, the bladder is suspended dorsolaterally through the *ligamenta vesicae lateralia* and ventrally through the *ligamentum vesicae medianum* (**Figure 9a**). All three ligaments attach along the apex to trigone line. Hence, higher stiffness in the longitudinal direction might reduce their straining during bladder expansion¹². Furthermore, as the urethral orifice is located above the bladder in the pig, higher active stress might be required longitudinally to successfully propel urine (against gravitational force) out of the body¹². However, it should be noted that due to the upright posture of humans, the bladder position is different and the urethra is situated on the deepest point of the bladder, facilitating the release of urine. This might lead to differences in bladder microstructure between humans and pigs. Moreover, other external forces, such as pressure exerted by neighboring organs might influence micturition under physiologic conditions. In addition to the anisotropic and heterogeneous material properties of the bladder, such effects should be integrated into computational whole organ models⁷⁵ to better understand *in vivo* bladder functioning or to predict functional implications of medical treatments or surgery.

2.5 Conclusion

We examined passive and active properties of bladder tissue strips depending on their location (ad, av, bd, bv, td, tv) and their direction (longitudinal vs. circumferential). Although the bladder's microstructure was found to be both anisotropic and heterogeneous¹², differences in the biomechanical properties (p_{act} , p_{pass} , $SMC_{stretched}$) appear more pronounced depending on the direction of the strip. Higher active and passive stress in the longitudinal direction can be explained

by a more longitudinal arrangement of muscle fibers. Locational differences were only observed for p_{pass} (highest in the trigone). As we found no differences in the contractile behavior of tissue strips from different bladder locations and directions, the detrusor muscle seems to contain a homogeneous and isotropic distribution of predominantly phasic smooth muscle fiber types.

The results of this study will likely contribute to the development and validation of realistic three-dimensional models of the urinary bladder. Bladder models, including biomechanical and structural data, are the base for advancement in the medical understanding and treatment of bladder diseases. For example, bladder augmentation surgery involves an enlargement of the bladder by cutting open the bladder and sewing in a patch of tissue from other organs, such as the intestine or ureter¹²⁰. Bladder functioning will depend on the biomechanical properties of the replacement tissue. Our data will help to develop and prove potential replacement tissues regarding their biomechanical properties. Furthermore, bladder models might be used at the preoperative stage to predict the functional effects of medical operations or treatments (e.g., removal of tumorous tissue, changes in tissue properties due to inflammatory diseases).

2.6 Author contributions

Tobias Siebert, Markus Böl, and Andre Tomalka conceived and designed the experiments. Mischa Borsdorf and Andre Tomalka performed the experiments on biomechanical properties; Enrique Morales-Orcajo performed the histochemical analysis. Mischa Borsdorf, Andre Tomalka, Norman Stutzig, and Tobias Siebert analyzed the data and interpreted the results. Mischa Borsdorf prepared the figures. Mischa Borsdorf, Andre Tomalka, Norman Stutzig, and Tobias Siebert drafted the manuscript; all authors edited, revised and approved the final version of manuscript

3 On a coupled electro-chemomechanical model of gastric smooth muscle contraction

3.1 Introduction

As one main part of the gastrointestinal tract, the stomach is a J-shaped, sac-like hollow organ that is attached proximally to the abdominal esophagus and distally to the duodenum and has three main tasks^{25,27}: To act as reservoir for ingested food and to release it into the duodenum, to secrete acids and enzymes, initiating protein digestion and neutralizing undesirable bacteria in the ingested food, and to mechanically churn ingested food and add gastric juice and thus, generating chyme to be a mixture of liquefied consistence. From the mechanical perspective, during storage and emptying, lasting up to 2 h¹⁵⁰, the stomach undergoes significant deformations¹⁵¹. Interestingly, after emptying, the stomach's shape returns completely back into its reference shape. This recoverable characteristic is facilitated by the microstructure of the stomach wall (SW), which consists of several layers (from the inside out): The tunica mucosa, tunica submucosa, tunica muscularis, and serosa layer, see also **Chapter 3.2.1**. These different layers vary significantly in thickness, waviness, and fiber orientation depending on the stomach's position, and thus, build a 'smart' load transferring system. However, this load transferring system can be considerably disturbed by various diseases^{152–157} that are among the most important causes of morbidity in industrialized countries.

To understand the stomach's functions in health and disease, experimental investigations are needed which are in turn essential as input data for the development of realistic three-dimensional models. Overall, the experimental studies can be categorized into two types of analyses: The first characterizes the mechanical behavior of the whole organ and the second type includes axial and biaxial experiments at the tissue strip level. To study the mechanical function of the stomach as a whole organ, observations on stomachs during filling and emptying have been realized by applying gastro-dynamic tests in different species with and without utilizing a gastric barostat^{54,151,158–165}. In the context of these investigations, quantities such as the flow rate, pressure, and volume relationships can be determined to be adequate clinical indicators with respect to stomach-related

medical conditions. While the advantage of these experiments lies in their applicability as valuable diagnostic tools in daily clinical practice, wall tissue properties, as layer-specific characteristics, cannot be directly determined. To determine those passive wall properties, axial tension^{94–96,166} and compression¹⁶⁷ as well as biaxial tension gastric strip experiments^{16,93} can be found in the literature. Regional variations in mechanical behavior were considered by conducting position-dependent experiments^{16,93–96}. Additionally, by realizing orientation-dependent axial experiments^{94–96,166}, the anisotropic mechanical character was studied. Further, layer-specific mechanical characteristics were studied by Zhao et al.⁹⁵ and Jia et al.⁹⁴.

In addition to the aforementioned studies on the experimental characterization of the passive, mechanical behavior of the SW, experimental studies were also performed to determine the active contraction behavior, reaching from isolated muscle cells^{14,168–170}, over tissue strips^{44,143,171}, to those on entire organs¹⁷². Basically, isolated muscle tissue can be activated by electrical stimuli^{44,137,143,173–175}, the administration of hormones¹⁷⁶, neurotransmitters¹⁷⁶, and mechanical stimuli¹⁷⁷. In case of an electrical stimulation, the isolated tissue specimen located within a basin filled with physiological solution is fixed between two electrodes and circulated around a physiological nutrient solution. Thereby, this kind of muscle activation provides reproducible tetanic contractions for stomach smooth muscle¹⁴³. The outcome of most of these studies are potential-time relations. However, especially for model developments of approaches aiming to describe and predict the excitation-contraction characteristics of smooth muscle (SM) tissue, active force-velocity and active force-length relationships^{44,137} are indispensable. Another option is the activation of the entire organ. Peristaltic contractions may be triggered, e.g., by nerve stimulation of the parasympathetic vagus nerve^{172,178}. Furthermore, gastric contractions may be induced by stimulation of the transmural nerves^{178,179} and the administration of a defined bolus¹⁸⁰ or fluid volumes^{181,182}. In studies on isolated stomachs^{178,182} of guinea-pigs, rats, and cats, the intraluminal pressure development in isovolumetric contractions as well as the dispensed fluid volume at gastric emptying against a constant pressure (isobar) was analyzed. Following¹⁸³, *in-vivo* studies in living animals deal with the measurement of rhythmic gastric activity by means of implanted electrodes, influencing this activity, for example, by external stimulation¹⁸⁴ or internal mechanical stimuli by administration of test meals¹⁸⁰. However, in a number of studies on various species, the barostat

is used to analyze pressure-volume relations for evaluation of tone, tension, and compliance in the stomach^{63,158,185–187}.

In contrast to the various experimental analyses, only a few theoretical models are available to quantify the entire observed experimental findings, i.e., the active, electro-chemomechanical contraction behavior of the stomach. Therefore, a brief overview of existing approaches to model active muscle contractions, with a strong focus on active SW behavior, is given. At a microscopic level so-called cell models^{105,168,188–198} describe fundamental processes of the mechano-electrochemical contraction. However, all models lack a complete description of the entire process. While most approaches only consider the electrical field, the modeling concepts of Corrias and Buist^{191,192} and Yeoh et al.¹⁹⁰ use the electrical and calcium field whereby only one model describes the dependence of the mechanical response on the calcium field¹⁹⁶. In general, modeling the electro-mechanical coupling of smooth muscle tissue is prominent in particular for the cardiovascular system. Several contributions analyzed the effect of tissue deformation on conductivity and ion concentration as shown in Panfilov et al.¹⁹⁹, Cherubini et al.²⁰⁰ and Göktepe and Kuhl²⁰¹. A very popular method to represent the active state of the muscle bases on a constitutive formulation for the active stress. Although allowing high flexibility to reproduce the observed experimental behavior, this comes at the cost of numerical stability when the mathematical formulation of the active stress does not fulfil certain requirements²⁰². An alternative approach is the active strain method, which considers the decomposition of the deformation into an active (inelastic) and an inactive (elastic) part. Using the standard strain energy function of the inactive material response the active strain method is mathematically more robust. In addition, the separate inelastic deformation is more consistent with the mechanism of sarcomere contraction²⁰³. However, it is also more rigid to capture the physiological behavior of the inactive and active material state²⁰². In contrast to cardiovascular systems, little has been reported on the electro-chemomechanical modeling of stomach smooth muscle contraction with regard to three-dimensional boundary value problems. Even after an intensive literature research, only one model by Akhmadeev and Miftahof^{116,117} could be found describing the complete electro-chemomechanical contraction process inside stomach tissue. However, the model contains a variety of material parameters and constants that have not been identified experimentally. In

another approach by Brandstaeter et al. ²⁰⁴, an electro-mechanical constitutive framework of gastric motility modeling by including pacemaker electrophysiology and smooth muscle contractility was presented. Inter alia, the authors realized three-dimensional simulations on a very simple tube-like stomach to demonstrate the general ability of their modeling approach. Finally, in contrast to the aforementioned modeling approaches, various multi-scale models focusing on the description of the electrophysiology of the stomach that do not consider fields other than the mechanical field can be found in the literature ^{103,106–111,205}. For a comprehensive overview on electrophysiological models, the reader is referred to Du et al. ²⁰⁶.

In this study, a three-dimensional multi-field model for the description of gastric motility is proposed. We present an active stress formulation, where the active part of the stress tensor incorporates information about the electrical activation of the smooth muscle cells (SMC) by pacemaker activity of the interstitial cells of Cajal (ICC), the voltage-induced calcium increase in the SMC, and the resulting generation of force. To enhance the predictive power of the presented modeling concept, appropriate active and passive model parameters are identified based on experiments performed on porcine stomach tissue strips.

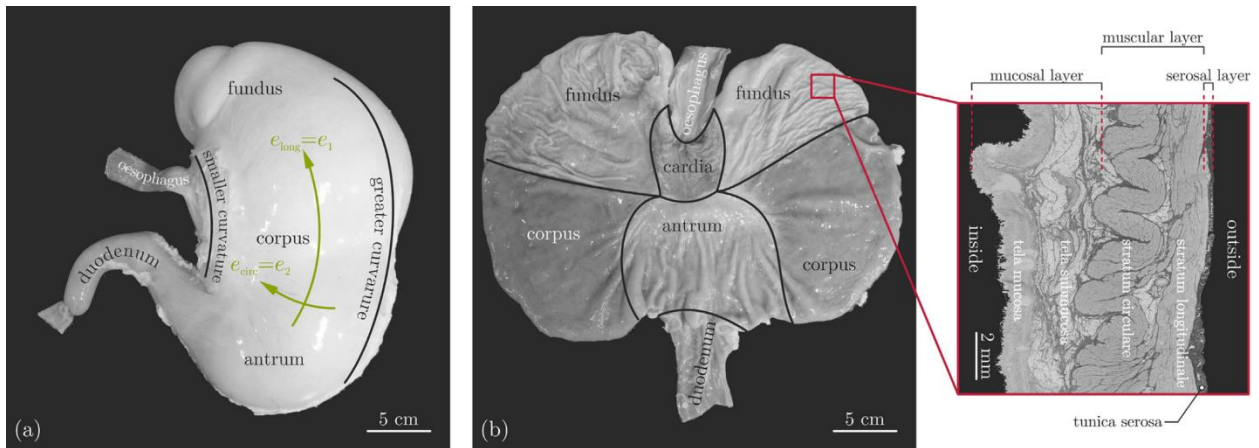


Figure 14. Gross anatomy of the stomach: (a) Inflated porcine stomach and (b) opened at the greater curvature with position-dependent histological cross-sectional presentations stained with Picro-Sirius red. (For interpretation of the references to color in this figure legend, the reader is referred to the web version of this article.) Figure reproduced with permission from Elsevier.

3.2 Structural, functional, and bio-chemophysical aspects of stomach soft tissue

3.2.1 Structure of the stomach wall

The stomach, located in the epigastric and left hypochondriac region of the abdomen, can be anatomically divided into three regions (from cranial to caudal): The fundus, corpus, and antrum (**Figure 14**). From the microstructural point of view, there exist large differences between these regions, cf. enlargement in (**b**). However, generally, the SW consists of three main layers (from the inside out): The mucosal layer, muscular layer, and serosal layer. Histologically, the mucosal layer, consisting mainly of a network of collagen fibers, can be roughly subdivided into tunica mucosa and tunica submucosa. For a detailed description of the different layers, the reader is referred to Bauer et al.¹⁶. Particularly striking is the wrinkle structure of the tunica mucosa. These gastric folds, cf. **Figure 14b**, caused by the smooth musculature of the lamina muscularis mucosae, serve to enlarge the surface of the gastric mucosa. Via connective tissue the tunica mucosa is linked with the muscular layer, which in turn consists of two layers, the stratum circulare and the stratum longitudinal (**Figure 14b**). Between the muscle layers lies the plexus myentericus, a network of nerves that control the muscular contractions of the tunica muscularis. The outer covering layer of the stomach is formed by the tunica serosa. As the serosal layer is relatively thin and has, e.g., in case of the urinal bladder, almost no influence on load-bearing processes⁸⁰, this layer is neglected within the present modeling approach, cf. **Chapter 3.5**.

3.2.2. Gastric reservoir and antral pump - functional units of the stomach

Based on the stomachs three main functions, described in **Chapter 3.1**, functionally, the stomach is frequently divided into two regions^{114,155}: The gastric reservoir (consisting of the fundus and the upper portion of the corpus), which performs mostly tonic contractions, and the gastric pump (consisting of the distal part of the corpus and the antrum), which performs primarily phasic contractions.

The reservoir function is reached through the flexible volume of the human stomach, which can expand to volumes of up to 2–4 liters^{150,207} without resulting in a significant increase in internal pressure^{182,208}. In the case of an empty stomach, the walls are collapsed and pressed tightly against

each other owing to contractions²⁰⁹. In this situation, the stomach features almost no cavities, and only the fundus is filled with gas²¹⁰. The incoming food is stored in the gastric reservoir, whereby the newest food lies closest to the esophageal opening, and oldest food is located nearest the greater curvature within the fundus²¹¹. When the food collects at one point, the distension causes relaxation of the SW in the previously contracted fundus. Herein, a high gastric tone enabled a larger filling without increasing the internal pressure of the organ. This process is called gastric accommodation and lasts approx. 15 min after ingestion²¹². Hereafter, the proximal stomach gradually regains its gastric tone, leading to a steady reduction in the volume of the upper half of the stomach and a reduction in the capacity of the stomach, resulting in its emptying. The content will be gently pushed into the distal antral pump^{159,213}. Liquid content will be immediately forced out of the stomach, while solid content will be retained by the pylorus.

In contrast to the proximal stomach, where no mixing occurs^{113,214}, the distal stomach serves as a muscular pump which grinds the food and transports it to the pyloric sphincter using strong peristaltic contraction waves¹¹⁶. As soon as food enters the distal part of the stomach, peristalsis begins²¹¹. The contraction waves start in the proximal corpus at the greater curvature as shallow indentations of the SW. As they move to the antrum and pyloric sphincter, they get stronger. In the antrum, the strongest contractions mix and grind the food into small particles until it is liquified enough to be emptied into the duodenum. The waves occur in a regular pattern, approximately three waves in a minute traveling at a rate of about 2.5 mm/s, with three or four waves occurring at the same time^{209,215}.

3.2.3. Electro-chemomechanical coupling process of gastric contraction

In the present work, a modeling approach considering two pathways is used to investigate gastric smooth muscle excitation-contraction (see **Figure 15**): An electro-chemical and a mechano-electrochemical pathway. Essential for the coordination of peristaltic contraction waves

in the distal SW is the underlying concept of smooth muscle activation, in which two types of cells, i.e., the interstitial cells of Cajal (ICC) and smooth muscle cells (SMC), play key roles.

According to Sanders et al. ²¹⁶, the ICCs work as pacemaker cells and generate the electrical slow waves that create the oscillations in the cell membrane potential ϕ_{ICC} . In the electro-chemical pathway, ϕ_{ICC} leads to the depolarization of the SMC membrane.

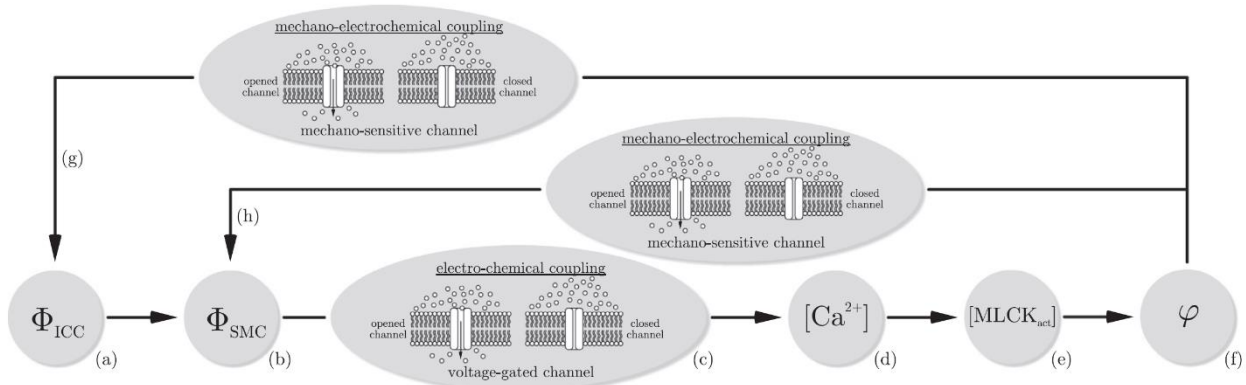


Figure 15. Electro-chemomechanical ((a) to (f)) and mechano-electrochemical ((h) and (g)) coupling pathways of gastric smooth muscle contractions. Four fields are considered, namely, the membrane potentials of the interstitial cells of Cajal ϕ_{ICC} and smooth muscle cells ϕ_{SMC} , intracellular calcium ion concentration $[\text{Ca}^{2+}]$, and deformation ϕ . Figure reproduced with permission from Elsevier.

In turn, a second electrical potential ϕ_{SMC} is generated (see **b** and **Remark 1**). In the SMC, each slow wave cycle of the cell membrane will set the SMC into a state with a high open-probability of the voltage-gated dihydropyridine-sensitive L-type Ca^{2+} channels ²¹⁷ (c). Consequently, extracellular free calcium ions (Ca^{2+}) flow into the cell, leading to an increase of the intracellular calcium ion concentration ($[\text{Ca}^{2+}]$). Ca^{2+} is involved in the activation of the enzyme myosin light chain kinase (MLCK), whose activity determines the contractile response of the phasic smooth muscle in the stomach, cf. (f). Thus, the coupling of $[\text{Ca}^{2+}]$ and the generation of a contraction ϕ is additionally regulated by the concentration of activated myosin light chain kinase ($[\text{MLCK}_{\text{act}}]$), described by the extended Hai-Murphy model (Supplementary Kinetics by Gajendiran and Buist ¹⁹⁶).

The electrical slow waves are always present ²¹⁶, but additional neural or mechanical stimuli need to be present for the slow waves to result in a contraction, activating the debilitating process of gastric peristalsis only when food is present ^{218–221}. Thus, for the second, mechano-electrochemical pathway, a contraction/relaxation triggered by a stretch of the SW is considered. ICCs as well as SMCs contain mechanosensitive ion channels ²¹⁷, which open during cell stretching. For example, the opening of stretch-activated, non-selective cation channels can lead to an influx of positive charged ions, depolarizing the cell membrane ³⁸. In the ICCs, the response can be an increase in the slow wave frequency (**g**) ²²². According to Huizinga and Lammers ²²³ and Johnson ²²⁴, in the SMCs, the stretch signal causes an increase in the plateau potential (PP) (**Figure 16b**) of the slow waves above the mechanical threshold to be the value of the membrane potential where contractions start to occur, which is approximately at -40 mV ⁵⁵. This increases the amplitude of the SMC slow waves, cf. (**h**). While (**g**) affects the open-frequency of the voltage-gated channels in the SMC, (**h**) influences their open-duration. As a consequence, a greater amount of calcium flows into the SMC, with increasing frequency, leading to stronger and more frequent phasic contractions in the distal stomach caused by stretching of the SW.

In contrast to the distal part of the stomach, a stretch in the fundus causes a decrease in the electrical tone in the SMC, see **Remark 1**, followed by a long closing-phase of the voltage-gated channels. The result is a relaxation of the proximal SW, leading to a larger filling to accommodate the incoming meal, as indicated in **Chapter 3.2.1**.

Remark 1 (Location-dependent characteristics of ICCs and SMCs). ICCs are located between and within the muscle layers, and are connected to each other, consequently building an electrically coupled network. At the isolated cell level, ICC slow waves feature different frequencies, depending on the location of the cell inside the SW. ICCs, generating slow waves with the highest frequency, are located in the proximal corpus at the greater curvature (see the red area in **Figure 16a**). Towards the antrum, the individual frequencies reduce (black curves in **a**). In the electrically coupled ICC-network, the slow waves in the ICCs adapt to one dominant frequency in a process called entrainment (red curves in **a**). Thus, for example, in the human stomach, a dominant slow wave frequency of 3 cpm, which is similar to the highest frequency at the dominant pacing site, can be measured ^{101,225}. Owing to the decreasing frequency gradient, the direction of the slow

waves is determined. Because the slow waves propagate faster in the circumferential direction ¹⁴³, they move in ring waves from the dominant pacing site towards the antrum and stop at the entrance of the duodenum. Contractions can only occur at the peak of a slow wave. In this way, they organize the spatio-temporal coordination of the peristaltic contraction waves ¹¹¹ by setting the frequency of the gastric peristaltic waves, their velocity, and their direction of propagation.

In contrast, SMCs need an input stimulus to trigger contractions. The ICCs are electrically coupled to the SMCs via gap junctions; therefore, slow waves can propagate to the neighboring SMCs ²²⁶. This coupling is relatively weak compared to that in the ICC-network, i.e., the slow wave amplitude in the SMC drops ²¹⁶, making the ICC-network important with respect to propagation. Muscle cells building electrical connections between each other and to ICCs via gap junctions are also referred to as electrical syncytium, allowing for the electrical propagation from muscle fiber to muscle fiber. One key feature is the gradient of the SMC resting membrane potential (RMP) of the slow waves along the longitudinal axis of the stomach ^{105,197} (**Figure 16b**). The RMP is the most negative potential occurring between the peaks of two slow waves. Generally, the fundus features no electrical oscillatory activity. As the RMP of the SMC in the fundus is already above the mechanical threshold ²¹³, the wall of the proximal stomach can generate a tonic contraction. Following (**b**), in the distal stomach, the RMP gets more negative from the corpus to the antrum. In the proximal corpus, the slow waves are relatively small in amplitude, which matches with the shallow indentations of the SW pushing the content from the reservoir into the antral pump. In the antrum, the RMP is the most negative, and consequently, the slow wave amplitude is the highest, being in line with the strong contractions in this region. Summarizing, the ICCs are responsible for setting the SMC in a state where contractions are easy to trigger. SMCs determine the strength of phasic contractions by their slow wave amplitude and RMPs ²²⁷.

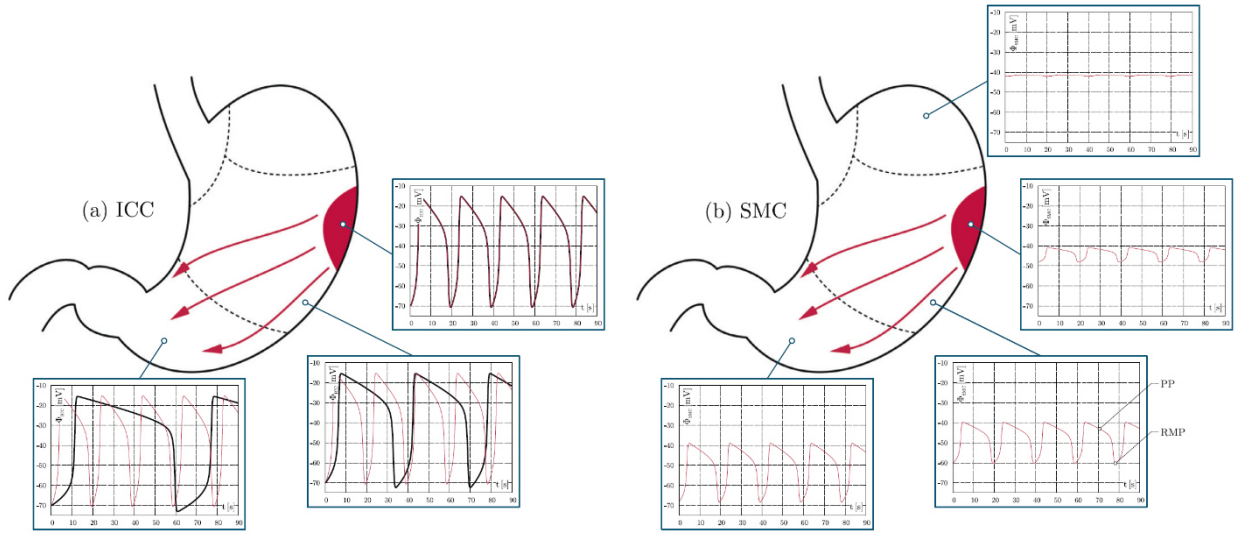


Figure 16. Illustration of the membrane potentials of the ICC and SMC at different locations for the deflated stomach at rest: (a) Slow wave behavior of isolated ICCs (black curve) and when entrainment happens in an ICC-network (red curve). (b) Slow waves of the SMCs featuring a gradient in the resting membrane potential. Note that slow waves are modeled with the FitzHugh-Nagumo type equations. (For interpretation of the references to color in this figure legend, the reader is referred to the web version of this article.) Figure reproduced with permission from Elsevier.

Table 4. Active and passive experiments conducted in this study. n defines the number of considered strips, and A_0 denotes the mean cross-sectional area of the samples in its undeformed configuration. Table reproduced with permission from Elsevier.

		n	A_0 [mm ²]	active	passive
entire wall structure	longitudinal	5	98.03 ± 14.06	-	✓
	circumferential	5	100.17 ± 19.95	-	✓
tunica muscularis	longitudinal	5	54.31 ± 9.54	✓	✓
	circumferential	5	74.65 ± 8.87	✓	✓

3.3 Materials and methods

3.3.1 Ethical approval

The study was exempted from ethical committee review according to national regulations (German Animal Welfare Act) as porcine stomachs of healthy, female domestic pigs were obtained from a slaughterhouse immediately after animal sacrifice.

3.3.2 Tissue strip experiments

For determination of the active and passive, layer-specific and orientation dependent mechanical characteristics of the SW, twenty (n=20) fresh porcine gastric tissue strips dissected from 20 stomachs of female domestic pigs (*Sus scrofa domestica*, age: approx. 6 months, mass: approx. 100 kg) were prepared within 60–90 min after animal sacrifice. Experiments were grouped into strips featuring the entire wall structure and strips whose tunica mucosa had been removed so that only the tunica muscularis remained for testing (**Table 4**).

The experimental set-up, handling, and preparation of smooth muscle tissue have been described earlier^{44,76,228}. Briefly, immediately after sacrifice, a predefined piece of smooth gastric tissue (30 ×30 mm) was dissected from the ventral fundus of the proximal stomach. For the active experiments, the tunica mucosa was separated from the strip. During this procedure, care was taken to ensure the tissue strip did not make contact with gastric acid to avoid smooth muscle degeneration. Subsequently, small tissue strips (0.6 ±0.14 g) of 16 ×8 mm in longitudinal (n=5) orientation (i.e., parallel to the direction of the gastric serosal fold and parallel to the greater curvature, see **Figure 14**) and in circumferential (n=5) orientation (perpendicular to the longitudinal orientation) were prepared from the predefined tissue sample of the fundus. The gastric strips were mounted vertically in an Aurora 805A *in-vitro* muscle apparatus between an alligator clip and two cannula hooks which were located at the bottom of the apparatus. The clamp was attached to a dual mode lever arm system (Aurora Scientific 305C-LR). Starting from a very short strip length (clearly sagging), the strip was passively lengthened through an isokinetic ramp (5 mm/min) until a passive force of 5–10 mN was reached. After finishing the ramp, the strip was kept at this length, while the passive force development settled at a negligible baseline value (<1

mN). The length of the strip between the clamp and attachment hooks was determined with a digital sliding caliper, and was defined as the slack length (L_S). The mean slack lengths of the longitudinal and circumferential strips were 13.0 ± 1.5 mm and 11.7 ± 1.6 mm, respectively.

During the period of preparation, handling, and testing, the gastric tissue strips were kept in an aerated (95% O_2 and 5% CO_2) modified Krebs solution¹⁴³ in (mM): 124 NaCl, 5 KCl, 2.5 $CaCl_2$, 15 $NaHCO_3$, 1.2 KH_2PO_4 , 1.2 $MgSO_4$, and 10 $C_6H^{12}O_6$. The temperature of the Krebs solution was 4° C. The tissue strips were electrically stimulated (Aurora Scientific 701C) with alternating pulses with a current, frequency, and pulse width of 1 A, 100 Hz, and 5 ms, respectively^{125,228} via two platinum field electrodes (65 ×2 mm) placed at each side of the strip. The experiments were performed at a constant solution temperature of 32 ± 0.1 °C to avoid spontaneous muscle activity²²⁹. Furthermore, the tissue samples proved to be very stable at this temperature, so that active experiments could be carried out over longer periods of time^{44,230}. After an equilibration period of 30 min at L_S , the strips were stimulated isometrically for about 23 s every 7 min until a steady state force (deviation < 5% of maximum isometric force F_{max}) was reached⁴². Intervals of 7 min were chosen to avoid muscle fatigue effects. Following⁴⁴, within each interval, a preconditioning protocol of 150 cycles was applied with a frequency of 1 Hz (amplitude: 0.03 strip length). To investigate the active force-length relationships, a series of 18–24 isometric contractions (with length increments of 0.1 L_S in ascending order), starting from an initial sample length of 0.8 L_S , were conducted. The active force was calculated as the difference between the maximum total strip force (during stimulation) and the passive force (immediately before stimulation). Details of the experimental procedure are illustrated in the Supplementary **Figure 1**. The same procedure was performed to measure the passive force length- relation of strips with their entire wall structures. Muscular tissue strips were stretched up to passive forces of about 50% F_{max} to avoid muscle damage induced by excessive lengthening. The muscle length at which F_{max} was produced was defined as the optimal muscle stretch λ_{opt} . Based on these force values, the passive force-stretch and stress-stretch relations (**Figure 18**) were determined using the mean cross-sectional areas A_0 specified in **Table 4**.

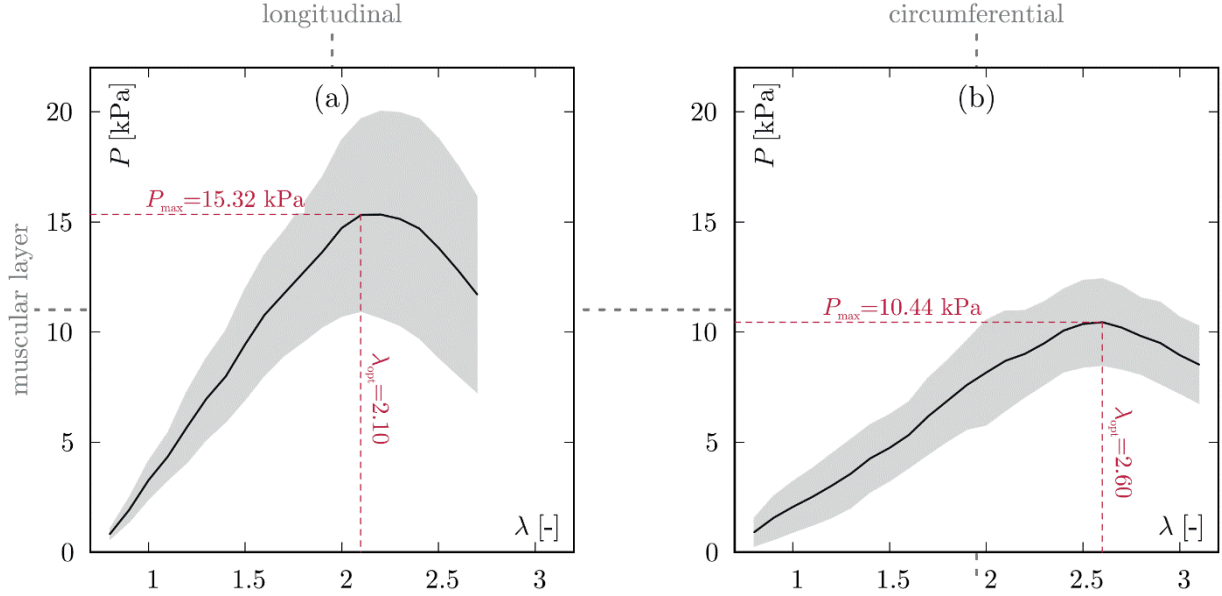


Figure 17. Active stress-stretch responses of 10 gastric muscular tissue samples in the (a) longitudinal and (b) circumferential directions. The solid curves indicate mean values, whereas the shaded areas depict the standard deviations. During all the experiments, the forces F and the strip length changes Δl were measured and converted to engineering stress $P = F / A_0$ (A_0 denotes the average cross-sectional area of the strip measured in the initial and unloaded situations) and stretch $\lambda = 1 + \Delta l / l_0$ (l_0 denotes the length of the strip measured in the initial, unloaded situation), respectively. Figure reproduced with permission from Elsevier.

3.3.3 Statistics

In **Chapter 3.4** the results are presented in terms of the mean and the standard deviations. To determine whether the fiber orientation and the different layers have a significant influence on the active and passive mechanical stresses, Mann-Whitney- U -tests for two independent sample sizes ($m, n = 5$) were performed for each stretch value λ_i . We tested the two groups of the active experiments for direction-dependency, and for direction- and layer-dependency in the passive experiments. With respect to the null hypothesis, stating that the median of both sample sizes is equal, differences were considered as significant based on a confidence level of $\alpha = 0.1$, if $U < 5$.

3.4 Experimental results: direction-dependent, layer-specific stress responses

The mean active stress-stretch responses are provided in **Figure 17** as black curves together with the standard deviations (s.d.), which are presented as grey shaded areas. As the active stress-stretch behavior of smooth muscles is length-dependent, the characteristic key variables are the optimum stretch λ_{opt} and the associated maximum stress P_{max} . By comparing the optimal stretches and stresses in the **(a)** longitudinal ($\lambda_{\text{opt}} = 2.1$ and $P_{\text{max}} = 15.32$ kPa) and **(b)** circumferential directions ($\lambda_{\text{opt}} = 2.6$ and $P_{\text{max}} = 10.44$ kPa), it is noticeable that the optimum stretch in the circumferential direction is larger, whereby a smaller stress is achieved in this direction. Interestingly, the optimal stretch is different in both directions, a fact, which is not the case, e.g., for urinary bladder tissue, see ⁷⁵. Mann-Whitney-*U*-test, as stated in **Chapter 3.3.3**, indicates that the differences in the active stresses for the longitudinal and circumferential directions are statistically significant ($\alpha = 0.1$) for stretch values below 2.4.

Additionally, passive elongation experiments were conducted on complete tissue strips and those only featuring the muscular layer (**Figure 18**). Independent of the orientation, the results are characterized by the typical exponential response. Further, by comparing the mechanical responses of the entire strip (**Figure 14a** and **b**), it can be seen that the material behaves almost isotropically, regardless of whether the stresses or the forces are compared. This is surprising, as the microstructure is clearly inhomogeneous in the fundus (**Figure 14b**). When applying the Mann-Whitney-*U*-test, the null hypothesis cannot be discarded for stretches above 1.6. On the other hand, by comparing the mechanical responses of the muscle layer **(c)** and **(d)**, a certain anisotropic behavior can be seen, which in turn reflects the inhomogeneous microstructure in **Figure 14b**. Therefore, the mucosal layer seems to balance the mechanical anisotropy of the muscularis. However, the direction-dependent difference of the muscular stresses is not statistically significant. Further, while the entire strip and the muscular layer behave similar in the longitudinal direction, there is a statistically significant ($\alpha = 0.1$) difference between both layers for stretches higher than 1.5 compared to the circumferential direction.

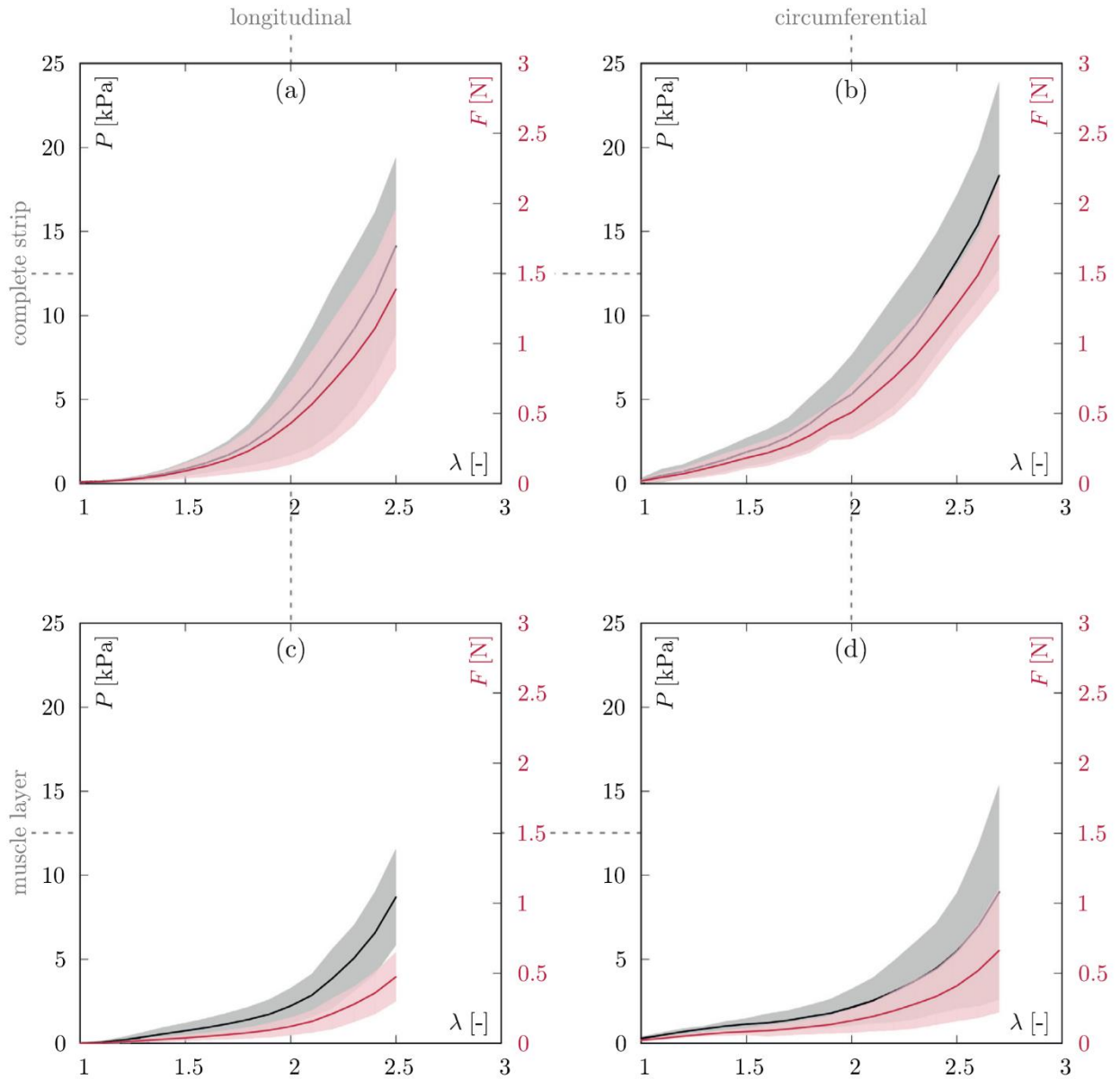


Figure 18. Passive force-stretch (red) and stress-stretch (black) responses of 20 gastric tissue samples. The solid curves indicate the mean values, whereas the shaded areas depict the standard deviations. (For interpretation of the references to color in this figure legend, the reader is referred to the web version of this article.) Figure reproduced with permission from Elsevier.

3.5 Continuum mechanical framework of gastric smooth muscle contraction

3.5.1 Kinematics

Based on general continuum mechanics, we introduce \mathbf{B}_0 and \mathbf{B} as the reference and current configurations of a contractive body, in which the position of a particle is given by the vectors \mathbf{X} and $\mathbf{x} = \boldsymbol{\varphi}(\mathbf{X}, t)$, respectively. Herein, the continuous, non-linear mapping of the body particles from the reference to the current configuration is represented by $\boldsymbol{\varphi}(\mathbf{X}, t)$ and $\mathbf{F} = \nabla_{\mathbf{X}} \boldsymbol{\varphi}(\mathbf{X}, t)$ is the corresponding deformation gradient. The Jacobian $J = \det \mathbf{F} > 0$, the determinant of the deformation tensor, characterizes volumetric changes, and $\nabla_{\mathbf{X}}(\bullet)$ defines the spatial derivative with respect to the reference coordinates \mathbf{X} . Unless otherwise stated, the term ‘tensor’ refers to a second-order tensor.

To incorporate the different fiber directions described in **Remark 2**, we introduce the structural tensors

$$\mathbf{Z}_{C/S} = \mathbf{M}_{C/S} \otimes \mathbf{M}_{C/S}, \quad (1)$$

in the reference configuration to represent the in-wall dispersion of collagen (index: c) and SMC (index: s) with the direction vectors $\mathbf{M}_{C/S}(\mathbf{X})$. The corresponding stretches $\lambda_{C/S}$ can thus be expressed as follows

$$\lambda_{C/S}^2 = I_{4,C/S} = \mathbf{C} : \mathbf{Z}_{C/S}, \quad (2)$$

Herein, $I_{4,C/S}$ denote the scalar valued fourth invariants, and $\mathbf{C} = \mathbf{F}^T \mathbf{F}$ describes the right Cauchy-Green tensor. Note that, unlike the isotropic part in Eq. (14), where the determination of the first in-variant makes use of the isochoric part of \mathbf{C} , i.e., $\hat{\mathbf{C}}$, the formulation of the anisotropic part here is based on the right Cauchy-Green tensor of the total deformation. This modification is necessary due to the formulation of the volumetric part in Eq. (13), which uses a static parameter to maintain material incompressibility. This means that in case of large deformations the isochoric formulation of the anisotropic part would violate the incompressibility condition and even initiate unphysical effects⁷⁵.

3.5.2 Governing equations

Within this work, electro-chemomechanical SM contraction is described by four primary variables, namely the electrical action potential for the ICC $\phi_{\text{ICC}}(\mathbf{X}, t)$ and the SMC $\phi_{\text{SMC}}(\mathbf{X}, t)$, the intracellular calcium ion concentration field $[\text{Ca}^{2+}](\mathbf{X}, t)$, and the mechanical placement $\varphi(\mathbf{X}, t)$. Thus, the electro-chemomechanical state S of a material points' placement \mathbf{X} at time t is given by

$$S(\mathbf{X}, t) = \{\phi_{\text{ICC}}(\mathbf{X}, t), \phi_{\text{SMC}}(\mathbf{X}, t), [\text{Ca}^{2+}](\mathbf{X}, t), \varphi(\mathbf{X}, t)\} \quad (3)$$

The spatio-temporal evolution of these variables is governed by the two field equations, namely one diffusion-type equation of excitation for the electrical potential and the balance of linear momentum.

Excluding any body forces, the balance of linear momentum in the local spatial form reduces to

$$J \operatorname{div}(J^{-1}\tau) = \mathbf{0} \quad (4)$$

which describes the quasi-static stress equilibrium, where $\operatorname{div}(\bullet)$ denotes the spatial divergence, and τ is the Kirchhoff stress tensor. The boundary conditions on the disjoint surface ∂B_φ and ∂B_σ are given by

$$\varphi = \check{\varphi} \text{ on } \partial B_\varphi \text{ and } \mathbf{t} = \check{\mathbf{t}} \text{ on } \partial B_\sigma. \quad (5)$$

The traction vector $\check{\mathbf{t}}$ is defined via the Cauchy stress theorem $\check{\mathbf{t}} = \sigma \mathbf{n}$, where \mathbf{n} denotes the outward surface normal and σ is the Cauchy stress tensor.

For the spatio-temporal description of the ICC membrane potential, the diffusion reaction-type equation

$$\dot{\phi}_{\text{ICC}} - J \operatorname{div}(J^{-1}\mathbf{q}^{\phi_{\text{ICC}}}) - F^{\phi_{\text{ICC}}} = 0, \quad (6)$$

is used. Herein, the material time derivative $(\dot{\bullet}) = \partial(\bullet)/\partial t|_X$ of the action potential ϕ_{ICC} is related to the reference configuration. The term $F^{\phi_{\text{ICC}}}$, defined with respect to the material configuration

and described in detail in **Chapter 3.5.3**, denotes an additional source controlling the activation and inactivation dynamics of the ICC membrane potential.

The flux term

$$\mathbf{q}^{\phi_{\text{ICC}}} = \mathbf{d} \nabla_X \phi_{\text{ICC}}, \quad (7)$$

responsible for the propagation and entrainment of the slow waves within the ICC network relates the spatial gradient of the action potential $\nabla_X \phi_{\text{ICC}}$ via the deformation- and location-dependent anisotropic conductivity tensor

$$\mathbf{d} = d_{\text{iso}} \mathbf{I} + \sum_{i=1}^{n_s} d_{\text{aniso},i} \mathbf{z}_{s,i}^R, \quad (8)$$

additively decomposed in an isotropic and anisotropic contribution. The particular formulation of the conductivity part in Eq. (6) – (8) considers the electric conductivity of $d_{\text{iso}} \mathbf{I}$ as isotropic with respect to the spatial configuration. Consequently, the pull-back of $d_{\text{iso}} \mathbf{I}$ leads to the anisotropic conductivity in the reference configuration²⁰⁰. Based on experimental investigations by Sarna et al.²³¹, the diffusion coefficients $d_{\text{iso}}(\mathbf{X})$ and $d_{\text{aniso},i}(\mathbf{X})$ are location-dependent material parameters controlling the velocity of the slow waves. Additionally, by introducing different coefficients $d_{\text{aniso},i}$ for the considered directions i , the faster propagation of the slow waves in circumferential direction of the smooth muscle fibers can be established. Further, n_s denotes the number of considered directions, \mathbf{I} defines the identity tensor, and

$$\mathbf{z}_{s,i}^R = \frac{\mathbf{FM}_i}{|\mathbf{FM}_i|} \otimes \frac{\mathbf{FM}_i}{|\mathbf{FM}_i|} \quad (9)$$

are the rotated structural tensors. According to the mechanical problem, the field equation of excitation depends on the corresponding boundary conditions

$$\phi_{\text{ICC}} = \check{\phi}_{\text{ICC}} \text{ on } \partial B_{\phi_{\text{ICC}}} \text{ and } q^{\phi_{\text{ICC}}} = \check{q}^{\phi_{\text{ICC}}} \text{ on } \partial B_{q^{\phi_{\text{ICC}}}}. \quad (10)$$

Similar to the Cauchy stress theorem of the mechanical description, the surface flux is defined by the relationship $\check{q}^{\phi_{\text{ICC}}} = \mathbf{q}^{\phi_{\text{ICC}}} \mathbf{n}$.

Although there may be some influences on the ICC and SMC potential¹⁰⁷, we considered no flux in the SMC-network, allowing us to handle the SMC potential as a local variable. As

ϕ_{ICC} basically determines the frequency of the SMC slow waves, we express ϕ_{SMC} by simply rescaling ϕ_{ICC} to adjust the amplitude of the electrical potential in the SMC, see **Chapter 5.3.2** for more details.

Finally, the dynamics of $[\text{Ca}^{2+}]$ inside the SMC are expressed by the evolution equation

$$[\text{Ca}^{2+}] = F^{[\text{Ca}^{2+}]}, \quad (11)$$

relating the time derivation of $[\text{Ca}^{2+}]$ with the source $F^{[\text{Ca}^{2+}]}$ for controlling the calcium increase and decrease in terms of a monodomain formulation.

3.5.3 Constitutive equations

Based on the SWs' microstructure, and with respect to an adequate modelling approach, the SW is associated with three main layers: The (inner) mucosal layer, the (middle) muscular layer, and (outer) serosal layer. In agreement with our experimental experiences, the mucosal and muscular layers are the essential load-bearing parts of the SW. Consequently, only these layers were considered in the modelling approach.

Mucosal layer

The mucosal layer (index: MCL), composed of the tunica mucosa and tunica submucosa, features only passive material characteristics, and its main constituents are elastin (index: e) and collagen (index: c). Consequently, the strain energy function

$$\psi_{\text{MCL}} = \hat{\psi}_{\text{MCL}} + U = \hat{\psi}_e + \hat{\psi}_c + U \quad (12)$$

is decomposed into a mixed contribution ($\hat{\psi}_{\text{MCL}}$), including the components for elastin ($\hat{\psi}_e$) and collagen ($\hat{\psi}_c$). The purely volumetric part

$$U = \frac{K_{\text{vol}}}{4} (J^2 - 1 - 2 \ln(J)) \quad (13)$$

controls the degree of incompressibility by means of the parameter K_{vol} .

Elastin as a load-bearing protein that builds three-dimensional networks with isotropic characteristics is represented by the isotropic Neo-Hookean material model

$$\hat{\psi}_e = \frac{\mu_e}{2} 2 (\hat{I}_1 - 3). \quad (14)$$

Herein, the isochoric first invariant $\hat{I}_1 = \text{tr } \hat{\mathbf{C}}$ is defined as the trace of the isochoric part of the right Cauchy-Green tensor $\hat{\mathbf{C}}$, and μ_e is the shear modulus.

The mechanical behavior of collagen as the second load-bearing protein in the SW is characterized by an exponential stress-stretch relationship along the fiber direction. According to Seydewitz et al.⁷⁵, such anisotropic, non-linear behavior is described by

$$\hat{\psi}_c = \sum_{i=1}^{n_c} f_{c,i} \psi_{c,i}, \quad (15)$$

where the strain energy functions²³²

$$\psi_{c,i} = \begin{cases} \frac{c_{c1}}{2c_{c2}} \left(\exp \left[c_{c2} (\lambda_{c,i}^2 - 1)^2 \right] - 1 \right) & \text{if } \lambda_{c,i} > 1 \\ 0 & \text{else} \end{cases} \quad (16)$$

depend on two material constants, c_{c1} and c_{c2} , weighted in every incorporated direction i with the corresponding fraction $f_{c,i}$. The fraction fulfils the relationship $\sum_{i=1}^{n_c} f_{c,i} = 1$, with n_c to be the number of incorporated directions, see also **Remark 2**. In addition, the tension-compression switch ensures that only fibers under tension contribute to the mechanical response.

Muscular layer

The muscular layer (index: MSL) consists of anisotropic oriented SM coats embedded in the extracellular matrix (ECM). This matrix consists of elastin and collagen forming an isotropic load-bearing network. Thus, based on earlier modelling approaches^{75,233–235}, the strain energy function

$$\psi_{\text{MSL}} = \hat{\psi}_{\text{MSL}} + U = \hat{\psi}_{\text{ECM}} + \psi_s + U \quad (17)$$

is decomposed into a mixed (ψ_{MSL}) and a volumetric contribution (U). While the volumetric part follows Eq. (13), the isochoric contribution is additively decomposed into a contribution for the

anisotropically aligned SM fascicles (ψ_s) and a purely passive contribution ($\hat{\psi}_{\text{ECM}}$) describing the ECM.

For the contribution arising from the ECM, the isotropic Neo-Hookean material model,

$$\hat{\psi}_{\text{ECM}} = \frac{\mu_{\text{ECM}}}{2} (\hat{I}_1 - 3), \quad (18)$$

which depends on only one material parameter, μ_{ECM} , is chosen.

Within the muscular layer, coats of active SM fascicles are oriented in the longitudinal and circumferential directions. In accordance with the active stress formulation, the SM strain energy function reads

$$\psi_s = \sum_{j=1}^{n_s} f_{s,j} (\psi_{s,j}^a + \psi_{s,j}^p), \quad (19)$$

including active and passive contributions, indexed with a and p. Based on the anisotropic character of these coats, the strain energy functions are weighted with SMC volume fractions $f_{s,j}$ in every direction $j = 1, \dots, n_s$, see also **Remark 2**. The passive strain energy functions²³²

$$\psi_{s,j}^p = \begin{cases} \frac{c_{s1}}{2c_{s2}} \left(\exp \left[c_{s2} (\lambda_{s,j}^2 - 1)^2 \right] - 1 \right) & \text{if } \lambda_{s,j} > 1 \\ 0 & \text{else} \end{cases} \quad (20)$$

feature two material parameters c_{s1} and c_{s2} , and are functions of SM fascicle stretches $\lambda_{s,j}$.

In this particular case a Gaussian function mimics the bell-shaped active stress response for which the corresponding active strain energy functions

$$\psi_{s,j}^a (\Phi_{\text{SMC}}, [\text{Ca}^{2+}], \mathbf{C}) = (n_c + n_d) P_{\text{max}} \int \exp \left[-\frac{(\lambda_{s,j} - \lambda_{\text{opt}})^2}{2\xi_s^2} \right] d\lambda_{s,j} \quad (21)$$

depend on $\lambda_{s,j}$, the constant ξ_s , which influences the width of the active stress generation, and the optimum stretch λ_{opt} at which the generated stress P_{max} reaches its maximum value. Furthermore, the strain energy function depends on the chemical degree of activation ($n_c + n_d$) provided by the model in¹⁹⁶, for details see Supplementary Kinetics by Gajendiran and Buist¹⁹⁶.

The electrical source term in Eq. (6) represents the electro- physiology of the ICC. To mimic the membrane potential and the ion current dynamics, we make use of a phenomenological two-variable FitzHugh-Nagumo type model ^{111,236}. In doing so, it is common to express the model equations and variables in terms of dimensionless variables.

The dimensionless potential

$$\phi = \frac{\Phi_{\text{ICC}} - \Phi_{\text{ICC}}^r}{\beta_{\text{ICC}}} \quad (22)$$

is obtained from the ICC membrane potential Φ_{ICC} . Herein, the conversion coefficient

$$\beta_{\text{ICC}} = \Phi_{\text{ICC}}^p - \Phi_{\text{ICC}}^r \quad (23)$$

equals the difference between the plateau potential Φ_{ICC}^p and the resting membrane potential Φ_{ICC}^r of the slow waves in the ICC (**Figure 16**). The formulation of the electric source

$$F\Phi_{\text{ICC}} = \bar{\beta}_{\text{ICC}} F\phi \quad (24)$$

involves the multiplicative decomposition into $\bar{\beta}_{\text{ICC}}$, a temporally normalised scaling factor of β_{ICC} , and the dimensionless electric source

$$F\phi = \kappa\phi(\phi - \alpha)(1 - \phi) - r, \quad (25)$$

to be a function of r , a second so-called recovery variable governed by an additional differential equation

$$\dot{r} = F^r \text{ with } F^r(\phi, r, \mathbf{C}) = \varepsilon(\gamma(\phi - \zeta) - r). \quad (26)$$

Although κ , α , γ , and ζ are constant material parameters controlling the oscillation of the electric potential,

$$\varepsilon = \begin{cases} \varepsilon_0 + \sum_{j=1}^{n_s} f_{s,j} \frac{w_f}{1 + \exp(-u_f * (\lambda_{s,j} - v_f))} & \text{if } \lambda_{s,j} > 1 \\ \varepsilon_0 & \text{else} \end{cases} \quad (27)$$

incorporates additional position and stretch information. Herein, $\varepsilon_0(\mathbf{X})$ is the initial location-dependent value of ε , which defines the ICC slow wave frequency in the absence of mechanical

stimulation, cf. also **Figure 16a**. w_f defines a parameter that, together with u_f and v_f , controls the stretch-dependent frequency ε of the slow waves (see **Figure 15g**).

Because the SMC potential is guided by the ICC potential, in a first approach a simplification of rescaling ϕ_{ICC} to adjust the amplitude of ϕ_{SMC} is used. We obtain the linear relationship

$$\phi_{\text{SMC}} = \beta_{\text{SMC}} \phi + \phi_{\text{SMC}}^r, \quad (28)$$

that links the physical value of the SMC membrane potential ϕ_{SMC} to ϕ with the conversion coefficient

$$\beta_{\text{SMC}} = \phi_{\text{SMC}}^p - \phi_{\text{SMC}}^r, \quad (29)$$

which is the difference between the plateau potential ϕ_{SMC}^p and the resting potential ϕ_{SMC}^r .

The propagation of a negative RMP gradient along the curved longitudinal axis of the stomach inside the SMC-network (**Figure 16b**) implies the initial value of the electrical potential $\phi_{\text{SMC}0}^r(\mathbf{X})$ to be a function of the material coordinates \mathbf{X} . Taking into account the additional location-dependent stretch response of the resting potential described in **Chapter 3.2.3** and illustrated in **Figure 15h**, a simple mixture rule obtained by setting

$$\phi_{\text{SMC}}^r = \begin{cases} \left(\phi_{\text{SMC}0}^r - \sum_{j=1}^{n_s} f_{s,j} \frac{w_a}{1 + \exp(-u_a * (\lambda_{s,j} - v_a))} \right) * (1 - \omega) + \phi_{\text{SMC}0}^r & \text{if } \lambda_{s,j} > 1 \\ \phi_{\text{SMC}0}^r & \text{else} \end{cases} \quad (30)$$

is applied. Herein, the dimensionless function $\omega(\mathbf{X}) \in [0, 1]$ ensures a smooth transition from stretch-induced relaxation in the fundus to stretch-induced contraction in the antrum along the curved longitudinal axis of the stomach. Further, the stretch sensitivity is controlled by w_a , u_a , and v_a , which are potential-like and dimensionless parameters. Unlike the resting potential, the initial value of the plateau potential $\phi_{\text{SMC}0}^p$ remains constant along the curved longitudinal axis of the stomach (**Figure 16b**), and the overall expression for the electric PP, including the stretch-dependent response is

$$\Phi_{\text{SMC}}^p = \begin{cases} \left(\Phi_{\text{SMC}0}^p - \sum_{j=1}^{n_s} f_{s,j} \frac{w_a}{1+\exp(-u_a*(\lambda_{s,j}-v_a))} \right) * (1 - \omega) \\ \quad + \left(\Phi_{\text{SMC}0}^p - \sum_{j=1}^{n_s} f_{s,j} \frac{w_a}{1+\exp(-u_a*(\lambda_{s,j}-v_a))} \right) * \omega & \text{if } \lambda_{s,j} > 1 \\ \Phi_{\text{SMC}0}^p & \text{else} \end{cases} \quad (31)$$

In the undeformed state of the fundus, the PP and the RMP are approximately identical. The potential difference remains constant during stretching, while both values decrease, reducing the tonic contraction to allow relaxation. The potential difference in the stretch-free state of the antrum is more distinct owing to a more negative value of the RMP. Stretching initiates an increase in the PP, which represents an increase in the phasic contraction.

To ensure consistency with the previous **Chapter 3.5.2**, the evolution of $[\text{Ca}^{2+}]$ is considered a pure local problem. As it is assumed that the $[\text{Ca}^{2+}]$ dynamics in the gastric SMC follows a bell-shaped curve ²³⁷, the relationship between the SMC membrane potential and the intracellular calcium concentration is modelled as a gaussian function ⁷⁵

$$F[\text{Ca}^{2+}] = q - k([\text{Ca}^{2+}] - [\text{Ca}^{2+}]_{\text{rest}}) \text{ with } q = q_0 \exp\left[\frac{-\Phi_{\text{SMC}}^2}{2\xi^2}\right]. \quad (32)$$

within the source term of Eq. (11). The constant ξ serves as a degree of freedom to limit the sensitivity of the calcium release to a certain range of the SMC membrane potential. The material parameters q_0 and k control the release and return of the calcium, and $[\text{Ca}^{2+}]_{\text{rest}}$ denotes the resting calcium concentration. Based on experimental investigations, the peak calcium concentration of gastric SMC, which varies from $[\text{Ca}^{2+}] = 0.37 \mu\text{M}$ ²³⁸ to $[\text{Ca}^{2+}] = 0.6 \mu\text{M}$ [75], is reached when the cell is depolarized to $\Phi_{\text{SMC}} = 0 \text{ mV}$. However, Vogalis et al. ²³⁸ stated that the measured $[\text{Ca}^{2+}]$ -values may be underestimated owing to calibration problems, so a slightly higher value was considered. With the maximum calcium concentration, the relationship q_0/k can be determined based on the relation for the stationary maximum calcium concentration

$$[\text{Ca}^{2+}] = \frac{q_0}{k} + [\text{Ca}^{2+}]_{\text{rest}}. \quad (33)$$

It is noted here that the choice of q_0 and k influences the delay between mechanically induced excitation of the SMC and regulation of $[Ca^{2+}]$ during the electro-chemomechanical coupling. For further information, the interested reader is referred to ⁷⁵.

Remark 2 (Fiber orientations). For modeling the mechanical characteristics of the gastric soft tissue, an anisotropic material in which the collagen and the SMC fibers are aligned tangentially to the SW, is considered. For a first approach $n_{c,s} = 2$ fiber directions are considered in each layer, leading to collagen fiber fractions in longitudinal ($f_{c,1}$) and circumferential ($f_{c,2}$) directions for the mucosal layer, and SMC fibre fractions in the longitudinal ($f_{s,1}$) and circumferential ($f_{s,1}$) directions in the muscular layer. This approach represents a highly simplified model of collagen and connective tissue with a discrete fiber dispersion. Since only two perpendicular fiber families are considered, the model may not represent a representative load transfer mechanism of the fiber material. As shown e.g. in ²³⁹ even small changes to the perfect alignment have significant impact on the stresses in the tissue material and therefore to the overall deformation of the stomach wall. A comprehensive histological study has been conducted in ¹⁶, investigating the location-dependent fiber orientation in six in-plane sections of the porcine stomach wall. With this information at hand, physiological fiber directions can be implemented in future works for the whole stomach model.

3.6 Results

This section presents the electro-chemomechanical excitation processes arising in porcine SW tissue under physiological conditions. To this end, three-dimensional simulations of an empty and filled stomach were performed to study the digestive and interdigestive properties of gastric motor activity. If not otherwise specified, the material parameters listed in **Tables 5–7** were identified based on a parameter identification scheme (Supplementary Model parameter identification) and used for the following simulations. Note that the layer-specific data of the mucosal layer was obtained by subtracting the measured passive forces of the muscular layer from the passive forces of the entire wall.

Table 5. Mechanical parameters for porcine SW tissue identified from active and passive experiments. Table reproduced with permission from Elsevier.

Mucosal Layer		
Parameter	Value	Unit
$c_{c,1}$	1.4	kPa
$c_{c,2}$	0.0149	-
$f_{c,1}/f_{c,1}^\dagger$	0.3767/0.6233	-
μ_e	0.0951	kPa
Muscular Layer		
Parameter	Value	Unit
$c_{s,1}$	0.2894	kPa
$c_{s,2}$	0.0188	-
$f_{s,1}/f_{s,1}^\dagger$	0.5788/0.4212	-
μ_{ECM}	0.1217	kPa
λ_{opt}	2.5403	-
ξ_s	0.8571	-
P_{opt}	24.5345	kPa
K_{vol}	121.6594	kPa

† Indices 1 and 2 correspond to the longitudinal and circumferential fascicle directions, respectively, as shown in **Figure 14a**.

Table 6. Material parameters for the calcium diffusion inside the SM tissue. Table reproduced with permission from Elsevier.

Parameter	Value	Unit	Reference
q_0	0.8	$\mu\text{M s}^{-1}$	As described in Chapter 3.5.3
ξ	9	mV	As described in Chapter 3.5.3
k	1	s^{-1}	As described in Chapter 3.5.3
$[\text{Ca}^{2+}]_{\text{rest}}$	0.15	μM	196
$f_{1,2,3,4,5,6,7,8,9}$	12/480/5/840/28/120/7.5/5/7.6	$\mu\text{M}^{-1} \text{s}^{-1}$	196
$r_{1,2,3,4,5,6,7,8,9}$	12/1200/135/45.4/0.0308/4/3.75/25/22.8	s^{-1}	196
$k_{3,4,7}$	15/5/10	s^{-1}	196
$k_{\text{cat}_K}/k_{\text{cat}_P}$	27/16	s^{-1}	196
k_{m_K}/k_{m_P}	10/15	μM	196
MLCP	7.5	μM	196

3.6.1 Geometrical model of the stomach

The modelling approach proposed in **Chapter 3.5** is applied to a geometry of the porcine stomach, see **Figure 19**. Note that the geometry of the stomach was generated by recording a real porcine stomach via an optical system consisting of 2 CCD cameras. Having the optical information of various angles at hand, these recordings were used to generate the three-dimensional geometry in a post-processing step. For more details, the interested reader is referred to ²⁴⁰, where a similar procedure was realized to reconstruct a skeletal muscle geometry. The surface was smoothed and an offset was created towards the inside of the stomach based on constant representative thicknesses. As indicated in **Chapter 3.5.3**, two layers, namely the mucosal layer ($T_{\text{MCL}} = 2.9$ mm, dark grey) and the muscular layer ($T_{\text{MSL}} = 4.6$ mm, light grey), are considered. Although the ECM is oriented in an isotropic way in both layers, the MSL is additionally dominated by an anisotropic arrangement of SMCs. Therefore, SMC fibers were assumed in a simplified manner to be aligned in the longitudinal and circumferential directions,

see also **Remark 2**. Due to the simple alignment of the fibers and the symmetric appearance of the stomach model, as a first approach only half of the stomach (**Figure 19**) was simulated and symmetric boundary conditions were applied. To mimic physiological boundary conditions, finite spring elements (stiffness: $k_{\text{spring}} = 10^{-2} \text{ mN/mm}$) were attached to the edges of the greater and lesser curvatures, representing the fixation via ligaments. In addition, the end surfaces of the esophageal entrance A_e and pyloric ending A_p were constrained in the normal direction to avoid unwanted rigid body motion. Finally, a pressure of $p = 0.13 \text{ kPa}$ acting perpendicular at the internal surface of the stomach simulates the filling process by chyme. For this purpose, the pressure increases linearly to a maximum value and is then kept constant over the time of simulation, cf. subfigure **Figure 19**.

3.6.2 Temporal evolutions of ϕ_{ICC} , ϕ_{SMC} , and $[\text{Ca}^{2+}]$

Before introducing all the fields involved in the electro-chemomechanical contraction excitation process, in a first step, the interactions between the membrane potentials ϕ_{ICC} and ϕ_{SMC} , as well as the intracellular calcium ion concentration $[\text{Ca}^{2+}]$ are considered by illustrating the temporal progresses of these fields for four different positions $P_{1/2/3/4}$ across an empty and a filled stomach. By considering these two filling states, the mechanical coupling effects can be demonstrated, see **Figure 20**.

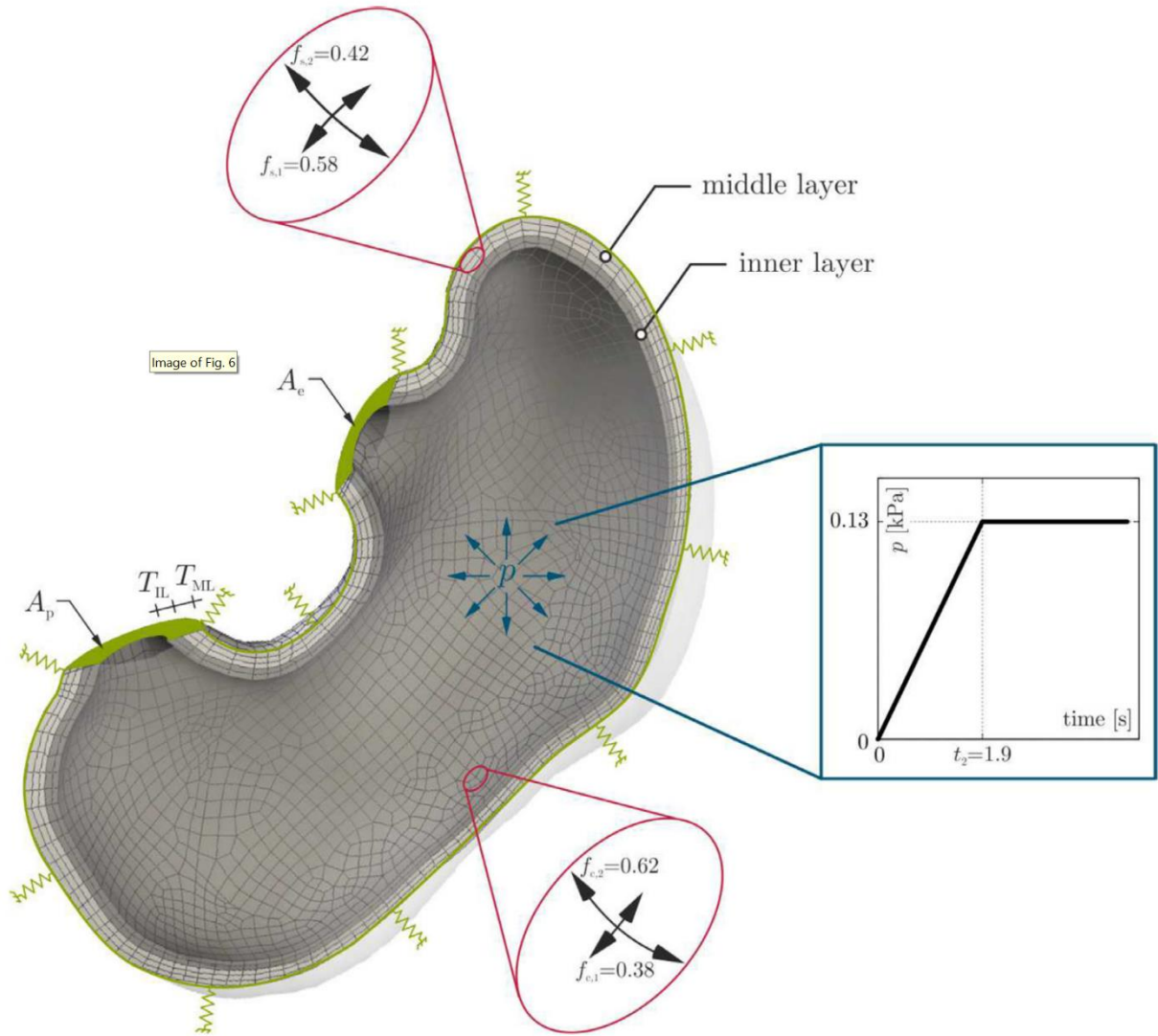


Figure 19. Illustration of a porcine, geometric stomach model. Two layers (MCL, MSL) were considered for the simulations. The MCL features passive, but anisotropic mechanical characteristics with collagen fiber fractions in longitudinal ($f_{c,1}$) and circumferential ($f_{c,2}$) directions. For the active anisotropic MSL, SMC fiber fractions in the longitudinal ($f_{s,1}$) and circumferential ($f_{s,2}$) directions were considered and are illustrated by double-sided arrows. Here, according to Eq. (5), ∂B_ϕ represents the greater and lesser curvature and the surfaces at the esophageal and pyloric ending, and ∂B_σ denotes the internal surface. For the discretization of the half system, 8140 linear brick elements (Q1P0) with 10,236 nodes were used. Figure reproduced with permission from Elsevier.

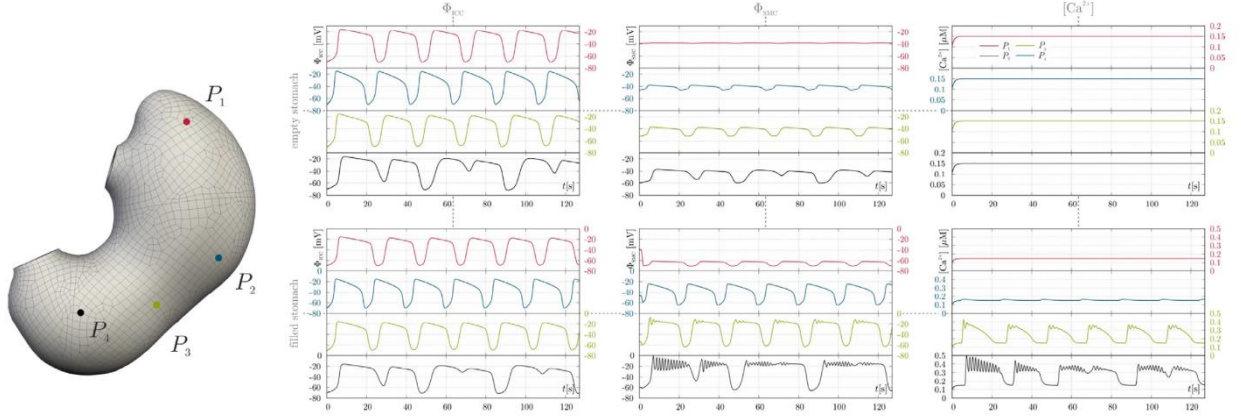


Figure 20. Temporal progress of ϕ_{ICC} , ϕ_{SMC} , and $[\text{Ca}^{2+}]$ at four different locations of the empty (upper row) and filled (lower row) stomach. (For interpretation of the references to color in this figure legend, the reader is referred to the web version of this article.) Figure reproduced with permission from Elsevier.

Focusing first on the empty stomach simulations (upper row), ϕ_{ICC} features a RMP of $\phi_{\text{ICC}}^r = -70$ mV and increases to a peak potential of -20 to -15 mV followed by a plateau-like decrease in all four locations. Almost six slow waves can be seen during a simulation time of 127 s. Clearly, the phase shift of the slow waves can be observed. ϕ_{ICC} increases first in the upper corpus (P_2) and then in the middle corpus (P_3) and lastly in the antrum (P_4), indicating a propagation of the slow waves in the aboral direction. This propagation is due to the decrease in the frequency with an increase in the distance from the dominant pacing site in the upper corpus. Point P_4 is worth noting. At the other points, six fully shaped slow waves with the same frequency can be seen. However, at point P_4 , the RMPs between some of the slow waves are elevated. Therefore, the slow waves are not fully formed.

Table 7. Material parameters for the electro-chemomechanical excitation. Table reproduced with permission from Elsevier.

Parameter	Value	Unit	Reference
κ	7	-	111
α	0.5	-	111
β	0.7	-	111

γ	8	-	111
ϵ_0	0.04-0.0025	-	111
Φ_{ICC}^p	-20	mV	111
Φ_{ICC}^r	-70	mV	111
$\Phi_{\text{ICC}0}^p$	-38.5	mV	105
$\Phi_{\text{ICC}0}^r$	-39 to -68	mV	105,241
d_{iso}	20-250	mm^2s^{-2}	chosen
$d_{\text{aniso},1}/d_{\text{aniso},2}$	20-250 / 1500	mm^2s^{-2}	chosen
w_f/w_a	0.03 / 80	mV	chosen
u_f/u_a	15 / 35	-	chosen
v_f/v_a	1.4 / 1.16	-	chosen

In a stable entrainment process, six well-formed slow waves should be visible at every point of the stomach. ϕ_{SMC} exhibits a constant electrical tone around -39 mV in P_1 , whereas the slow wave amplitudes at the other points increase in the aboral direction owing to the decreasing RMP, which varies from $\phi_{\text{SMC}}^r = -46$ mV in P_2 to $\phi_{\text{SMC}}^r = -60$ mV in P_4 . Because at each point the timing of the SMC slow waves coincides with the ones of the ICC, a phase-shift in the SMC network can be observed, indicating that SMC slow waves have the same propagation. The elevated RMP in point P_4 can also be observed for the SMC membrane potential. For further details on the electrical propagation, the reader is referred to Supplementary **Figure 2**, illustrating isochronic maps of the ICC and SMC membrane potential propagations across the SW. Focusing finally on the $[\text{Ca}^{2+}]$, the concentration is constantly at around $[\text{Ca}^{2+}]_{\text{rest}} = 0.15$ μM at every point. The calcium concentration at resting levels is too low to enable contraction of the SW.

In comparison, the lower row of **Figure 20** illustrates the temporal progress of the same variables for a filled stomach. Here, the ICC slow wave behavior is quite similar. The only difference is the frequency of the slow waves, which increases slightly in all four positions owing to the mechanical feedback when the stomach is inflated. In the empty stomach, at most six slow

waves can be detected in all four locations, while the beginning of the seventh slow wave can already be observed in the filled stomach at P_2 and P_3 . This also leads to an even more elevated RMP between the slow waves mentioned before, further reducing the characteristics of the individual slow wave. However, in comparison to the empty stomach, the temporal progress of ϕ_{SMC} is different when the stomach is internally pressurized. The electrical tone in the fundus decreases and becomes slightly phasic, oscillating from -71 to -61 mV. In P_2 (upper corpus), the RMP drops by nearly 20 mV and the peak potential increases by more than 10 mV, which all in all leads to an increase in the slow wave amplitude. This increase is even higher in the middle corpus, where the peak potential increases by more than 20 mV. The RMP drops by nearly 10 mV. Moreover, after the peak potential is reached at each slow wave, the potential decreases rapidly by about 8 mV, followed by a damped oscillation, and only then does the plateau-like decrease appear. At P_4 , in the antrum, various peak potentials reaching values between -15 and 0 mV can be observed superimposed on the PP of the slow waves. Here, the amplitude is the highest of all four points. The RMP decreases by nearly 5 mV at some time, but also increases at other times. Between the third and fourth and between the fifth and sixth slow wave, the RMP is nearly as high as the PP, making a distinction between the slow waves difficult. As in the empty stomach, the $[\text{Ca}^{2+}]$ at P_1 (fundus) stays at its resting value. In P_2 the calcium concentration only slightly increases to $0.16 \mu\text{M}$ in a phasic manner, not distinctly differing from that in the empty case. In the middle corpus, at P_3 , the calcium concentration increases at the same time the SMC potential increases from the resting calcium concentration to a peak concentration of $0.42 \mu\text{M}$ to $0.35 \mu\text{M}$, with slightly damped oscillations at the peaks. In the antrum, this increase is even higher with peak concentrations of 0.4 to $0.5 \mu\text{M}$. Here, the damping can be clearly observed at the times of the peak concentrations. The mechanical back-coupling effect of the stretch-dependent SMC plateau potential ϕ_{ICC}^p is the reason for the damped oscillation of ϕ_{SMC} and $[\text{Ca}^{2+}]$ at peak levels.

3.6.3 Influence of material characteristics on gastric muscle contraction

When investigating the deformation of the filled stomach from **Chapter 3.6.2**, nearly no contraction is visible in the simulation (not shown). However, relatively high stresses occur in the mucosal layer during loading, while nearly zero stresses are observed in the muscular layer. This

limits stomach inflation as the internal pressure increases. However, this in turn restricts possible stretches in the muscular layer and reduces mechanical feedback mechanisms. This situation is schematically illustrated in **Figure 21a**, in which the active and passive force-length relations of the muscular and mucosal layers are sketched, respectively.

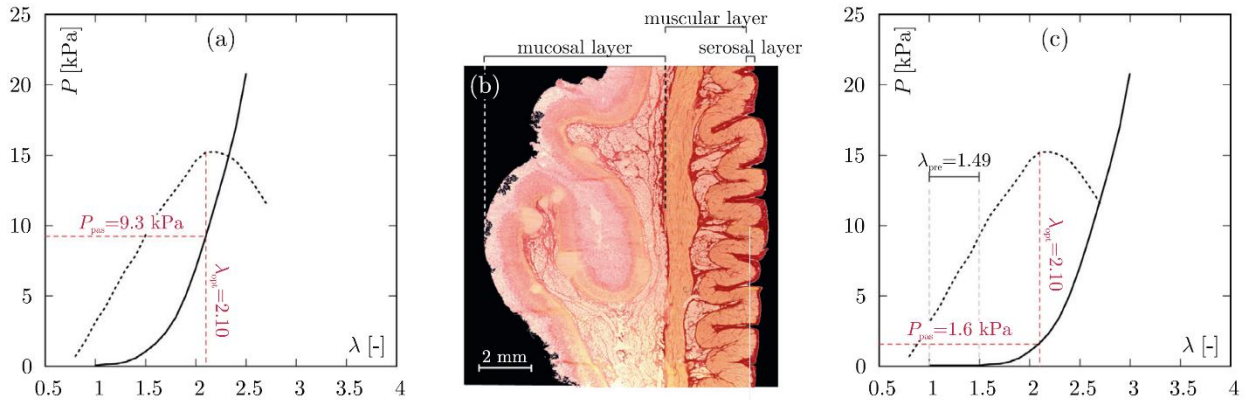


Figure 21. Influence of mucosal layer’s waviness on the SW mechanical behavior. The relations between the active behavior of the muscular layer and the passive characteristics of the mucosal layer (a) without and (c) with consideration of the unfolding of the mucosal waves are illustrated. (b) a histological cut stained with Picro-Sirius red staining featuring a strong waviness of the mucosal layer. Note that the passive characteristics of the mucosal layer and the active behavior of the muscular layer are illustrated as black solid and black dotted curves, respectively. (For interpretation of the references to color in this figure legend, the reader is referred to the web version of this article.) Figure reproduced with permission from Elsevier.

As shown in the figures, the stresses of the mucosal layer are relatively high in the range of the optimal stretch λ_{opt} , which limits the deformation of the stomach during the filling phase with simultaneous development of high voltages in the mucosal layer. Such behavior is unphysiological, as it is known that, in general, hollow organs experience relatively large deformations during the filling phase without occurrence of large stresses in their walls. This phenomenon is attributed to the organs’ microstructures.

The mucosal layer, featuring a strong waviness, is of particular importance with regard to load transfer mechanisms that take place during loading (**Figure 21b**). Following ¹⁶, during initial stretching of the SW, the mucosal layer does not contribute to load transfer, as during this stretching region called the ‘pre-stretch (λ_{pre})’, the folds are essentially smoothed without creating significant effort. With respect to (a), this means that the force- stretch relation of the mucosal layer needs to be shifted by λ_{pre} , see (c). For more details on this issue, the interested reader is

referred to ¹⁶. This phenomenon motivates the investigation of simulations with optimized parameters based on shifted experimental results. In the present study, only uniaxial investigations were made. In contrast, equibiaxial tension experiments on the mucosal layer were performed in ¹⁶, during which a mean pre-stretch of $\lambda_{\text{pre}}^{\text{biax}} = 1.26$ was realized. Based on this information, for the uniaxial data, a comparative pre-stretch of $\lambda_{\text{pre}}^{\text{uniax}} = 1.49$ has been determined. As a result, the stress-stretch relation of the non-shifted mucosal layer at optimal stretch λ_{opt} is 9.3 kPa, while in the shifted case, the passive contribution of the mucosa is 1.6 kPa. With this information, a new parameter set for the mucosal layer was determined (**Table 8**), allowing resimulation of the excitation-contraction of the entire stomach.

In **Figure 22**, the results are presented. In **Chapter 6.2**, only selective points were chosen to discuss the influence of the electrical and chemical fields. In this section, the spatio-temporal progress of the main variables ϕ_{ICC} , ϕ_{SMC} , $[\text{Ca}^{2+}]$, σ_{VM} (von Mises stress), and λ_{s} (smooth muscle fiber stretch) during active muscle contraction is illustrated at the discrete time points $t_{1/2/3/4/5/6} = 0/1.9/36.5/40.2/43.2/51.2$ s. To better visualize the contractions of the SW, the simulated deformation is scaled by a factor of 1.3.

In the deflated stomach at t_1 (left column), the ICC membrane potential ϕ_{ICC} is close to the resting membrane potential of -70 mV. Similarly, ϕ_{SMC} is at its resting level, gradually decreasing from about -38 mV in the fundus to -70 mV in the antrum. The same applies to the concentration of Ca^{2+} , which is approximately $[\text{Ca}^{2+}]_{\text{rest}} = 0.15$ μM . Therefore, no activation of contraction or stress can be detected, as indicated in the fourth row, which shows that σ_{VM} has a value of zero. The stomach is in a stretch free state, as indicated by a smooth muscle fiber stretch of $\lambda_{\text{s}} = 1$ in the muscular layer. During the filling phase between time step t_1 and t_2 , which is caused by the linear increase in the internal pressure, the stomach starts to inflate. At t_2 the maximum pressure is applied, and the simulated stomach inflates to a volume of nearly 1.89 liters, which is roughly 5.2-fold of the deflated stomach's capacity. Now, the stomach shows a visibly larger deformation with identical intragastric pressure, as the stresses in the mucosal layer increase much later in comparison to the simulation with the identified parameters of the unshifted experimental results from **Chapter 3.6.2** (not shown).

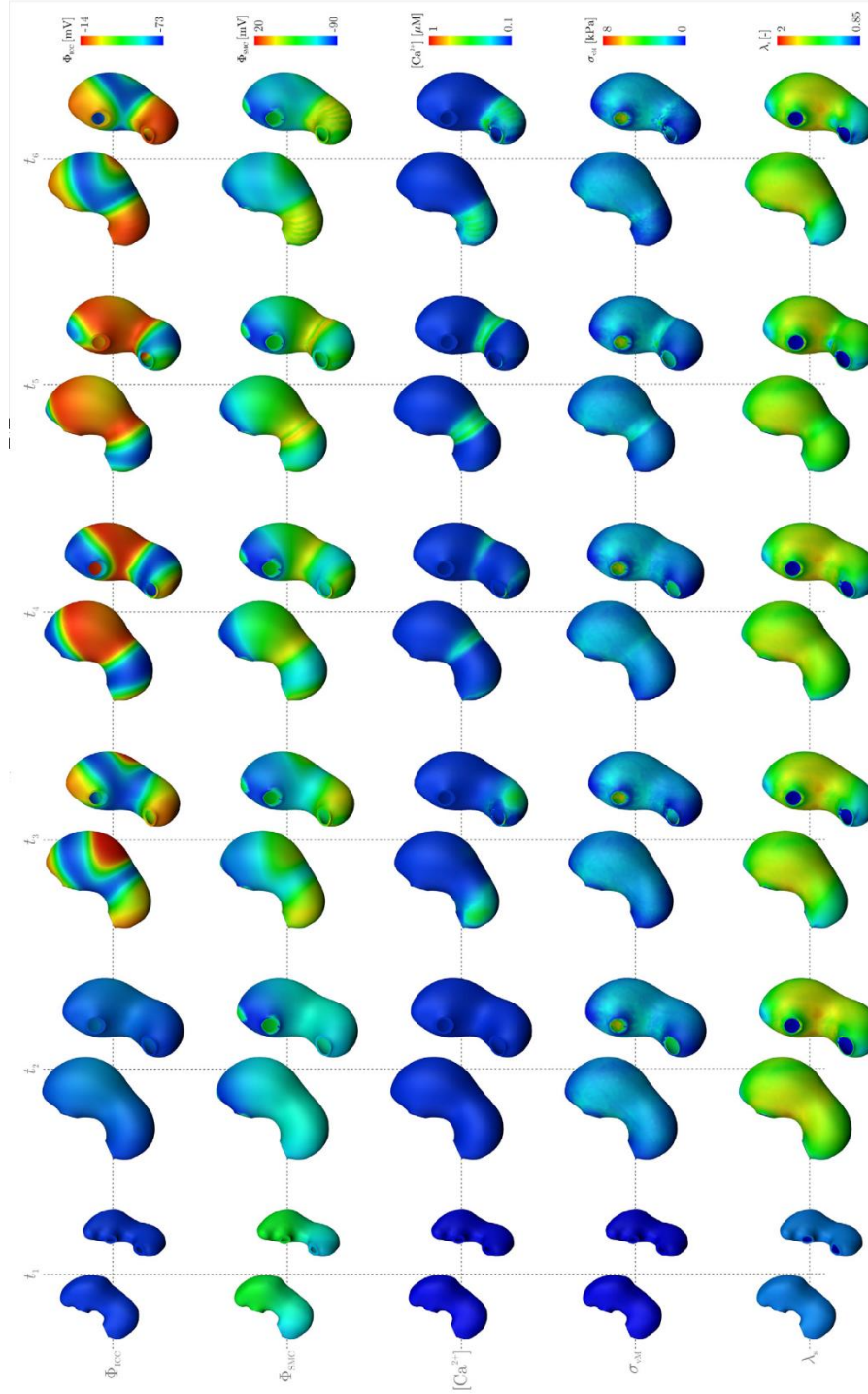


Figure 22. Re-simulation of the situation shown in **Figure 19**, considering the pre-stretch of the mucosal layer. Temporal progress of the main variables ϕ_{ICC} , ϕ_{SMC} , and $[Ca^{2+}]$, σ_{VM} , and λ_s during the active stomach contraction illustrated at the discrete time point $t_{1/2/3/4/5/6} = 0/1.9/36.5/40.2/43.2/51.2$ s. Every grid point illustrates snapshots of two stomach orientations. (For interpretation of the references to color in this figure legend, the reader is referred to the web version of this article.) Figure reproduced with permission from Elsevier.

As a consequence, the muscular layer becomes more stretched, and the mechanical stimulation leads to a decrease of the SMC resting membrane potential ϕ_{SMC}^r up to -80 mV in the fundus. In addition, the stress in the muscular layer increases to 3 kPa and is twice as much in the mucosal layer. The passive stretches in the muscular layer increase to at least 1.3 in the entire stomach wall, with the highest stretches of almost 100% occurring below the esophageal opening.

At time step t_3 , a new slow wave originates at the greater curvature of the upper corpus, as indicated by a rise in ϕ_{ICC} , while the previous slow wave can still be seen in the antrum and fundus. ϕ_{SMC} increases at the dominant pacing site and in the antrum as well, where it is in phase with ϕ_{ICC} , but does not change in the fundus. Because of the depolarization of the previous slow wave in the antrum, Ca^{2+} increases to $0.5 \mu M$, but no increase in σ_{VM} can be seen. A contraction of the SW in the antrum due to the depolarization of the vanishing slow wave is clearly visible, accompanied by lower muscle stretches in the distal antrum. At time step t_4 , the previous ICC slow wave moves slowly further in the aboral direction and the new slow wave is fully propagated in the circumferential direction, leading to a ring of depolarization of ϕ_{SMC} in the corpus, which in turn increases $[Ca^{2+}]$ in this region, as well as σ_{VM} . As a consequence, the SW slightly begins to contract. In contrast, ϕ_{SMC} remains low in the fundus. During t_4 , the depolarization of ϕ_{ICC} propagates further to the fundus and antrum, while the ring of depolarization of ϕ_{SMC} moves only in the aboral direction, while increasing the amplitude. In fact, the SW depolarizes to $\phi_{SMC} = \phi_{SMC}^p = 10$ mV. Two regions of depolarization can be distinguished due to the several peak potentials at the PP of the slow wave. $[Ca^{2+}]$ also increases up to $0.5 \mu M$ while propagating with the SMC slow wave. σ_{VM} increases to 4 kPa in the region of high $[Ca^{2+}]$, and a ring of contraction can be observed in the lower corpus, constricting the inflated stomach while moving in the aboral direction. As a consequence, λ_s decreases slightly. In the last time step t_6 , the ICC and SMC slow wave reaches the antrum. The SMC membrane potential exhibits several peaks in the antrum owing to the mechanical back-coupling effect, while the depolarization moves towards the pylorus. This leads to an area of increased $[Ca^{2+}]$ in the antrum and a contraction in this region. However, σ_{VM} increases less than in t_5 . The wide ring of calcium increase in the antrum is caused by the several peaks superimposed on the plateau of the calcium increase. These peaks are weakened in value and consequently, the stress is lower than in t_5 , showing that the stress development is very

sensitive towards changes in the calcium increase. This also fits with the SMC membrane potential, which seems to be more depolarized in t_5 than t_6 . The peaks become greater in number with an increase in the SMC membrane potential. The smooth muscle fiber stretch λ_s in the antrum decreases as the stomach contracts, partly resulting in a state of compression. The SW of the fundus is electrically silent during the simulation and is in a relaxed state.

Table 8. Mechanical parameters identified from the shifted, experimental data of the mucosal layer. Table reproduced with permission from Elsevier.

Mucosal Layer		
Parameter	Value	Unit
c_{c1}	0.5335	kPa
c_{c2}	0.0123	-
f_{c1}/f_{c2}	0.3781/0.6219	-
μ_e	0.0903	kPa

3.7 Discussion

Motivated by the need for a better understanding of the mechano-electrochemical process during active smooth muscle contraction of the SW, a three-dimensional multi-field model of the excitation-contraction characteristics in gastric smooth muscle tissue is presented. To identify the model parameters describing the material behavior of the SW's muscular and mucosal layers, active and passive experiments on gastric tissue strips were conducted. Within the finite element method, whole-organ simulations on a three-dimensional numerical model of a porcine stomach were performed to predict the spatio-temporal propagation of the ICC and SMC membrane potential (electrical fields), the intra-cellular calcium concentration (chemical field), and the generation of active contraction (mechanical field).

3.7.1 Modeling the electro-chemomechanical contraction excitation process in the stomach wall

Gastric electrical oscillations, termed slow waves, are always present in the SW, but do not always trigger a contraction. Contractions can only occur at the peak of a slow wave in the presence of mechanical or neural stimuli, which is why the slow waves only determine the maximum achievable rate of phasic contractions. Therefore, in the first simulation, the electro-chemomechanical characteristics of the empty, deflated stomach were investigated. To this end, no loading of the SW was conducted, and the only input signal were the electrical slow waves of the ICC. The results in **Figure 20** demonstrate a dominant frequency of the ICC slow waves of approximately 3 cpm, indicating successful entrainment of the ICC slow waves replicated by our model. However, the elevated RMPs between some slow waves in the antrum are an indicator of an unstable entrainment process, see also **Chapter 3.7.4**.

The second simulation aimed to study the mechano-electrochemical contraction process. Herein, the stomach was inflated by an internal pressure, acting perpendicular on the inner surface of the SW, to imitate the filling by a bolus of food. The capacity of the filled stomach amounts to nearly 2 liters at an intragastric pressure of 1.3 kPa. Physiological observations report a maximum volume of 2 to 4 liters. Generally, the normal intragastric pressure of the resting stomach is below 1 kPa, and can increase up to 4 kPa when distended ²⁴². After inflation, the input signal of ϕ_{ICC} and ϕ_{SMC} was modulated by the mechanosensitive response of the slow waves. As can be seen from the results, the frequency of the ICC slow waves increases because of the mechanical stimulation, which has also been observed experimentally by Won et al. ²²². In the model, particularly, a mixing rule was applied to simulate the heterogenous response behavior of the SMC slow waves to mechanical input. The results demonstrate a mechanically induced decrease in the electrical tone in the fundus, especially around the esophagus. The associated relaxation, experimentally observed and described in ^{155,159,213,243} is not visible in either of the simulations, because the preceding tonic contraction of the fundus at rest was not visible either. To improve this, by setting the threshold for contraction in the fundus to be more negative than in the antrum, following the observations by ²⁴⁴, we expect the tonic contraction and mechanically induced relaxation to be more visible. The results in the antrum are in good agreement with those of ²⁴⁴, who measured a rise in the amplitude of the canine antral slow wave after nerve stimulation.

Furthermore, according to this study and to ¹⁹⁷, the characteristic peak potential and subsequent PP of the slow waves are well replicated by our model. Won et al. ²²² revealed that the PP increases when murine antral muscle is mechanically stimulated, which is in accordance with our results. The authors also found an increase in the RMP under mechanical loading, which was not considered within the present modelling approach. The SW in the simulation with the shifted experimental results for the mucosal layer (**Chapter 3.6.3**) clearly showed active contractions during each slow wave owing to the mechanosensitivity. The constrictions of the SW move in an aboral direction, cf. **Figure 22**, which has also been reported experimentally by Cannon ²¹⁴ and Gregersen et al. ¹⁶². In the corpus, a tonic-phasic combination exhibiting phasic electrical behavior at an elevated baseline can be observed in the simulations, which was also reported by Golenhofen and Mandrek ²⁴⁵. Further, the damped oscillation due to the coupling and back coupling effect has also been observed in smooth muscle tissue ²⁴⁶. The calcium concentration during slow wave depolarization reaches peak values of about 0.5 μM , which is slightly higher than the experimentally observed concentrations ^{238,247}. In addition, the shape of the calcium concentration in the distal stomach under loading (two lower rows in **Figure 20**) matches quite well the experimentally observed calcium concentration obtained under stimulation of ACh by Ozaki et al. ²⁴⁸.

3.7.2 Stomach mechanical properties

To develop a comprehensive modeling approach which is able to describe the excitation contractile behavior of the stomach, active and passive experiments are essential. Within this study, both types of experiments were performed. To fully characterize the mechanical SW characteristics, biaxial protocols, like gastro-dynamic inflation experiments on whole stomachs ^{54,151,158,160–165,185}, or tensile loading experiments on tissue strips ^{16,93}, are needed. However, the experimental aim of the present study was not a full characterization of the mechanical SW behavior; rather, we focused on uniaxial experiments ^{94–96,166}, identifying meaningful material parameters for a multifield modeling approach as presented in **Chapter 3.5**.

Within this study, uniaxial passive experiments in the longitudinal and circumferential stomach directions were performed using complete SW strips and those consisting of the muscular layer only. Based on the assumption that the contributions of the serosal layer to the load transfer and physiological deformation are negligible, the testing of the muscular layer strips and complete SW strips allows for the determination of the mucosal layer mechanical characteristics. This implies that identification of the respective material parameters is required for the presented modeling approach. Following **Figure 18**, all strip types display typical exponential stress-stretch characteristics, which is consistent with studies available in the literature ⁹⁴⁻⁹⁶. Owing to the different strip structures, the stress-stretch relationships of the complete tissue wall strips indicate a higher stiffness than those of the separated muscle layer strips. When focusing on the different loading directions of the entire SW, cf. **Figure 18a** and **b**, it is worth noting that the tissue is slightly stiffer in the longitudinal direction than in the circumferential direction. This behavior can be also observed in experimental studies by Zhao et al. ^{95,96} and Jia et al. ⁹⁴, even though partially different species and stomach regions were considered in those studies. Furthermore, when considering the muscular layer, based on the stress-strain relation, it is slightly stiffer in the longitudinal direction than in the transverse direction, cf. **Figure 18c** and **d**. However, for the mucosal layer, the circumferential direction is stiffer than that in the longitudinal direction (Supplementary **Figure 4a** and **b**). While our findings for the muscle layer are similar to those in the literature ⁹⁴, the results of the mucosal layer in this study show a relationship that is the inverse to that in the literature ⁹⁴. However, while ⁹⁴ measured the mechanical characteristics of the mucosal layer directly, in the present study, the stress-stretch relation of the mucosal layer was analyzed by subtracting the muscular layers' behavior from the behavior of the entire SW.

The determination of the mucosal layers' mechanical characteristics is challenging, as the layer has a wavy structure in its *in-vivo* state, which is frequently not considered in experimental studies. However, in our own experimental (biaxial tension) investigations on porcine stomach ¹⁶, the mucosal layer was found to behave strongly isotropically. Further, owing to its wavy structure, a so-called 'pre-stretch' of approximately $\lambda_{\text{pre}} = 1.3$ was found, where the mucosal layer does not bear loads, i.e., the stress is equal to zero in this region. The underlying mechanism behind this is based on the fact that the undeformed mucosal layer of the entire strip has a high waviness (**Figure**

14b). If the strip is, for example, pulled axially, the folds are continuously pulled smoothly without force being applied to the mucosal layer. Once the mucosal layer is smooth, it can transfer loads. For detailed investigations on this topic, the interested reader is referred to ¹⁶.

In case the aforementioned phenomenon is not taken into account (Supplementary **Figures 4a** and **b**), there is a stronger superposition between the active and passive stress stretching curve of the muscle or mucosa layer (**Figure 21a**). Consequently, if material parameters are identified from this and simulations are carried out, these show too little deformation behavior during activation (see **Chapter 3.6.3**). Therefore, simulations with a pre-stretch of the mucosal layer were carried out within the present study. As expected, an increase in the pre-stretch led to an increase in the deformation during contraction or the filling phase because the mucosal layer contributes to the load transfer of the entire SW at higher global loadings. These numerical studies in combination with the findings in ¹⁶ confirm the correctness of the presence of a preload.

The stomach smooth muscle tissue shows an active stress-stretch relationship characterized by an ascending limb, a stress maximum and a descending limb, as shown in **Figure 17**. The mean maximum stress (P_{\max}) determined in the longitudinal (15.32 kPa) and circumferential (10.44 kPa) directions differ considerably. These values are about half as much when compared to stomach tissue of small mammals such as guinea pigs ¹³⁷; however, they are about three times higher compared to active muscle stress values of porcine bladder tissue ^{75,76,249}. The maximum isometric force is reached after large elongations of the muscle strip, corresponding to an optimum stretch of $\lambda_{\text{opt}} = 2.1$ to 2.6 (**Figure 17**). Similar values for optimal muscle lengths were reported for porcine stomach strips and strips of porcine bladder tissue ^{44,75,76,125,228}.

Both the active and passive mechanical properties are related to each other in a certain way (**Figure 21a**). It has been shown that the structural properties of the SW, in particular the waviness of the mucosal layer, have a physiologically significant influence on the load transfer mechanisms of the SW. Because of this waviness, the stomach can accommodate a large volume while the tensile stresses remain low in the mucosal layer. The folds are pulled out until they are no longer present. This stretching without any stress build up was defined as a pre-stretch. Thereafter, the mucosal layer can transfer the tension to the SW. For the modelling of the individual layers this means that such a behavior has to be considered. One possibility is to shift the stress-stretch

relation of the mucosal layer accordingly by λ_{pre} (**Figure 21c**). The simulative results with the shifted data show a much more physiological result compared to the simulations with the non-shifted information. Thus, the stomach can accommodate significantly higher volumes while at the same time minimizing tension loads inside the mucosal layer.

3.7.3 Functional aspects on relation to mechanical findings

The stomach exhibits a complex structure to deal with a series of functions including storage and mechanical churning of ingested food. Some of the main challenges, from a physiological/biomechanical point of view, are dealing (at the same time) with large volume changes induced by intake of food and enabling active muscle contractions to transport and mix the ingested food with the chyme. One prerequisite is the large working range of the muscular layer (**Figure 17**), which enables the generation of active forces despite large stomach volume changes of up to 300%²⁵⁰. Compared to skeletal muscles, which are able to shorten by about 40–50% from their optimum muscle length²⁵¹, smooth muscle can shorten about twice this distance (**Figure 17**)^{44,75,228}. Furthermore, in addition to the vagovagal reflex, which leads to relaxation of the stomach in response to the swallowing of food²⁵², we found that the structure of the mucosal layer further contributes to accommodation of large amounts of food in the stomach. Owing to the wavy-structure of the mucosa (**Figure 21b**), initial stomach filling results in almost no stress in this layer. Significant passive forces which counteract further stomach filling were generated only at stretches of $\lambda > 2.0$ (**Figure 21c**). Thus, interaction of the SW microstructure (including region and layer-specific collagen and muscle fiber bundle orientation as well as (wavy) arrangement of the layers,¹⁶) and excitation propagation, cf. **Chapter 3.6.3**, ensures complex stomach functions.

3.7.4 Model limitations and outlook

This section aims to discuss some limitations of the presented model. One critical factor is the comprehensive number of material parameters. The procedure for the material parameter identification, see Supplementary Model parameter identification, is layer-specific and handles the active and inactive states separated from each other. Therefore, a reduction of variables during the optimization processes provides parameters, which may represent the specific material layer and

the respective state, but not the overall mechanical response of the physiological condition of the combined layers. Further, the algorithm for the parameter identification is a direct search method, which does not use numerical or analytic gradients. As for many other optimization techniques, the solution can converge to a local minimum of the objective function. Consequently, it is not possible to verify whether the obtained set of parameters represent the solution for the global minimum of the objective function.

One limitation of the model are the applied boundary conditions. The choice of a symmetric stomach model restricts the natural deformations obtained by the active contractions of the stomach wall. Similarly, because there was no information at hand, the chosen spring stiffness at the greater and lesser curvature are not correlated to any physiological value. Furthermore, as can be seen in ¹⁶, the fiber orientation in the SW is much more complex, with isotropic behavior in some regions and anisotropic alignment of fibers in others. This has a large impact in the characteristics of active contractions. In addition, by choosing constant layer thicknesses along the stomach wall, and not different thicknesses as it is the case in the real stomach ⁹⁵, the simulative contraction force may be restricted. It is known that the antrum features a thicker muscular wall, resulting in the strong phasic contractions. A further limitation is the phenomenological approach of the electrical ICC and SMC model by FitzHugh-Nagumo. This includes the simplified coupling between ICC and SMC membrane potential by simple scaling, as well as the observed unstable entrainment process mentioned earlier. To improve this, ¹⁰⁵ and ²⁵³ suggest a voltage-to-calcium transducer mechanism for the entrainment, instead of a simple voltage-based coupling between ICCs and SMCs as used here. In their biophysical-based model, the underlying concepts of ion flux through the relevant channels in the ICC and SMC are considered, enhancing the model's predictability. This enables the implementation of many of the complex mechanisms during the electro-chemomechanical coupling process, which are not covered by the current approach presented in **Chapter 3.2.3**. For example, cell stretch can induce an increase in calcium concentration directly, and not only by depolarizing the cell ³⁸. Thus, $[Ca^{2+}]$ can also be coupled to the mechanical field ϕ . Further, in many studies it is stated that the ICC frequency is determined by intracellular cycling of Ca^{2+} , which was implemented by Corrias and Buist ¹⁹³. In this context, the mechanical feedback of the ICC and SMC electrophysiology can be implemented by

considering stretch activated channels. The mechanical feedback and location-dependencies in our model are not correlated to an underlying cause, but replicate the physiological observations by implementing a tonic-to-phasic switch along the stomach wall ²⁴⁵.

Finally, the stomach shows viscoelastic and history-dependent characteristics, which was not considered in the present modeling approach, leading to further limitations of the model predictability. Finally, the model needs to be validated in future. While in the present study the model parameters were identified at tissue sample scale, a model validation should be conducted at organ level. To this end, a step-wise procedure is promising, including a validation of the passive and the total (passive and active) characteristics. For the experimental characterization of passive stomach properties, typically *in-vivo* [e.g. ^{54,187}] or *ex-vivo* ^{151,161,254} inflation tests are performed. Thereby, the stomach is inflated with a physiological solution, partly included in a plastic bag (barostat procedure), while simultaneously measuring the internal pressure and the volume. During a validation process, these two quantities can be used to compare them with the model response. In a second step, the model previously validated on passive organ experiments can thus be validated on organ experiments that include the total (passive and active) material response ^{158,165,185}, including, e.g., internal pressure, volume, and surface deformation data.

The present model is able to replicate several typical features of gastric smooth muscle excitation-contraction coupling occurring in the two functional units of the stomach, which are the gastric reservoir and the antral pump, as described in **Chapter 3.2.2**. The model is supposed to represent a first step in the prediction of gastric smooth muscle contraction in health and disease. By altering the parameters of the electrical field, different scenarios associated, for example, with gastroparesis can be investigated in future. This includes abnormalities in slow wave frequency (tachygastria and bradygastria), initiation, or conduction, caused by clinical surgery or a degraded ICC-network ^{225,253,255,256}. To enhance the predictability of the model with regard to the aforementioned gastric impairments, the properties of the electrical field as the input signal in the present model need to be optimized. This includes a stable entrainment process, as well as an improvement of the region- and stretch-dependent mechanical characteristics of the electrical slow waves.

Declaration of Competing Interest

The authors declare that they have no known competing financial interests or personal relationships that could have appeared to influence the work reported in this paper.

Acknowledgements

Partial support for this research was provided by the Deutsche Forschungsgemeinschaft (DFG) under Grants BO 3091/18-1 and SI 841/12-1.

Supplementary material

Supplementary material associated with this article can be found, in the online version, at doi: [10.1016/j.actbio.2020.04.007](https://doi.org/10.1016/j.actbio.2020.04.007).

4 Influence of layer separation on the determination of stomach smooth muscle properties

4.1 Introduction

There are three types of muscles: skeletal, cardiac, and smooth muscles. The latter are predominantly located in the walls of blood vessels and organs of the gastrointestinal, urogenital, and respiratory tract. Smooth muscles are non-striated and cannot be controlled voluntarily. Through complex coordination between contraction and relaxation, they facilitate the propulsion of various contents within the body and regulate the inner pressure of organs. Due to their distinct features and crucial role in the healthy functioning of various vital body systems, research on smooth muscles has been of high physiological and medical interest ^{9,10}.

Typically, walls of hollow organs consist (from inside to outside) of a mucosal, muscular and serosal layer. A decisive aspect of the study of smooth muscles are active biomechanical properties, including the characteristic force-length relationship (FLR) ⁴¹ and the hyperbolic force-velocity relationship (FVR) ⁴⁹. Their examination yields experimental data, which are necessary for the development of muscle models ²⁵⁷ and realistic three-dimensional models of organs ^{75,258}. These, in turn, can describe the organ in health and disease and advance the knowledge and treatment of various medical conditions.

Active biomechanical properties of muscles are commonly examined through *in vitro* uniaxial tensile experiments ^{69,144}, in which muscle forces are measured in one direction only. Typically, muscle tissue is mounted along the muscle direction to a force-measuring device, while muscle activation is initiated through electrical or pharmacological stimulation. Thereby, biomechanical properties of smooth muscles in uniaxial experiments have been examined on tissue specimens, dissected from the bladder ^{72,73,75,76,85–87,89,90,125,138,145,146,228,259}, the stomach ^{14,44,143,258}, the intestine ^{11,136,141,260–263}, the trachea ^{13,139,142,264,265}, or from blood vessels ^{140,266–270}.

However, the walls of the urinal- and gastrointestinal organs contain multiple smooth muscle layers with different muscle fiber orientations ^{12,16,271}. While various studies conducted tests on isolated muscle layers ^{85,265,272}, muscle bundles ^{73,87,138,146}, or single smooth muscle cells ¹⁴, active

biomechanical properties are frequently investigated of strips from which the muscle layers are not separated^{44,76,125,141,143,228}. In such experiments, narrow strips are cut and mounted so that the examined muscle layer and specifically their muscle fibers are aligned lengthwise to the force-measuring axis of the measuring device. In contrast, the other muscle layers (with deviating muscle fiber directions) are still attached. Therefore, strip activations initiate muscle contractions in more directions than just in the lengthwise axis of the strip. Since the strips are not fixed transversally, this would cause a shortening in that direction. Although generally neglected, a transverse shortening may have a considerable effect on examining biomechanical properties through uniaxial experiments. To date, there has not been a systematic study that investigated the influence of layer separation on the determined muscle properties.

The aim of this study is to examine the influence of muscle layer separation on the determined muscle properties. Therefore, we investigated the active biomechanical properties of smooth muscle strips, consisting of the whole muscle tissue and muscle strips, consisting of only one separated muscle layer. Strips were dissected from the ventral fundus of the pig stomach, as this region exhibits two orthogonally oriented, distinct muscle layers^{16,44}. Uniaxial experiments were conducted to investigate muscle properties, including the FLR and FVR.

4.2 Materials and methods

4.2.1 Experimental set-up

Porcine stomachs of healthy domestic pigs (*Sus scrofa domestica*, age: \approx 6 months, mass: \approx 100 kg) were obtained from a slaughterhouse immediately after animal sacrifice. After the death of the animal, stomachs were prepared within 90 minutes. The experiments were conducted on overall nineteen (n=19) gastric smooth muscle strips cut from 12 healthy pig stomachs. The experimental setup, handling, and preparation of gastric smooth muscle tissue have been described earlier in detail^{44,258}. An aerated (95% O₂ and 5% CO₂) Krebs solution (124mM NaCl; 5mM KCl; 2.5mM CaCl₂; 15mM NaHCO₃; 1.2mM KH₂PO₄, 1.2mM MgSO₄, 10mM C₆H₁₂O₆; pH 7.3 at 37°C) was used for storage of the tissue and realisation of the experiments at temperatures of 4°C and 37°C, respectively. To eliminate spontaneous contractions, the method of adding 50 μ M methylene blue

to the solution plus illumination was used during experiments^{273–275}. Smooth muscle tissue strips (0.26 ± 0.11 g) of 15×7 mm were dissected from the ventral fundus in the circumferential direction (i.e., transversal to the direction of the gastric serosal folds and orthogonal to the greater curvature, see **Figure 1a**). Experiments were performed on strips, from which only the mucosal layer was removed (whole-muscle strips, WMS) and strips, from which the mucosal and the longitudinal muscle layer were removed, leaving only the circumferential smooth muscle layer (separated layer strips, SLS).

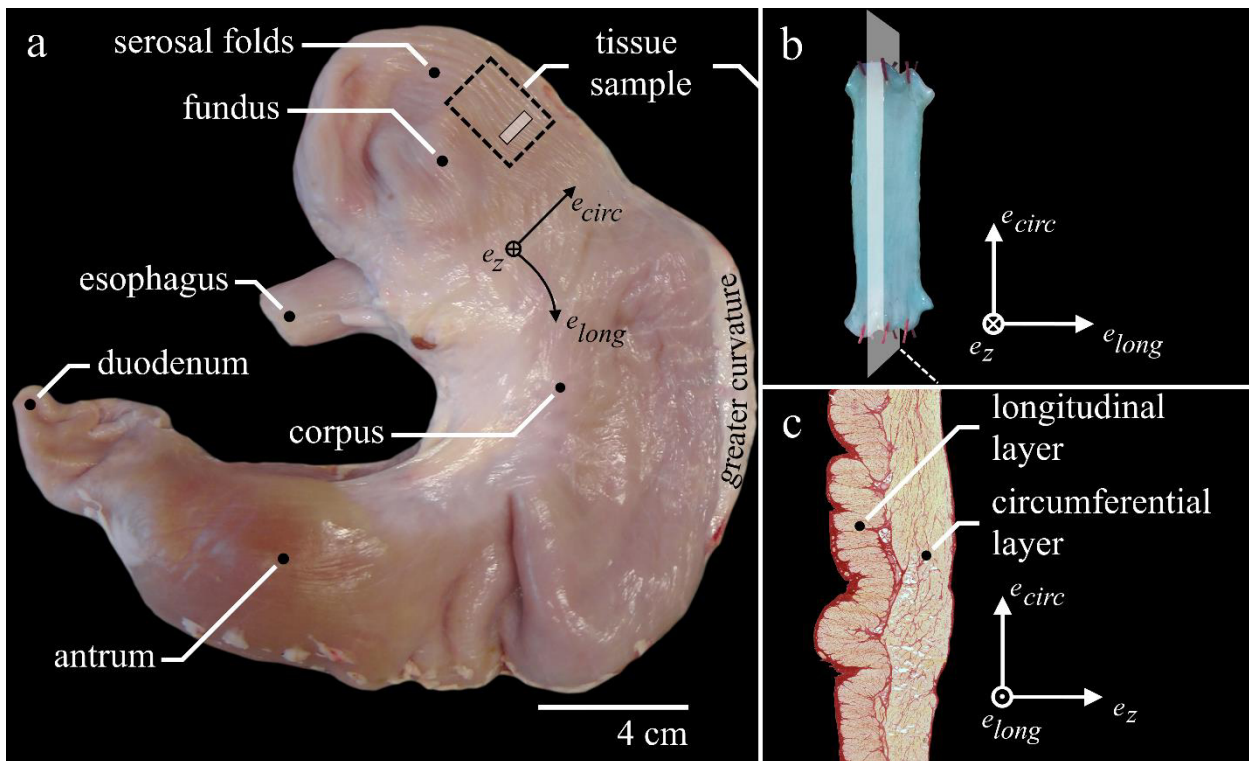


Figure 23. Tissue strip structure and location in the porcine stomach. (a) Ventral view of a porcine stomach with anatomical regions. The dashed black rectangle indicates the location from which tissue strips were dissected. The visible gastric serosal folds run in line with the greater curvature. (b) Tissue strip, mounted in the uniaxial tensile experiments. Note, the blue color of the strip was due to the addition of methylene blue to the solution. The transparent white plane illustrates the (c) lengthwise histological cut of a porcine muscle tissue strip from the fundus. The mucosal layer is missing, as it was cut away for the experiments. The thin serosal layer on the outside (left), the outer longitudinal- and the inner circumferential muscle layer can be identified. Permission to reproduce figure under the terms of the CC-BY license.

Both ends of the strip were threaded into small rectangular blocks (10 x 8 x 3mm) with a braided fishing line. Via these blocks, the strip was mounted vertically to a dual-mode muscle lever system (Aurora Scientific 305C-LR; accuracy: ± 1 mN in force; ± 1 μ m in length), to be part of the Aurora Scientific 805A in-vitro muscle apparatus. The circumferential layer was aligned along the force-measuring axis e_{circ} (**Figure 23b, c**). After strips were suspended in a relaxed state at a very short length (clearly sagging), they were passively stretched via an isokinetic ramp (5 mm/min) until a passive force of 1–3 mN was reached. After reaching the end of the ramp, the strips were kept at this length, while the passive force development settled to a negligible initial value (<1 mN). The length of the strips, averaging 10.8 ± 1.3 mm between attachment threads, was determined with a digital sliding caliper (± 0.02 mm accuracy) and was defined as slack length (L_S). Muscle contractions were induced by supramaximal electrical stimulations (1000 mA, 100 Hz, 5 ms) for 16 s. The muscle properties were determined after an equilibration period of 30 min^{44,228,258}.

4.2.2 Determination of muscle properties

Uniaxial experiments were performed *in vitro* on nineteen ($n = 19$) tissue strips. **Table 9** summarizes the number of samples examined for each analyzed parameter. The FLR was investigated by a series of isometric contractions with length increments of 20% L_S until a decrease in force, and hence the descending limb of the FLR, was established. The muscle length at maximum isometric force (F_{im}) was defined as the optimum muscle length (L_0). The ascending- and descending limbs of the FLR were fitted using linear regression models ($f(x) = mx + b$, with $x = L/L_S$) to extrapolate to lengths of zero force generation^{140,267}. The respective distances to L_0 were defined as the width of the ascending- (w_{asc}) and descending limb (w_{desc}).

Before determining the FVR, the strips were stimulated isometrically every 5 min until a stable maximal isometric force generation (deviation $<3\%$ F_{im}) was established. A series of 6 isotonic contractions determined the FVR at L_0 against forces of 0.1–0.9 F_{im} . The data were fitted with Hill's hyperbolic equation to yield the maximum shortening velocity (v_{max}) and the curvature factor $curv = a/F_{im}$ (a describes the force asymptote). Between all contractions, recovery phases of 5 min were interposed, and the "cycling-protocol" by Brenner¹²⁷ was applied.

The cross-sectional area (CSA) of the strip at L_0 was determined from the strip volume and the length of the tissue between the stitches. The volume was calculated by its wet weight, assuming a density of 1.05 g/cm^3 ²⁶⁶. F_{im} and the passive isometric force were divided by the strip's CSA to calculate the maximum active stress (p_{act}) and the corresponding passive stress at L_0 (p_{pass}), respectively.

Table 9. The number of investigated tissue samples of each strip group for the determined muscle properties and parameters. FLR parameters: L_0 , w_{asc} , w_{desc} , p_{act} and p_{pass} . FVR parameters: v_{max} and $curv$. Permission to reproduce table under the terms of the CC-BY license.

Stomach Number	Whole-Muscle Strips		Separated Layer Strips	
	FLR	FVR	FLR	FVR
1	X		X	X
2			X	X
3	X	X	X	
4	X		X	X
5	X	X		
6	X	X	X	X
7	X	X	X	X
8	X		X	
9			X	X
10	X	X		
11	X	X	X	X
12	X	X		
Number of Samples	10	7	9	7

4.2.3 Histological observations

Histological analyses were performed exemplarily for one WMS strip to show typical stomach smooth muscle structure. Cross-sectional, lengthwise-sectional, and in-plane slices were stained with Picrosirius Red staining protocol ¹², exhibiting two distinct muscle layers. The outer muscle layer contains muscle fibers, oriented in the longitudinal direction, whereas the inner muscle layer consists of muscle fibers in the circumferential direction. The procedure is described in detail in previous studies ^{16,44,76}.

4.2.4 Statistics

For statistical analyses, muscle properties were normalized as follows: (1) Force and length values were divided by individual CSA and L_0 , respectively. (2) Velocity data were normalized to optimal muscle length and expressed in L_0/s . The strips were differentiated according to their composition (WMS vs. SLS). The biomechanical properties were analyzed using seven parameters (L_0 , w_{asc} , w_{desc} , p_{act} , p_{pass} , v_{max} , and $curv$). No indication for deviation from normal distribution was found using the Kolmogorov–Smirnov Test with $p > 0.05$. Each parameter was tested for significant differences using Student's unpaired t-test. A significance level of $p < 0.05$ was used for all analyses. Statistical analyses were carried out using MATLAB (The Mathworks, Inc., Natick, MA, USA).

4.3 Results

The FLR and FVR of whole-muscle strips and separated layer strips are shown in **Figure 24**. The shape of the mean active isometric FLR was similar for both groups investigated (**Figure 24a**). Specifically, the FLR exhibited a linear ascending limb, a bell-shaped plateau region, and a linear descending limb. No differences have been found for optimum muscle length (WMS: $L_0 = 2.86 \pm 0.23 L/L_S$, SLS: $L_0 = 2.98 \pm 0.43 L/L_S$). Furthermore, there were no differences in w_{asc} and w_{desc} between both groups of strips (**Table 6**). However, p_{act} was significantly lower for WMS (58.5 ± 11.5 kPa) compared to SLS (160.9 ± 66.5 kPa) (**Figure 25a**).

Table 10. Influence of layer separation on optimal length (L_0), the width of ascending (w_{asc}), and descending limb (w_{desc}) of the force-length relationship and passive stress (p_{pass}) at L_0 . (n.s.): not significant. Permission to reproduce table under the terms of the CC-BY license.

Sample	$L_0 [L/L_S]$	$w_{asc} [L/L_0]$	$w_{desc} [L/L_0]$	$p_{pass} [\text{kPa}]$
Whole-Muscle Strips	2.86 ± 2.32	0.67 ± 0.07	1.29 ± 0.98	20.6 ± 13.6
Separated Layer Strips	2.97 ± 4.29	0.63 ± 0.05	0.87 ± 0.58	20.3 ± 8.2
p	0.461 (n.s.)	0.203 (n.s.)	0.273 (n.s.)	0.944 (n.s.)

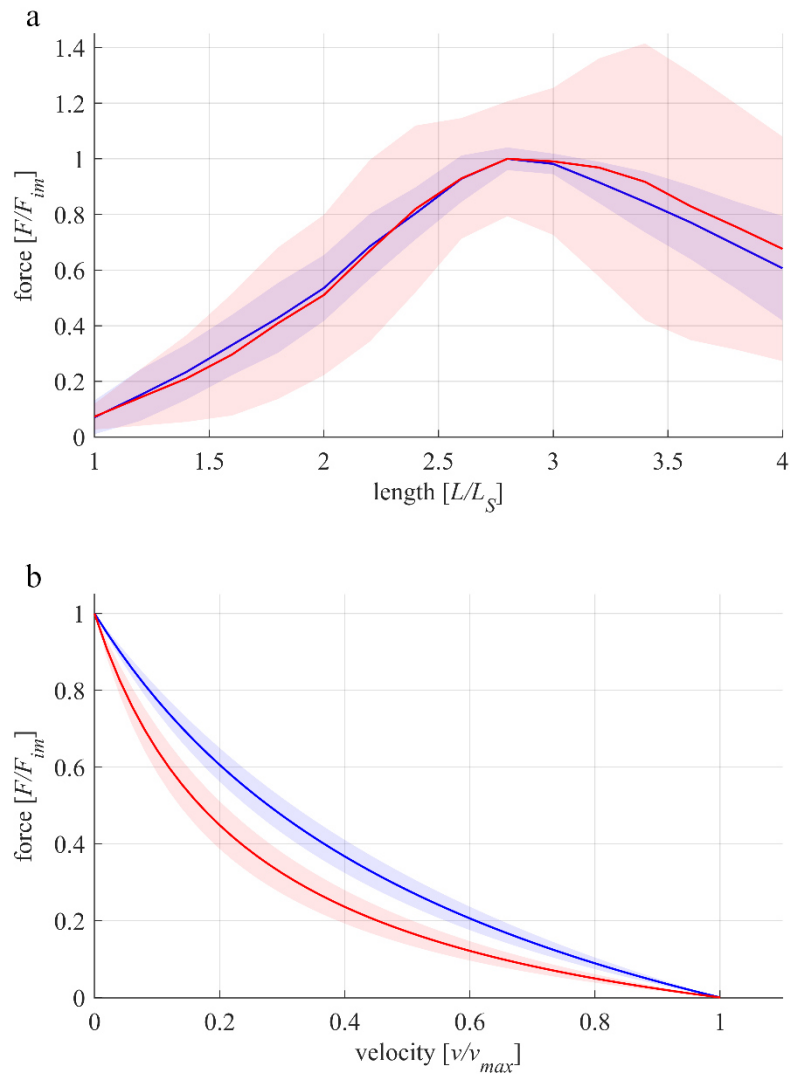


Figure 24. Active muscle properties of whole-muscle strips (WMS: blue color) and isolated layer strips (SLS: red color). The solid curves and light-shaded areas indicate mean values and standard deviations, respectively. (a) Active force-length relationship. Force and length are normalized to maximum isometric force (F_{im}) and slack length (L_S), respectively. Isometric force-length measurements comprise $n = 10$ tissue samples for whole-muscle strips and $n=9$ samples for isolated layer strips. (b) Force-velocity relationship. Velocity and force values are normalized to maximum shortening velocity (v_{max}) and F_{im} , respectively. Based on a series of 6 isotonic contractions, the force-velocity curves of $n = 7$ tissue samples were fitted using the typical Hill equation^{49,144}. Permission to reproduce figure under the terms of the CC-BY license.

The FVR was normalized to F_{im} and v_{max} in **Figure 24b**. Both groups of strips exhibited a typical hyperbolic shape of the FVR. Maximum shortening velocity was lower ($p = 0.0025$, **Figure 25b**) for WMS ($v_{max} = 0.023 \pm 0.005 L_0/s$) compared to SLS ($v_{max} = 0.042 \pm 0.012 L_0/s$). Furthermore, curvature factor of WMS ($curv = 0.664 \pm 0.21$) was significantly higher ($p < 0.001$, **Figure 25c**) than that of SLS ($curv = 0.267 \pm 0.076$). The passive stress-strain relationships of both groups are displayed in **Figure 26**. Both curves were characterized by a course that resembles an exponential increase of stress with muscle length. No statistically significant differences were found between the two groups for p_{pass} .

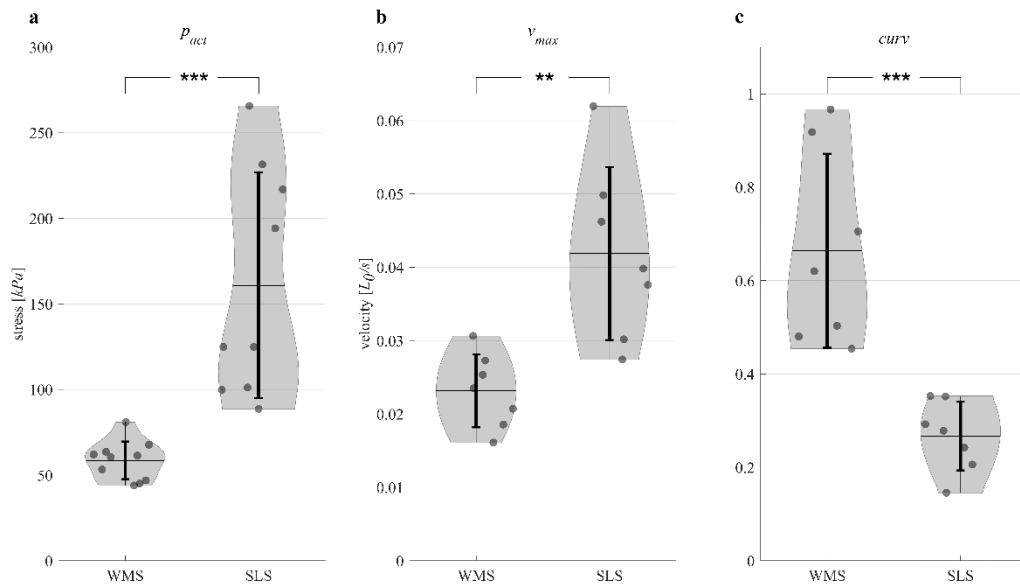


Figure 25. (a) Influence of layer separation on maximum active isometric stress (p_{act}), (b) maximum shortening velocity (v_{max}), and (c) $curv$ factor of the force-velocity relationship (FVR). For whole-muscle strips (WMS) and separated layer strips (SLS), mean values \pm standard deviations are displayed by the black horizontal line and the vertical errorbars, respectively. The transparent black markers indicate the individual datapoints. The shaded area (violin plot ²⁷⁶) illustrates the distribution of the data. Brackets and asterisks (*) mark significant differences. Significance levels are marked as ** $p < 0.01$ and *** $p < 0.001$. Permission to reproduce figure under the terms of the CC-BY license.

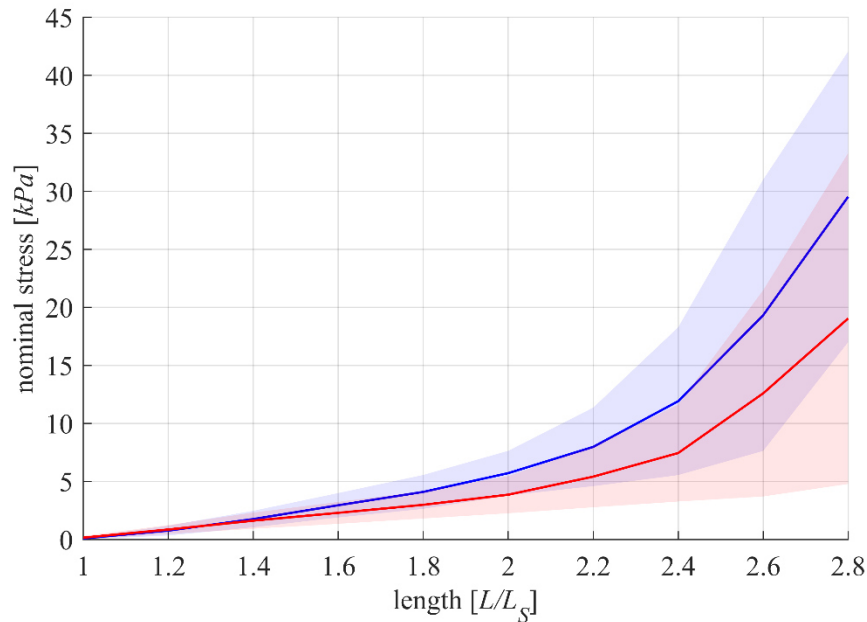


Figure 26. Passive stress-length relationship of whole-muscle strips (blue) and separated layer strips (red). Force is divided by the cross-sectional area (CSA) of the strip at slack length (L_s) to obtain nominal stress. Passive stresses are measured right before activation on each length from isometric experiments. The solid curves and light-shaded areas indicate mean values and standard deviations, respectively. Permission to reproduce figure under the terms of the CC-BY license.

4.4 Discussion

To our knowledge, there has not been a systematic study that examined the influence of layer separation on smooth muscle strip properties. Therefore, the present study performed *in vitro* uniaxial tensile experiments on tissue samples from the fundus of the porcine stomach to characterize the FLR and FVR of WMS and SLS. We found apparent differences in muscle properties determined from shortening contractions, such as in the parameters v_{max} and *curv*. In contrast, there was a negligible influence of layer separation on the normalized FLR-parameters determined from isometric contractions. These results are relevant for the determination of realistic muscle parameters, which are required in muscle models. Moreover, the results presented can be used to check, which parameters in the existing data are influenced by the interaction of multiple muscle layers.

4.4.1 Porcine smooth muscle properties – comparison with the literature

The average p_{act} of 160.9 ± 66.5 kPa generated by separated layer strips can be considered as the pure smooth muscle stress. Histological analyses yielded negligible amount of collagen in the circumferential muscle layer, see **Figure 23c**. Observed p_{act} values are in agreement with stress values, smooth muscles typically generate^{14,85,139,228}. The FLR displayed the typical bell shape of smooth, skeletal and cardiac muscles. The extrapolated range, at which the muscle produced forces (0.35 to $2.08 L_0$), is similar to examined values of other studies on smooth muscles, which lie between $0.13 - 0.38 L_0$ ^{44,76,85,138,140,142,228,267} and $1.82 - 2.17 L_0$ ^{43,44,76,140,228,267}. The average v_{max} of $0.023 \pm 0.003 L_0/s$ and $0.042 \pm 0.012 L_0/s$ of WMS and SLS, respectively, are rather low, but within the range of reported values between $0.016 - 0.6 L_0/s$ of visceral smooth muscles^{44,73,76,86,87,136,138,141,143,145,146,228,260–263,277}. The mean $curv$ of 0.664 ± 0.21 and 0.267 ± 0.076 of WMS and SLS, respectively, is in agreement with values of $0.1–0.8$, found in smooth^{44,76,86,136,139,141–143,145,146,228,260,261,263,268,277} and skeletal muscles¹⁴⁴. The mean p_{pass} of 20.6 ± 13.6 kPa of WMS at L_0 amounts to about 35% of their average p_{act} (58.5 ± 11.5 kPa), which is in accordance with findings of previous studies on smooth muscles^{44,76,141}.

4.4.2 Influence of layer separation on smooth muscle properties

The separation of the circumferential smooth muscle layer affected the shortening characteristics of the examined tissue strips, as WMS displayed lower v_{max} and higher $curv$ than SLS (**Figure 25b, c**). WMS consisted of the circumferential and the longitudinal muscle layers, which were oriented in the lengthwise (e_{circ}) and transversal direction (e_{long}) of the strip, respectively (**Figure 27a**).

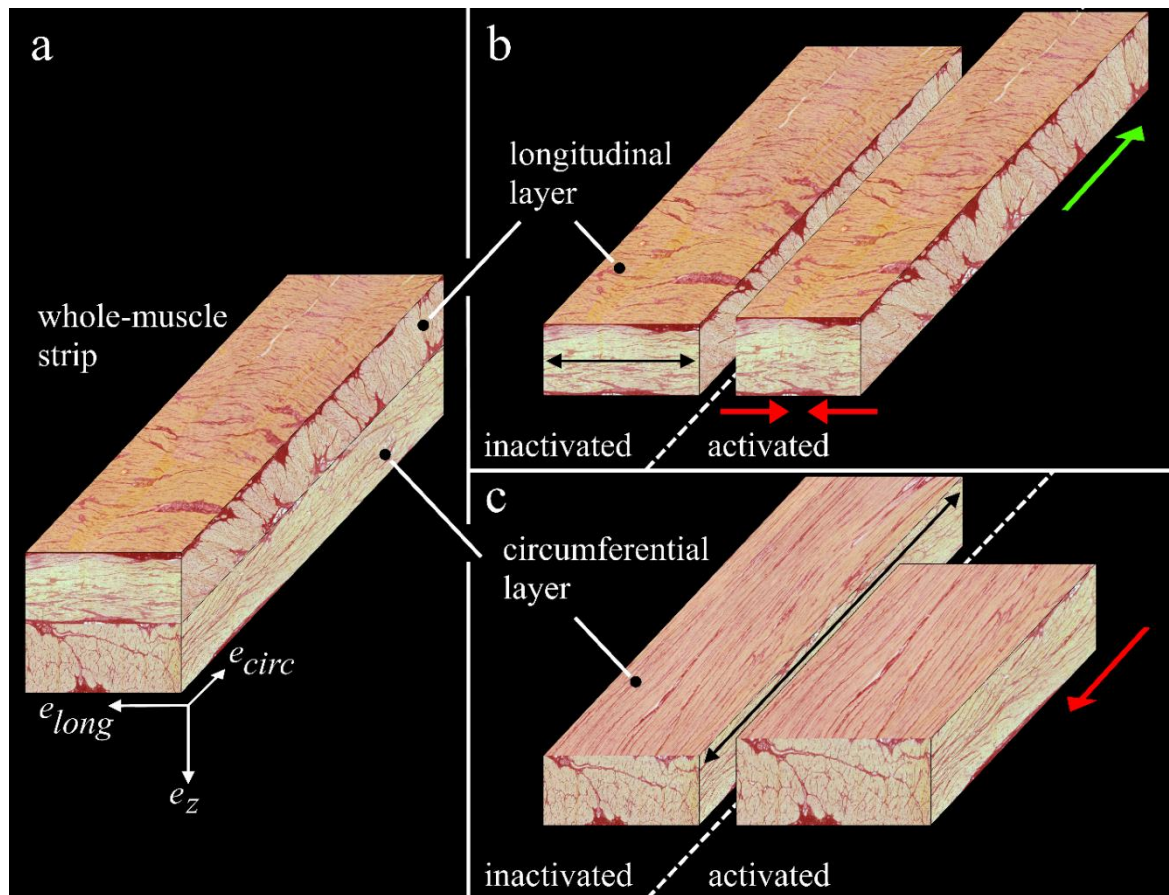


Figure 27. Schematic reconstruction of whole-muscle strips from the porcine stomach during concentric contractions in uniaxial experiments. Strip representation is based on perpendicular histological examinations with Picrosirius Red staining protocol. (a) Whole-muscle strips were cut from the fundus (**Figure 23**) lengthwise to the circumferential smooth muscle layer. They consisted of the outer longitudinal layer (b) and the inner circumferential layer (c). When activated, both layers contracted concentrically along their muscle fiber direction (black arrows in b and c). While the circumferential layer shortened lengthwise (c, red arrow), the longitudinal layer shortened transversally (b, red arrows). Due to volume constancy, the narrowing of the longitudinal layer prompted its simultaneous lengthening (green arrow). Through force transmission between the layers, this lengthening counteracted the shortening of the circumferential layer during the concentric contraction. Consequently, the shortening velocity was decreased in WMS. Permission to reproduce figure under the terms of the CC-BY license.

The two layers may be regarded as isolated, individual muscle layer strips. The muscle fibers of the longitudinal layer strip run along its narrow side (**Figure 27b**, black arrow), whereas the muscle fibers of the circumferential layer strip run along its lengthwise side (**Figure 27c**, black arrow). During isotonic contractions, the circumferential layer shortens along the lengthwise axis of the strip (**Figure 27c**, red arrow), while simultaneously, the longitudinal layer shortens in the transverse direction of the strip (**Figure 27b**, red arrows). The transverse shortening of the

longitudinal layer causes a narrowing of the strip, which causes the strip to lengthen due to expected volume constancy of the muscle tissue. This lengthening is directed opposite the shortening of the circumferential muscle layer. Similar to myofascial force transmissions in skeletal muscles^{118,119}, force transmission occurs between the neighboring smooth muscle layers. The lengthening of the longitudinal layer counteracts the concentric contraction of WMS, reducing its shortening velocity. As SLS do not contain the longitudinal layer, this effect does not apply, and the shortening velocity of SLS is not reduced. Therefore, SLS exhibited higher v_{max} than WMS (**Figure 25b**). The shortening velocity of WMS was reduced more markedly compared to SLS at concentric contractions against low relative forces (high velocities) (**Figure 28**).

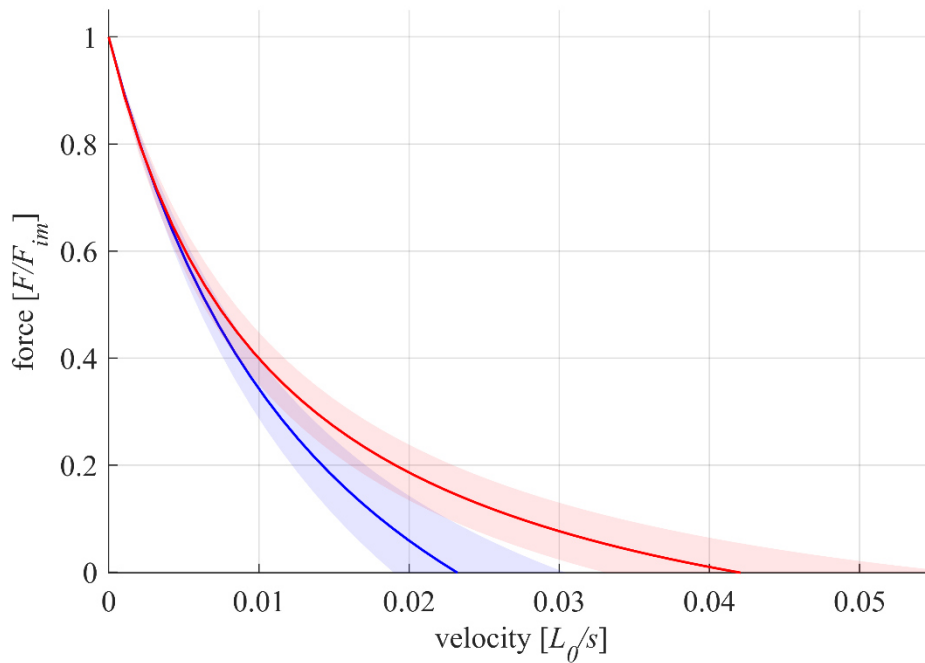


Figure 28. Force-velocity relationship of whole-muscle strips (blue) and separated layer strips (red). Velocity and force values are normalized to optimum muscle length (L_0) and maximum isometric force (F_{im}), respectively. Based on a series of 6 isotonic contractions, the force-velocity curves of $n = 7$ tissue samples were fitted using the typical Hill equation^{49,144}. Permission to reproduce figure under the terms of the CC-BY license.

During isometric contractions ($v=0$) no or negligible change in WMS strip length is expected. Due to volume constancy, this would result in no or negligible lengthening of the longitudinal layer and thus no or negligible counteracting forces of the longitudinal layer during isometric contractions. Counteracting forces of the longitudinal layer might decrease with decreasing

velocity due to velocity-dependent viscoelastic properties of muscle tissue ²⁷⁸ and velocity-dependent damping properties of the FVR.

For the comparison of isometric contractions, the FLR was determined. As a result, the layer separation did not affect the shape of the FLR. However, the p_{act} was higher in SLS than WMS. While both groups consisted predominantly of muscle tissue, the longitudinal layer of the WMS did not generate tensile forces along the measuring force axis during isometric contractions due to the orientation of its muscle fibers in the transversal direction. Therefore, the active stress of WMS was lower due to the higher CSA of the WMS strip. Nevertheless, it remains a question whether the pure muscle stresses of the SLS and the WMS were different if the WMS force will be normalized by the CSA of only the tensile force-generating muscle tissue, i.e., its circumferential layer. However, for a valid analysis of such a parameter, determining CSA of both WMS muscle layers by histological examinations of all tested samples would be necessary, which was not performed in the present study.

The p_{pass} and the course of the nominal stress with increasing length did not differ between WMS and SLS (**Table 6**). This suggests an isotropic passive behavior of the smooth muscle tissue in the gastric fundus, agreeing with observations of studies that conducted biaxial experiments on tissue strips from this region ^{16,93}.

4.4.3 Relevance for studies on smooth muscle strips

It was shown that the examined muscle properties through uniaxial experiments are dependent on whether the muscle layers of smooth muscle strips are separated or not. From a physiological point of view, it would be preferable to separate the muscle layers, so smooth muscle properties are not influenced by such side effects. However, whole-muscle tissue strips represent more realistic samples for the organ wall *in vivo*, and hence may be more suitable for the three-dimensional modeling of organs. Furthermore, depending on the organ, or the animal from which the smooth muscle strips are harvested, it may not be possible to separate the muscle layers. For example, some regions of the bladder wall do not contain clearly separate muscle layers but rather multiple, differently oriented muscle fibers ¹². Studies on the stomach of guinea-pigs ¹⁴³ or the

intestine of rabbits ¹¹ report difficulties in separating the muscle layers, as this was not possible without potentially damaging the tissue. In this case, biaxial tension testing ^{12,77,83} of muscle tissue is recommended.

In sum, uniaxial experiments are a valid method to determine smooth muscle properties, especially if separated muscle layers were used. However, when conducting experiments on strips with multiple muscle layers, the effect of a transversal shortening needs to be considered and discussed.

4.5 Conclusion

The present study examined the influence of layer separation on the muscle properties of smooth muscle strips from the porcine stomach. SLS displayed higher v_{max} than WMS, as the contraction of the longitudinal layer of the WMS with its transversally oriented muscle fibers affected the shortening velocity. This effect is weaker with decreasing shortening velocity, which results in a lesser curvature (higher $curv$ parameter) of the force-velocity relation of WMS compared to SLS. The FLR showed no differences in shape between the groups. However, SLS generated a higher p_{act} than WMS. This was due to higher CSA of WMS compared to SLS with the same amount of circumferential muscle layer tissue in WMS and SLS generating force in the direction of the force-measuring axis. The results of this study show that the determination of smooth muscle properties through uniaxial experiments may depend on whether the muscle layers are separated or not.

Declarations

Funding

This work was funded by the Deutsche Forschungsgemeinschaft (DFG) under Grants SI 841/12-1 and BO 3091/18-1.

Conflict of interest

All authors have no conflicts of interest.

Availability of data

The datasets generated during and/or analysed during the current study are available from the corresponding author on reasonable request.

Author contributions

Mischa Borsdorf: Wrote the paper, conducted the experiments, and analyzed the data. Markus Böl: Review and editing, coordinated the study. Tobias Siebert: Designed and coordinated the study, wrote the paper.

Ethics approval

The study was exempted from ethical committee review according to the National Regulations (German Animal Welfare Act) as porcine stomach smooth muscle tissue was obtained from a slaughterhouse immediately after animal sacrifice.

5 General Conclusion

Due to their central role within their respective body system, the normal functioning of the stomach and urinary bladder is highly important for the health and well-being of an organism. Acting as the motor of inner organs, smooth muscles are of special interest. They actively generate forces and movements to prompt and regulate the transportation of inner contents and thereby fulfill major tasks of the various body systems. A holistic comprehension of an organ's smooth muscle structure and function is essential in advancing the prediction, prevention, evaluation, and treatment of several dysfunctions and diseases.

Computational, three-dimensional models are able to depict the mechanical behavior of the healthy organ realistically. By manipulation of input parameters, models can simulate pathophysiological alterations of an organ's structure and function, as they characteristically occur *in vivo*, and in turn, simulate how medical treatments, such as surgical procedures or medications, were to reestablish normal organ functioning. Thereby, computational modeling enables a better understanding and evaluation of several dysfunctions and helps to establish and improve medical treatments. However, the development and validation of integrative, realistic models rely on the acquisition of experimental data.

The present thesis aimed to advance the knowledge about smooth muscle microstructure and biomechanics in general, and particularly in the context of their functions within the stomach and urinary bladder. Hence, this thesis derived logical conclusions and generated valuable data about the stomach and urinary bladder's active and passive biomechanical behavior. These, in turn, can be integrated into existing and future biomechanical models for a more realistic and holistic depiction of these organs' healthy and normal operation.

Generally, it was shown that the biomechanics of inner organs are dependent on their individual functions or their suspension within the body. Thereby, some may exhibit large regional differences in smooth muscle structure and contractility (e.g., the vagina⁹¹ or the stomach¹⁶) due to their simultaneous performance of multiple functions, whereas others show minor regional differences (e.g., the bladder, see **Chapter 5.2**), as they perform only one major task at a time (the bladder either storing or emptying). Organs may show anisotropic passive biomechanical

properties (e.g., the bladder, see **Chapter 5.2**), while a part of another organ with similar functions exhibits rather isotropic characteristics (e.g., fundus in the stomach ¹⁶, see **Chapter 5.3**).

Moreover, it has been shown that the multi-layered composition of organ walls greatly affects an organ's biomechanics. On the one hand, the layers contribute differently to the load-bearing process of the organ wall (e.g., the stomach, see **Chapter 5.3**); on the other hand, the determination of active muscle properties is dependent on whether the differently directed muscle layers are separated or not (e.g., stomach tissue strips, see **Chapter 5.4**).

Overall, this thesis provided insights and valuable datasets about stomach and bladder motility (**Chapter 2 & 3**), advancing and improving the computational modeling of these organs. Furthermore, an effect has been proposed (**Chapter 4**), which occurs within uniaxial tensile tests and needs to be considered when evaluating and discussing past and future results from uniaxial tensile experiments on smooth muscle strips. Furthermore, future studies may include this additional viewpoint when developing their methods to investigate their objective more precisely.

5.1 Differences in the methodology of determining smooth muscle properties

The methodology of determining smooth muscle properties, including the experimental set-up, as well as the preparation and handling of smooth muscle tissue, varied between the individual studies of this thesis in a few aspects. On the one hand, the acidic content of the stomach made it necessary to adjust the applied methods compared to other smooth muscle preparations; on the other hand, with gaining experience throughout the numerous conducted tests, optimizations in the experimental procedures were implemented. These muscle-specific optimizations yielded, e.g., more stable preparations over the experimental time and more reproducible results.

Active experiments on urinary bladder tissue were conducted with all wall layers attached, whereas this was not possible for stomach tissue. The mucosa of the stomach was soaked in acid gastric juice, which caused muscle degeneration when it came in contact with the muscular tissue. It was attempted to thoroughly wash away the gastric juice before the storage of the tissue. Nevertheless, active muscle experiments were still not feasible due to vastly diminished active force of the stomach tissue strips. This might be ascribed to the soaked state of the mucosa or due

to its function to secrete gastric juice⁵¹, leading to an ongoing secretion during storage and experiments. Hence, similarly to other studies^{44,137,143}, the mucosal and submucosal layers of stomach tissue strips were removed before putting the tissue in the Krebs solution for storage and transportation.

Another major difference was the presence of spontaneous contractions in stomach muscle strips. Initial experiments (**Chapter 3**) were thereby conducted at a lower temperature of 32° C, at which no such occurrences were observed. However, spontaneous contractions could also be suppressed by adding methylene blue into the solution. Methylene blue is usually used in microscopic analyses to stain and visualize ICC's²⁷⁹. However, it also suppresses the ICCs' generation of slow waves and hence eliminates the ensuing spontaneous contractions^{273,274,280}, whereas smooth muscle cells, on the other hand, remain intact²⁷⁴. Thereby, experiments on stomach smooth muscles could be realized at a physiological temperature of 37° C with methylene blue added to the Krebs solution (**Chapter 4**).

For the study in **Chapter 4**, further adjustments were made to the experimental protocol and set-up. It was found that 5-minute intervals between contractions were sufficient for a stable, high active force generation, and larger length increments than 10% L_S could be applied to properly determine the FLR. Hence, the interval time was cut from 7 to 5 min, and the number of isometric contractions to investigate the FLR was reduced, using length increments of 20% L_S . Also, the strip fixation was changed from an alligator clamp and hooks to sewing the strip to rectangular blocks via braided fishing lines. Thereby, the strips could freely deform in the transversal direction.

Furthermore, the CSA was calculated either by measuring the width and depth of the strips, assuming a rectangular shape⁴⁴, or from the strip's volume by measuring the length of the strips and the wet weight, assuming a density of 1.05 g/mm³²⁶⁶. While both methods are valid and have been applied in various studies^{44,260,266,281} yielding similar CSAs²⁶⁶, the strip thickness measurement was more complex due to the serosal folds in the stomach strips leading to an irregular, wave-like strip thickness. Whereas the mean strip thickness could be approximated precisely by measuring at multiple locations, the calculation of the CSA via volume and density proved to be less time-consuming, while delivering similar results.

5.2 Locational and directional smooth muscle properties of the urinary bladder

The detrusor is the smooth muscular layer lining the urinary bladder, which enables its cycle of filling and emptying by sustained relaxations and periodic contractions, respectively. It is categorized as a phasic, fast smooth muscle³⁶, which contains single-unit smooth muscle cells interconnected through gap junctions⁵⁷. Thereby, the micturition reflex initiates a fast and transient, synchronized contraction of the detrusor, which quickly reduces the bladder's volume and squeezes its content via the urethra out of the body. It was shown that the smooth muscle tissue exhibits uniform contractile properties among the bladder's various regions, as well as in the longitudinal- and the circumferential direction (**Chapter 2**). Thereby, the detrusor is able to compress the bladder homogeneously to successfully discharge all of its content at once. Afterward, the process of bladder filling can fluently start again. A uniform contraction is of particular importance, as it facilitates the complete emptying of the bladder and thereby avoids remaining residual urine, which increases the risk for bacterial urinary tract infections²⁸².

The bladder exhibits microstructural differences in dependence on location and direction. The smooth muscle fibers are predominantly arranged in the longitudinal orientation, by which the bladder is able to generate higher active stress in this direction. In pigs, this might be required to better overcome gravitational force, as the urethral orifice is located above the bladder¹². The predominantly longitudinal fiber arrangement may also lead to a higher passive stiffness along the bladder's length axis, reducing the mechanical strain on the ligaments that fixate the bladder to the pelvis¹². It should be noted that some studies similarly report higher stiffness in the longitudinal direction^{12,70,77,78}, whereas several others made contrary findings^{75,79,80}. Ambivalent results in the literature on the bladder's passive behavior may be explained by differences in the methods, which have been discussed in detail in⁷⁵. Nevertheless, consistent with other studies^{12,70}, the bladder was found to be stiffer in the trigone compared to the body and apex, which can be explained by an increased collagen content^{12,70}. At the trigone, the urine enters and exits the bladder via the ureters and urethra, respectively. The higher passive stiffness in this region restrains larger deformations and could thereby prevent possible disturbances of these processes' steady and normal functioning.

When putting these findings in a greater context, gender- and species-specific differences should be considered. The bladder of female pigs is smaller, as the uterus occupies space just superior to the bladder, whereas the prostate lies inferior to the bladder in males ⁶¹. Thereby, interactions with these organs could lead to differently exerted pressure on the bladder and hence to biomechanical variations. Moreover, the upright posture of humans in contrast to pigs may lead to dissimilar bladder characteristics due to gravitational force effects, which should be considered when translating animal models to human organs. Furthermore, as proposed in **Chapter 4**, the determined biomechanical properties regarding the shortening characteristics may have been affected by the tissue strips' differently oriented muscle fibers. Bladder smooth muscle tissue should therefore exhibit faster shortening velocities on a cellular or single bundle level compared to the examined specimens. However, comparisons of contractile muscle properties within this study are to be considered valid, as all specimens contained the whole muscle tissue, and hence the described effect was to apply to all investigated subjects.

In conclusion, the presented results contribute to the understanding of how the healthy bladder actively contracts and empties its contents, and how it deforms during expansion in the passive storage phase. Incorporated into biomechanical models of the whole organ, the acquired data help describe both passive and active bladder behavior. While passive bladder characteristics have been analyzed for locational or directional differences numerous times ^{12,70,75,79,80,283,284}, the provided results are especially of great value, as a new and broad dataset on active biomechanical smooth muscle properties in this regard is given. A complete, holistic understanding of bladder biomechanics is especially beneficial for improving surgical procedures that augment the bladder or replace diseased bladder tissue, as the sewn-in tissue needs to be biomechanically equivalent to the bladder tissue. Typically, patches from the intestine or the ureters are used as a replacement, although these exhibit dissimilar mechanical properties ²⁸⁵ and bring about short- and long-term complications ^{120,121,286,287}. Thereby, the replacement by synthetically engineered biomaterials presents a promising alternative ²⁸⁸. However, this method has several reports of non-satisfactory outcomes, particularly due to limited biomechanical capabilities of the treated bladder ²⁸⁹. With the advancement of computational bladder models through the integration of new and manifold data, as provided in this thesis, the quality and practicability of synthetically engineered tissue

shall vastly improve in the future. Ultimately, with more insights into specific bladder properties, synthetic biomaterials may reliably replace diseased bladder tissue to successfully restore normal urinary function.

5.3 Layer and direction dependent properties of the stomach wall

The stomach is a complex organ with distinct regions and layers, tasked with various functions. The fundus and upper corpus have a storage function, accommodating food through relaxation of the muscle tissue, whereas the lower corpus and antrum act as food grinder and propeller, mechanically digesting the food through fast phasic contractions. As the stomach undergoes enormous deformations, the mechanical properties of the stomach wall are of high importance. Its main components are the muscular layer, which mainly acts as a motor for the stomach's motility, and the mucosal layer, mainly functioning as a barrier between the stomach's content and its muscular layer, and secreting gastric juice. Data on the stomach's biomechanics can be incorporated into organ models to realistically depict the stomach's passive and active behavior.

Mechanical experiments on stomach strips from the fundus, either featuring all layers or with the mucosal layers removed, showed that the mucosal layer contributes to the passive stiffness of the organ wall only after a certain stretch threshold (**Chapter 3**). The mucosa needs to be pulled beyond its crimped state first and only then begins to bear a considerable load. With higher stretches, it eventually becomes the predominant load-bearing component compared to the muscular layer. Thereby, the mucosal layer enables the stomach to expand to larger volumes while maintaining a low inner pressure. Furthermore, it protects the muscular layer from being overstretched by extensive stomach deformations. These results are in agreement with a recent study that conducted biaxial experiments, which investigated and discussed passive stomach behavior in great detail ¹⁶. The fundus was further found to be slightly stiffer in the longitudinal than in the circumferential direction, as well as to generate higher active stress in this direction. The acquired data on the mechanical properties of longitudinal and circumferential muscle strips were incorporated into a three-dimensional model of gastric smooth muscle contraction to illustrate the excitation-contraction coupling mechanism of the stomach on a whole organ level

(**Chapter 3**). This model features a novel simulation of the complex spatio-temporal regulation of the stomach's calcium-dependent contraction and relaxation in respect to mechanical stretches of the ICCs and SMCs.

5.4 Uniaxial tensile experiments

Active muscle properties of smooth-, as well as of striated muscles^{68,69}, are typically investigated through *in vitro* uniaxial tensile experiments^{76,143,266}. Muscle tissue is characteristically fixated so that the muscle fiber orientation coincides with the force measuring axis, allowing for a precise detection and quantification of muscle properties. However, smooth muscle tissue from organ walls, such as the stomach and urinary bladder, characteristically feature differently oriented muscle fiber bundles or layers. Whereas some studies conducted experiments on isolated muscle layers^{85,265,272}, muscle bundles^{73,87,138,146}, or single smooth muscle cells¹⁴, it is also common to perform uniaxial experiments on tissue strips that feature the whole muscle layer, and therefore differently oriented fibers. On the one hand, it was reported that it was hardly possible to separate the muscle layers of small specimens without damaging the tissue^{11,143}; on the other hand, whole-muscle tissue strips represent the organ wall's behavior *in vivo* more closely, delivering more holistic information for organ models. Although accompanied microstructural investigations can be applied to detect the amount of smooth muscle tissue aligned to the measuring axis and hence facilitate the calculation of pure muscle stress values, the differently oriented muscle fibers shall not be perceived as a mere passive component. It was shown that in whole-muscle strips of the stomach, the shortening characteristics are impaired compared to separated layer strips that feature a uniform muscle direction (**Chapter 4**). As the differently oriented muscle fibers co-contract upon activation, they prompt a shortening in the transversal direction of the measuring axis and consequently induce a strip narrowing. Due to assumed volume constancy, a strip narrowing causes the strip to lengthen, which counteracts the contraction of the strips in the measured axis. Thereby their shortening velocity in the measured axis is decreased, whereas particularly shortenings at higher velocities are affected. The force-velocity relationship of whole-muscle strips consequently displays a decreased maximum shortening velocity and a higher curvature factor than separated layer strips.

These results provide a new viewpoint for analyzing and interpreting past and future results of studies that include uniaxial experiments on muscle strips containing fibers with deviant orientations. This effect needs to be considered and discussed, particularly when putting the acquired data about biomechanical smooth muscle properties into a greater context. With more data on this effect, it could be possible to calculate single muscle layer properties from whole-muscle tissue models and vice versa, under the condition that the microstructure, including muscle composition and fiber orientation, are known. However, a prerequisite for such a method is the knowledge about the mechanical coupling between the individual layers. This could be investigated through peeling experiments, which measure the force required to separate layers^{290–294}. By including this new viewpoint, data from various studies can be better compared, and *in vitro* smooth muscle characteristics can be better interpreted regarding the behavior of the corresponding organ *in vivo*.

Moreover, the methodology of future studies can be adjusted to their specific objective, whether they aim to yield more practicable data and depict the organ's behavior more realistically, or whether they intend to investigate general smooth muscle tissue behavior and its phenomena. The samples are to consist of all organ wall layers (as in the study from **Chapter 2**) for the former objective, and experiments are to be realized on muscle strips or bundles featuring a uniform fiber orientation for the latter.

5.5 Comparison between the stomach and bladder

The stomach and the urinary bladder show similarities in their wall composition, as well as in their function as a temporary reservoir for their respective inner content. Although the stomach additionally has the task of chemically and mechanically digesting its content, the proximal region (fundus), which has been investigated in this thesis, has the main function of accommodating and storing food. Consequently, it is interesting to compare the urinary bladder and the stomach's fundus mechanics of storing and propelling/ emptying their respective content.

The tunica muscularis of both these organs is comprised of differently oriented smooth muscle fibers. The fundus features two distinct muscle layers oriented orthogonally to each other either in

the longitudinal- (outer layer) or in the circumferential direction (inner layer), whereas the fibers in the bladder are formed in interwoven bundles which are directed in diverse orientations¹². Thereby, the tissues in both organs are able to uniformly contract and return to their initial shape after being deformed by storing food/ urine for a period of time. To accommodate their content, the muscle tissue relaxes, whereby the mucosal layer protects the muscular tissue from overstretching while allowing the organs to maintain little inner pressure during initial expansion, as its folds (rugae) need to be stretched out first^{16,77}. To transport their content, the fundus gradually increases its tone and slowly pushes the food forward through a tonic contraction. In contrast, the bladder quickly contracts after being initiated by the micturition reflex to rapidly and forcefully discharge all urine out of the body. Hence, there is a clear difference in the contractile kinetics, as shown by the bladder's maximum shortening velocity of 0.071 L_0/s (whole-tissue strips) in contrast to the fundus' 0.023 L_0/s (whole-muscle strips, without mucosal layers). It should be noted that there were small variations in the method of determining the muscle properties (see **Chapter 5.1**). Nevertheless, the contrast in these tissues' shortening characteristics is apparent, as visualized in **Figure 29**, showing the FVR of tissue strips from the stomach's fundus compared to strips from a representative region of the bladder. These results support that the fundus consists of tonic-^{53,295}, and the bladder consists of phasic smooth muscle tissue^{36,53}. Regarding the FLR and the generated muscle stresses, no such decisive differences were noticeable. Both tissues were able to generate forces over a large range of muscle lengths and the maximum pure active muscle stress was similar, averaging ca. 160 kPa. A more valid determination of the muscles' shortening characteristics should, however, be realized by conducting experiments on strips that consist of only one fiber direction (as shown in **Chapter 4**). Consequently, smooth muscle can be classified more reliably into a tonic or phasic type in connection with their signaling and metabolic properties

36.

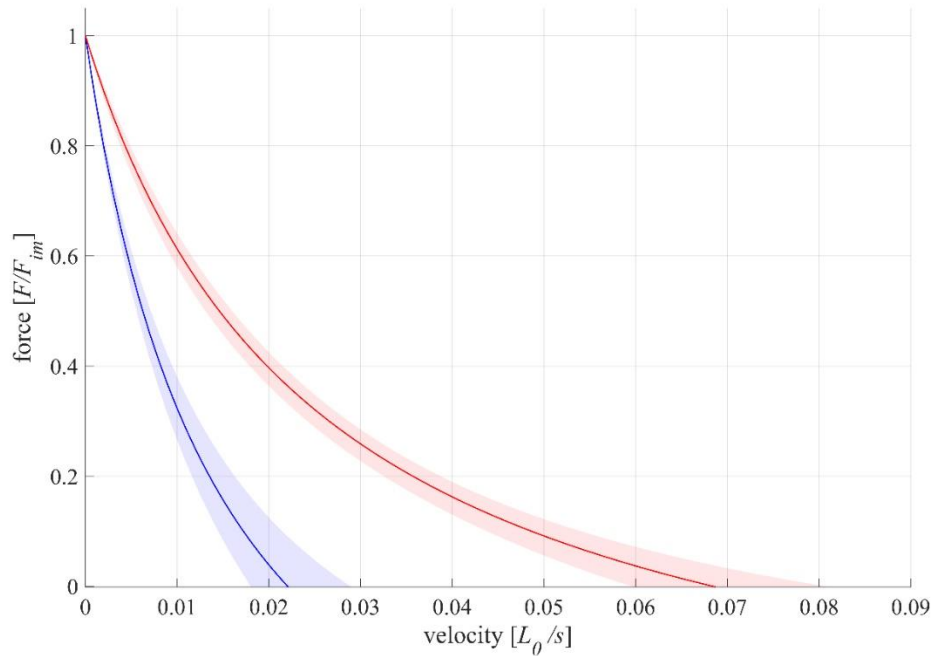


Figure 29. Comparison of the force-velocity relationship (FVR) between circumferential whole-muscle strips from the stomach’s ventral fundus (blue, n=6) and, representative for the bladder, circumferential whole-tissue strips from the dorsal trigone (red, n=6). The solid curves and light-shaded areas indicate mean values and standard deviations, respectively. Velocity and force values were normalized to optimum length (L_0) and maximum isometric force (F_{im}), respectively. Based on a series of isotonic contractions, the force-velocity curves were fitted using the typical Hill equation^{49,144}. The mean maximum shortening velocity (v_{max}) and *curv* of stomach strips were $0.023 L_0/s$ and 0.664 , respectively, those of bladder strips were $0.069 L_0/s$ and 0.379 , respectively.

5.6 Prospects

Smooth muscle tissue remains an exciting and highly valuable research topic, requiring further studies to understand its structural and functional properties more thoroughly. On the one hand, manifold data on biomechanical organ wall characteristics that describe the organ’s motility are required to extend and improve computational, three-dimensional organ models. The model validation can then take place based on measurement data at the whole organ level (e.g. 3D organ deformation²⁹⁶, pressure-volume curves²⁹⁷). On the other hand, the basic mechanism of a smooth muscle contraction is not as deeply understood as in striated muscle²⁹⁸, leaving several phenomena yet to be examined. Thereby, history effects, for example, have been analyzed and discovered in

smooth muscle only recently ^{44,76,299}, whereas these have been studied in skeletal muscle since as early as the 1950s ³⁰⁰. History effects describe the dependence of a muscle's force on its kinematics in the activated state ultimately before the contraction. They have decisive functional implications, whereby multiple hypotheses about their underlying mechanism were proposed ^{301,302}. It was suggested that the protein titin, which holds and stabilizes the myosin filaments in sarcomeres, binds to actin during activation ³⁰¹. This reduces its spring length prompting higher forces during eccentric contractions in addition to those exerted by the cross-bridges ³⁰¹. While this mechanism affects the force production considerably, it has only been investigated in smooth muscle sparsely, despite observations of a similar protein to titin termed smitin ³⁰³. Hence, a similar mechanism may exist in smooth muscle, by which further studies on history effects could yield additional valuable knowledge and insights about the contraction process of smooth muscles.

Similarly, the mechanism that leads to the decline in generated force at shorter muscle lengths (ascending limb of the FLR) has been investigated much more intensively in skeletal muscle, with intuitive and logical explanations proposed recently ³⁰⁴. In contrast, there are only a few studies that focused on this subject in smooth muscle tissue ^{44,76,299}. Hence the contraction mechanism at short lengths is not as thoroughly comprehended, presenting a considerable knowledge gap. Thereby, studies on the basic mechanisms and phenomena of smooth muscle, as the mentioned history effects and contractions at short lengths, could prove to be of high value, yielding knowledge that is applicable for all smooth muscles and hence various organs. As concluded from **Chapter 4**, such examinations on pure smooth muscle function should be conducted either on isolated muscle cells or on bundles/strips that contain only one direction of fibers to eliminate side-effects that influence and impair the determined muscle characteristics.

Otherwise, of great worth would be the investigation of the stomach regarding locational differences of active biomechanical muscle properties, as similarly performed within this thesis on the bladder. Due to the distinct functions of the stomach's regions, there may be significant differences in contractile characteristics, which would have a substantial impact on stomach modeling, as well as on the understanding of tonic and phasic smooth muscle types. Moreover, as they have only been performed in studies on passive biomechanics of the stomach and urinary bladder, biaxial experiments could also be conducted in the future to examine active muscle

properties. These were to generate new, valuable data, as measurements of the tissue's deformation and contraction were realized in two dimensions, mimicking the *in vivo* behavior of the organ wall more closely. Furthermore, *in vitro* experiments on the whole organ, by which the deformation and inner pressure during passive filling and active emptying are analyzed in detail, would yield further data on the organs' biomechanics and advance the development and validation of new and existing computational models, respectively. In the end, holistic three-dimensional models that realistically depict the biomechanical characteristics of the healthy and diseased organ, and integrate further aspects such as electrochemical or metabolic properties up to interorgan effects, shall enable the development of synthetically engineered biomaterials, which is able to replace diseased organ tissue or even whole organs.

6 Bibliography

1. Vermillion, D. L., Huizinga, J. D., Riddell, R. H. & Collins, S. M. Altered small intestinal smooth muscle function in Crohn's disease. *Gastroenterology* **104**, 1692–1699 (1993).
2. Montero, D. *et al.* Vascular smooth muscle function in type 2 diabetes mellitus: A systematic review and meta-analysis. *Diabetologia* **56**, 2122–2133 (2013).
3. Nagatomi, J., Toosi, K. K., Grashow, J. S., Chancellor, M. B. & Sacks, M. S. Quantification of bladder smooth muscle orientation in normal and spinal cord injured rats. *Ann. Biomed. Eng.* **33**, 1078–1089 (2005).
4. Mimata, H., Satoh, F., Tanigawa, T., Nomura, Y. & Ogata, J. Changes of rat urinary bladder during acute phase of spinal cord injury. *Urol. Int.* **51**, 89–93 (1993).
5. Dohi, Y., Kojima, M., Sato, K. & Lüscher, T. F. Age-related changes in vascular smooth muscle and endothelium. *Drugs Aging* **7**, 278–291 (1995).
6. Bitar, K., Greenwood-Van Meerveld, B., Saad, R. & Wiley, J. W. Aging and gastrointestinal neuromuscular function: insights from within and outside the gut. *Neurogastroenterol Motil.* **23**, 490–501 (2011).
7. Cheng, L. K. *et al.* Strategies to refine gastric stimulation and pacing protocols : experimental and modeling approaches. **15**, 645472 (2021).
8. Cai, X. Regulation of smooth muscle cells in development and vascular disease: current therapeutic strategies. *Expert Rev. Cardiovasc. Ther.* **4**, 789–800 (2006).
9. Turner, W. H. & Brading, A. F. Smooth muscle of the bladder in the normal and the diseased state: pathophysiology, diagnosis and treatment. *Pharmacol. Ther.* **75**, 77–110 (1997).
10. An, S. S. *et al.* Airway smooth muscle dynamics: a common pathway of airway obstruction in asthma. *Eur. Respir. J.* **29**, 834–860 (2007).
11. Elbrønd, H., Tøttrup, A. & Forman, A. Mechanical properties of isolated smooth muscle from rabbit sphincter of oddi and duodenum. *Scand. J. Gastroenterol.* **26**, 289–294 (1991).
12. Morales-Orcajo, E., Siebert, T. & Böl, M. Location-dependent correlation between tissue structure and the mechanical behaviour of urinary bladder. *Acta Biomater.* **75**, 263–278 (2018).
13. Biancani, P., Zabinski, M., Kerstein, M. & Behar, J. Lower esophageal sphincter mechanics: anatomic and physiologic relationships of the esophagogastric junction of cat. *Gastroenterology* **82**, 468–475 (1982).
14. Harris, D. E. & Warshaw, D. M. Length vs. active force relationship in single isolated smooth muscle cells. *Am. J. Physiol.* **260**, C1104–C1112 (1991).
15. Gunst, S. J. & Tang, D. D. The contractile apparatus and mechanical properties of airway

- smooth muscle. *Eur. Respir. J.* **15**, 600–616 (2000).
16. Bauer, M. *et al.* Biomechanical and microstructural characterisation of the porcine stomach wall: location- and layer-dependent investigations. *Acta Biomater.* **102**, 83–99 (2020).
 17. Peery, A. F. *et al.* Burden of gastrointestinal disease in the united states: 2012 update. *Gastroenterology* **143**, 1179–1187 (2012).
 18. Bray, F. *et al.* Global cancer statistics 2018: GLOBOCAN estimates of incidence and mortality worldwide for 36 cancers in 185 countries. *CA. Cancer J. Clin.* **68**, 394–424 (2018).
 19. Etemadi, A. *et al.* The global, regional, and national burden of stomach cancer in 195 countries, 1990–2017: a systematic analysis for the Global Burden of Disease study 2017. *Lancet Gastroenterol. Hepatol.* **5**, 42–54 (2020).
 20. Irwin, D. E. *et al.* Population-based survey of urinary incontinence, overactive bladder, and other lower urinary tract symptoms in five countries: results of the EPIC study. *Eur. Urol.* **50**, 1306–1315 (2006).
 21. Patterson, J. K., Lei, X. G. & Miller, D. D. The pig as an experimental model for elucidating the mechanisms governing dietary influence on mineral absorption. *Exp. Biol. Med.* **233**, 651–664 (2008).
 22. Kararli, T. T. Comparison of the gastrointestinal anatomy, physiology, and biochemistry of humans and commonly used laboratory animals. *Biopharm. Drug Dispos.* **16**, 351–380 (1995).
 23. Teufl, F., Dammann, F. & Wehrmann, M. In vitro study of morphology of the bladder wall using MR tomography at 1.0 Tesla: correlation with histology. *Rofo* **166**, 406–410 (1997).
 24. Dahms, S. E., Piechota, H. J., Dahiya, R., Lue, T. F. & Tanagho, E. A. Composition and biomechanical properties of the bladder acellular matrix graft: comparative analysis in rat, pig and human. *Br. J. Urol.* **82**, 411–419 (1998).
 25. Mahadevan, V. Anatomy of the stomach. *Surgery* **35**, 608–611 (2017).
 26. Andersson, K.-E. E. & Arner, A. Urinary bladder contraction and relaxation: physiology and pathophysiology. *Physiol. Rev.* **84**, 935–986 (2004).
 27. Hobson, A. R. & Aziz, Q. Oesophagus and stomach motility. *Medicine (Baltimore)*. **39**, 210–213 (2011).
 28. Sherwood, L. *Human physiology - from cells to systems*. (Cengage Learning, 2016).
 29. Craig, R. & Megerman, J. Assembly of smooth muscle myosin into side-polar filaments. *J. Cell Biol.* **75**, 990–996 (1977).
 30. Xu, J. Q., Harder, B. A., Uman, P. & Craig, R. Myosin filament structure in vertebrate

- smooth muscle. *J. Cell Biol.* **134**, 53–66 (1996).
31. Isshiki, M. & Anderson, R. G. W. Function of caveolae in Ca²⁺ entry and Ca²⁺ - dependent signal transduction. *Traffic* **4**, 717–723 (2003).
 32. Huxley, A. F. Muscle structure and theories of contraction. *Prog. Biophys. Biophys. Chem.* **7**, 255–318 (1957).
 33. Huxley, A. F. & Niedergerke, R. Structural changes in muscle during contraction; interference microscopy of living muscle fibres. *Nature* **173**, 971–973 (1954).
 34. Huxley, H. & Hanson, J. Changes in the cross-striations of muscle during contraction and stretch and their structural interpretation. *Nature* **173**, 973–976 (1954).
 35. Somlyo, A. P. & Somlyo, A. V. Vascular smooth muscle. I. normal structure, pathology, biochemistry, and biophysics. *Pharmacol. Rev.* **20**, 197–272 (1968).
 36. Boberg, L., Szekeres, F. L. M. & Arner, A. Signaling and metabolic properties of fast and slow smooth muscle types from mice. *Pflüger's Arch. - Eur. J. Physiol.* **470**, 681–691 (2018).
 37. Bárány, M. ATPase activity of myosin correlated with speed of muscle shortening. *J. Gen. Physiol.* **50**, 197–218 (1967).
 38. Kirber, M. T. *et al.* Multiple pathways responsible for the stretch-induced increase in Ca²⁺ concentration in toad stomach smooth muscle cells. *J. Physiol.* **524**, 3–17 (2000).
 39. Langton, P., Ward, S. M., Carl, A., Norell, M. A. & Sanders, K. M. Spontaneous electrical activity of interstitial cells of Cajal isolated from canine proximal colon. *Proc. Natl. Acad. Sci. U. S. A.* **86**, 7280–7284 (1989).
 40. Ward, S. M., Burns, A. J., Torihashi, S. & Sanders, K. M. Mutation of the proto-oncogene c-kit blocks development of interstitial cells and electrical rhythmicity in murine intestine. *J. Physiol.* **480**, 91–97 (1994).
 41. Gordon, A. M., Huxley, A. F. & Julian, F. J. The variation in isometric tension with sarcomere length in vertebrate muscle fibres. *J. Physiol.* **184**, 170–192 (1966).
 42. Herrera, A. M. *et al.* ‘Sarcomeres’ of smooth muscle: functional characteristics and ultrastructural evidence. *J. Cell Sci.* **118**, 2381–2392 (2005).
 43. Siegman, M. J., Davidheiser, S., Mooers, S. U. & Butler, T. M. Structural limits on force production and shortening of smooth muscle. *J. Muscle Res. Cell Motil.* **34**, 43–60 (2013).
 44. Tomalka, A., Borsdorf, M., Böl, M. & Siebert, T. Porcine stomach smooth muscle force depends on history-effects. *Front. Physiol.* **8**, 802 (2017).
 45. Gunst, S. J., Meiss, R. a, Wu, M. F. & Rowe, M. Mechanisms for the mechanical plasticity of tracheal smooth muscle. *Am. J. Physiol.* **268**, C1267–C1276 (1995).
 46. Chen, C. *et al.* Fluidization and resolidification of the human bladder smooth muscle cell

- in response to transient stretch. *PLoS One* **5**, e12035. (2010).
47. Chitano, P. *et al.* Smooth muscle function and myosin polymerization. *J. Cell Sci.* **130**, 2468–2480 (2017).
 48. Wang, L., Pare, P. D. & Seow, C. Y. Plasticity in skeletal, cardiac, and smooth muscle selected contribution: effect of chronic passive length change on airway smooth muscle length-tension relationship. *J. Appl. Physiol.* **90**, 734–740 (2001).
 49. Hill, A. V. The heat of shortening and the dynamic constants of muscle. *Proc. R. Soc. B Biol. Sci.* **126**, 136–195 (1938).
 50. Till, O., Siebert, T., Rode, C. & Blickhan, R. Characterization of isovelocity extension of activated muscle: a Hill-type model for eccentric contractions and a method for parameter determination. *J. Theor. Biol.* **255**, 176–187 (2008).
 51. Schubert, M. L. Gastric acid secretion. *Curr. Opin. Gastroenterol.* **32**, 452–460 (2016).
 52. Feher, J. *Quantitative human physiology: an introduction.* (Elsevier, 2017).
 53. Cohen, S., Long, W. B. & Snape, W. J. Gastrointestinal motility. *Int. Rev. Physiol.* **19**, 107–149 (1979).
 54. Ahluwalia, N. K., Thompson, D. G., Barlow, J., Troncon, L. E. A. & Hollis, S. Relaxation responses of the human proximal stomach to distension during fasting and after food. *Am. J. Physiol.* **267**, G166–G172 (1994).
 55. Sanders, K. M., Ward, S. M. & Koh, S. D. Interstitial cells: regulators of smooth muscle function. *Physiol. Rev.* **94**, 859–907 (2014).
 56. Fry, C. H. & Vahabi, B. The role of the mucosa in normal and abnormal bladder function. *Physiol. Behav. Clin Pharmacol Toxicol* **119**, 57–62 (2016).
 57. Hubert, J., Wang, X., Wehrli, E., Hauri, D. & Maake, C. Evidence of gap junctions in stable nonobstructed human bladder. *J. Urol.* **169**, 745–749 (2003).
 58. Brading, A. F., Teramoto, N., Dass, N. & McCoy, R. Morphological and physiological characteristics of urethral circular and longitudinal smooth muscle. *Scand. J. Urol. Nephrol. Suppl.* **35**, 12–18 (2001).
 59. Vaughan, C. W. & Satchell, P. M. Urine storage mechanisms. *Prog. Neurobiol.* **46**, 215–237 (1995).
 60. Morrison, J. Physiological society symposium on the physiology and pathophysiology of the lower urinary tract: the activation of bladder wall afferent nerves. *Exp. Physiol.* **84**, 131–136 (1999).
 61. Tortora, G. J. *Principles of Anatomy and Physiology.* (John Wiley & Sons, 2016).
 62. Sarnelli, G., Vos, R., Cuomo, R., Janssens, J. & Tack, J. Reproducibility of gastric barostat studies in healthy controls and in dyspeptic patients. *Am. J. Gastroenterol.* **96**,

- 1047–1053 (2001).
63. Whitehead, W. E. *et al.* Standardization of barostat procedures for testing smooth muscle tone and sensory thresholds in the gastrointestinal tract. *Dig. Dis. Sci.* **42**, 223–241 (1997).
 64. Wang, C. C. *et al.* Diabetes induced alternations in the biomechanical properties of the urinary bladder wall in rats. *Urology* **73**, 911–915 (2009).
 65. Damaser, M. S. Whole bladder mechanics during filling. *Scand. J. Urol. Nephrol.* **33**, 51–58 (1999).
 66. Abarbanel, J. & Marcus, E. L. Impaired detrusor contractility in community-dwelling elderly presenting with lower urinary tract symptoms. *Urology* **69**, 436–440 (2007).
 67. Miyazato, M., Yoshimura, N. & Chancellor, M. B. The other bladder syndrome: underactive bladder. *Rev. Urol.* **15**, 11–22 (2013).
 68. Tomalka, A., Weidner, S., Hahn, D., Seiberl, W. & Siebert, T. Cross-bridges and sarcomeric non-cross-bridge structures contribute to increased work in stretch-shortening cycles. *Front. Physiol.* **11**, 921 (2020).
 69. Tomalka, A. *et al.* Extensive eccentric contractions in intact cardiac trabeculae: revealing compelling differences in contractile behaviour compared to skeletal muscles. *Proc. R. Soc. B Biol. Sci.* **286**, 20190719 (2019).
 70. Korossis, S., Bolland, F., Southgate, J., Ingham, E. & Fisher, J. Regional biomechanical and histological characterisation of the passive porcine urinary bladder: implications for augmentation and tissue engineering strategies. *Biomaterials* **30**, 266–275 (2009).
 71. Rezakhaniha, R. *et al.* Experimental investigation of collagen waviness and orientation in the arterial adventitia using confocal laser scanning microscopy. *Biomech. Model. Mechanobiol.* **11**, 461–473 (2012).
 72. Longhurst, P. A., Kang, J., Wein, A. J. & Levin, R. M. Comparative length-tension relationship of urinary bladder strips from hamsters, rats, guinea-pigs, rabbits and cats. *Pharmacology* **96A**, 221–225 (1990).
 73. Minekus, J. & van Mastrigt, R. Length dependence of the contractility of pig detrusor smooth muscle fibres. *Urol. Res.* **29**, 126–133 (2001).
 74. Speich, J. E. *et al.* Adjustable passive length-tension curve in rabbit detrusor smooth muscle. *J. Appl. Physiol.* **102**, 1746–55 (2007).
 75. Seydewitz, R., Menzel, R., Siebert, T. & Böl, M. Three-dimensional mechano-electrochemical model for smooth muscle contraction of the urinary bladder. *J. Mech. Behav. Biomed. Mater.* **75**, 128–146 (2017).
 76. Menzel, R., Böl, M. & Siebert, T. Importance of contraction history on muscle force of porcine urinary bladder smooth muscle. *Int. Urol. Nephrol.* **49**, 205–214 (2017).
 77. Trostorf, R., Morales-Orcajo, E., Siebert, T. & Böl, M. Location- and layer-dependent

- biomechanical and microstructural characterisation of the porcine urinary bladder wall. *J. Mech. Behav. Biomed. Mater.* **115**, 104275 (2021).
78. Gilbert, T. W. *et al.* Collagen fiber alignment and biaxial mechanical behavior of porcine urinary bladder derived extracellular matrix. *Biomaterials* **29**, 4775–4782 (2008).
 79. Zanetti, E. M., Perrini, M., Bignardi, C. & Audenino, A. L. Bladder tissue passive response to monotonic and cyclic loading. *Biorheology* **49**, 49–63 (2012).
 80. Natali, A. N. *et al.* Bladder tissue biomechanical behavior: experimental tests and constitutive formulation. *J. Biomech.* **48**, 3088–3096 (2015).
 81. Chantereau, P. *et al.* Mechanical properties of pelvic soft tissue of young women and impact of aging. *Int. Urogynecol. J.* **25**, 1547–1553 (2014).
 82. Cheng, F. *et al.* Layer-dependent role of collagen recruitment during loading of the rat bladder wall. *Biomech. Model. Mechanobiol.* **17**, 403–417 (2018).
 83. Gloeckner, D. C. *et al.* Passive biaxial mechanical properties of the rat bladder wall after spinal cord injury. *J. Urol.* **167**, 2247–2252 (2002).
 84. Nagatomi, J., Gloeckner, D. C., Chancellor, M. B., De Groat, W. C. & Sacks, M. S. Changes in the biaxial viscoelastic response of the urinary bladder following spinal cord injury. *Ann. Biomed. Eng.* **32**, 1409–1419 (2004).
 85. Uvelius, B. Isometric and isotonic length-tension relations and variations in cell length in longitudinal smooth muscle from rabbit urinary bladder. *Acta Physiol. Scand.* **97**, 1–12 (1976).
 86. Uvelius, B. Influence of muscle length on the force-velocity relation of K⁺-contractures in smooth muscle from rabbit urinary bladder. *Acta Physiol. Scand.* **101**, 270–277 (1977).
 87. Uvelius, B. Shortening velocity, active force and homogeneity of contraction during electrically evoked twitches in smooth muscle from rabbit urinary bladder. *Acta Physiol. Scand.* **106**, 481–486 (1979).
 88. Uvelius, B. Length-tension relations of in vitro urinary bladder smooth muscle strips. *J. Pharmacol. Toxicol. Methods* **45**, 87–90 (2001).
 89. Griffiths, D. J., van Mastrigt, R., van Duyl, W. A. & Coolsaet, B. L. R. A. Active mechanical properties of the smooth muscle of the urinary bladder. *Med. Biol. Eng. Comput.* **17**, 281–290 (1979).
 90. van Mastrigt, R. The length dependence of the series elasticity of pig bladder smooth muscle. *J. Muscle Res. Cell Motil.* **9**, 525–532 (1988).
 91. Huntington, A., Abramowitch, S. D., Moalli, P. A. & De Vita, R. Strains induced in the vagina by smooth muscle contractions. *Acta Biomater.* **129**, 178–187 (2021).
 92. Ulrich, D. *et al.* Regional variation in tissue composition and biomechanical properties of postmenopausal ovine and human vagina. *PLoS One* **9**, e104972 (2014).

93. Aydin, R. C. *et al.* Experimental characterization of the biaxial mechanical properties of porcine gastric tissue. *J. Mech. Behav. Biomed. Mater.* **74**, 499–506 (2017).
94. Jia, Z. G., Li, W. & Zhou, Z. R. Mechanical characterization of stomach tissue under uniaxial tensile action. *J. Biomech.* **48**, 651–658 (2015).
95. Zhao, J., Liao, D., Chen, P., Kunwald, P. & Gregersen, H. Stomach stress and strain depend on location, direction and the layered structure. *J. Biomech.* **41**, 3441–3447 (2008).
96. Zhao, J., Liao, D. & Gregersen, H. Tension and stress in the rat and rabbit stomach are location- and direction-dependent. *Neurogastroenterol. Motil.* **17**, 388–398 (2005).
97. Gabella, G. & Uvelius, B. Urinary bladder of rat: fine structure of normal and hypertrophic musculature. *Cell Tissue Res.* **262**, 67–79 (1990).
98. Gilbert, T. W. *et al.* Collagen fiber alignment and biaxial mechanical behavior of porcine urinary bladder derived extracellular matrix. *Biomaterials* **29**, 4775–4782 (2008).
99. Longhurst, P. A., Leggett, R. E. & Briscoe, J. A. K. Influence of strip size and location on contractile responses of rat urinary bladder body strips. *Gen. Pharmacol.* **26**, 1519–1527 (1995).
100. Vila Pouca, M. C. P. *et al.* Simulation of the uterine contractions and foetus expulsion using a chemo-mechanical constitutive model. *Biomech. Model. Mechanobiol.* **18**, 829–843 (2019).
101. O’Grady, G. *et al.* Origin and propagation of human gastric slow-wave activity defined by high-resolution mapping. *Am. J. Physiol.* **299**, G585–G592 (2010).
102. Egbuji, J. U. *et al.* Origin, propagation and regional characteristics of porcine gastric slow wave activity determined by high-resolution mapping. *Neurogastroenerol. Motil.* **22**, e292–e300 (2010).
103. Sathar, S., Trew, M. L., O’Grady, G. & Cheng, L. K. A multiscale tridomain model for simulating bioelectric gastric pacing. *IEEE Trans. Biomed. Eng.* **62**, 2685–2692 (2015).
104. Lammers, W. J. E. P., Ver Donck, L., Stephen, B., Smets, D. & Schuurkes, J. A. J. Origin and propagation of the slow wave in the canine stomach: The outlines of a gastric conduction system. *Am. J. Physiol.* **296**, G1200–G1210 (2009).
105. Buist, M. L., Corrias, A. & Poh, Y. C. A model of slow wave propagation and entrainment along the stomach. *Ann. Biomed. Eng.* **38**, 3022–3030 (2010).
106. Cheng, L. K., Komuro, R., Austin, T. M., Buist, M. L. & Pullan, A. J. Anatomically realistic multiscale models of normal and abnormal gastrointestinal electrical activity. *World J. Gastroenterol.* **13**, 1378–1383 (2007).
107. Corrias, A., Pathmanathan, P., Gavaghan, D. J. & Buist, M. L. Modelling tissue electrophysiology with multiple cell types: Applications of the extended bidomain

- framework. *Integr. Biol.* **4**, 192–201 (2012).
108. Du, P., O’Grady, G., Davidson, J. B., Cheng, L. K. & Pullan, A. J. Multiscale modeling of gastrointestinal electrophysiology and experimental validation. *Crit. Rev. Biomed. Eng.* **38**, 225–254 (2010).
 109. Du, P., O’Grady, G., Cheng, L. K. & Pullan, A. J. A multiscale model of the electrophysiological basis of the human electrogastrogram. *Biophys. J.* **99**, 2784–2792 (2010).
 110. Du, P., O’Grady, G., Gao, J., Sathar, S. & Cheng, L. K. Toward the virtual stomach: progress in multiscale modeling of gastric electrophysiology and motility. *Wiley Interdiscip. Rev. Syst. Biol. Med.* **5**, 481–493 (2013).
 111. Pullan, A., Cheng, L., Yassi, R. & Buist, M. Modelling gastrointestinal bioelectric activity. *Prog. Biophys. Mol. Biol.* **85**, 523–550 (2004).
 112. Pal, A., Brasseur, J. G. & Abrahamsson, B. A stomach road or ‘Magenstrasse’ for gastric emptying. *J. Biomech.* **40**, 1202–1210 (2007).
 113. Pal, A. *et al.* Gastric flow and mixing studied using computer simulation. *Proc. Biol. Sci.* **271**, 2587–94 (2004).
 114. Ferrua, M. J. & Singh, R. P. Modeling the fluid dynamics in a human stomach to gain insight of food digestion. *J. Food Sci.* **75**, 151–162 (2010).
 115. Xue, Z., Ferrua, M. J. & Singh, R. P. Computational fluid dynamics modeling of granular flow in human stomach. *Rev. Aliment. Hoy* **21**, 3–14 (2012).
 116. Miftahof, R. N. *Biomechanics of the human stomach*. (Springer, 2017).
 117. Akhmadeev, N. R. & Miftahof, R. Stress-strain distribution in the human stomach. *Int. J. Des. Nat. Ecodynamics* **5**, 90–107 (2010).
 118. Huijing, P. A. & Baan, G. C. Myofascial force transmission: muscle relative position and length determine agonist and synergist muscle force. *J. Appl. Physiol.* **94**, 1092–1107 (2003).
 119. Yucesoy, C. A. Epimuscular myofascial force transmission implies novel principles for muscular mechanics. *Exerc. Sport Sci. Rev.* **38**, 128–134 (2010).
 120. Greenwell, T. J., Venn, S. N. & Mundy, A. R. Augmentation cystoplasty. *BJU Int.* **88**, 511–525 (2001).
 121. Gerharz, E. W., Turner, W. H., Kälble, T. & Woodhouse, C. R. J. Metabolic and functional consequences of urinary reconstruction with bowel. *BJU Int.* **91**, 143–149 (2003).
 122. Madersbacher, S. & Marberger, M. Is transurethral resection of the prostate still justified? *BJU Int.* **83**, 227–237 (1999).

123. Ahyai, S. A. *et al.* Meta-analysis of functional outcomes and complications following transurethral procedures for lower urinary tract symptoms resulting from benign prostatic enlargement. *Eur. Urol.* **58**, 384–397 (2010).
124. Cheng, L. K. *et al.* Gastrointestinal system. *Wiley Interdiscip. Rev. Syst. Biol. Med.* **2**, 65–79 (2010).
125. van Mastrigt, R. & Glerum, J. J. Electrical stimulation of smooth muscle strips from the urinary bladder of the pig. *J. Biomed. Eng.* **7**, 2–8 (1985).
126. Siebert, T., Stutzig, N. & Rode, C. A hill-type muscle model expansion accounting for effects of varying transverse muscle load. *J. Biomech.* **66**, 57–62 (2017).
127. Brenner, B. Technique for stabilizing the striation pattern in maximally calcium-activated skinned rabbit psoas fibers. *Biophys. J.* **41**, 99–102 (1983).
128. Cohen, J. *Statistical power analysis for the behavioral sciences.* (Lawrence Erlbaum Associates, 1988).
129. Ali, M. H. M., Amin, W., Nasr El-Din, M. S. & Abdel-Hamid, G. A. Role of tibolone and cimicifuga racemosa on urinary bladder alterations in surgically ovariectomized adult female rats. *Egypt. J. Anat.* **38**, 1–24 (2015).
130. Sellers, D., Chess-Williams, R. & Michel, M. C. Modulation of lower urinary tract smooth muscle contraction and relaxation by the urothelium. *Naunyn. Schmiedebergs. Arch. Pharmacol.* **391**, 675–694 (2018).
131. Levin, R. M., Wein, A. J., Krasnopolsky, L., Atta, M. A. & Ghoniem, G. M. Effect of Mucosal Removal on the Response of the Feline Bladder to Pharmacological Stimulation. *J. Urol.* **153**, 1291–1294 (1995).
132. Propping, S. *et al.* Mucosa of human detrusor impairs contraction and β -adrenoceptor-mediated relaxation. *BJU Int.* **112**, 1215–1222 (2013).
133. Chaiyaprasithi, B., Mang, C. F., Kilbinger, H. & Hohenfellner, M. Inhibition of human detrusor contraction by a urothelium derived factor. *J. Urol.* **170**, 1897–1900 (2003).
134. Maggi, C. A. *et al.* The presence of mucosa reduces the contractile response of the guinea-pig urinary bladder to substance P. *J. Pharm. Pharmacol.* **39**, 653–655 (1987).
135. Koşan, M. *et al.* Effect of urothelium on bladder contractility in diabetic rats. *Int. J. Urol.* **12**, 677–682 (2005).
136. Mashima, H., Okada, T. & Okuyama, H. Dynamics of contraction in the guinea pig taenia coli. *Jpn. J. Physiol.* **29**, 85–98 (1979).
137. Moriya, M. & Miyazaki, E. The differences in contractile response of AC field stimulation between longitudinal and circular muscles of guinea pig stomach. *Jpn. J. Physiol.* **32**, 1–12 (1982).
138. Malmqvist, U., Arner, A. & Uvelius, B. Mechanics and Ca²⁺-sensitivity of human

- detrusor muscle bundles studied in vitro. *Acta Physiol. Scand.* **143**, 373–380 (1991).
139. Stephens, N. L. Force-velocity constants in smooth muscle: afterload isotonic and quick-release methods. *Can. J. Physiol. Pharmacol.* **63**, 48–51 (1985).
 140. Mulvany, M. J. & Warshaw, D. M. The active tension-length curve of vascular smooth muscle related to its cellular components. *J. Gen. Physiol.* **74**, 85–104 (1979).
 141. Gordon, A. R. & Siegman, M. J. Mechanical properties of smooth muscle. I. Length-tension and force-velocity relations. *Am. J. Physiol.* **221**, 1243–1249 (1971).
 142. Stephens, N. L., Kroeger, E. & Mehta, J. A. Force-velocity characteristics of respiratory airway smooth muscle. *J. Appl. Physiol.* **26**, 685–692 (1969).
 143. Moriya, M. & Miyazaki, E. Force-velocity characteristics of stomach muscle: a comparison between longitudinal and circular muscle strips. *Comp. Biochem. Physiol.* **81A**, 531–537 (1985).
 144. Siebert, T. *et al.* Three-dimensional muscle architecture and comprehensive dynamic properties of rabbit gastrocnemius, plantaris and soleus: input for simulation studies. *PLoS One* **10**, e0130985 (2015).
 145. Pel, J. J. M., van Asselt, E. & van Mastrigt, R. Contractile properties of the proximal urethra and bladder in female pig: morphology and function. *Neurourol. Urodyn.* **25**, 70–77 (2006).
 146. Pel, J. J. M., van Asselt, E. & van Mastrigt, R. Contractile properties of inner and outer smooth muscle bundles from pig urinary detrusor. *Urol. Res.* **33**, 23–30 (2005).
 147. Gong, M. C. *et al.* Myosin light chain phosphatase activities and the effects of phosphatase inhibitors in tonic and phasic smooth muscle. *J. Biol. Chem.* **267**, 14662–14668 (1992).
 148. Horiuti, K., Somlyo, A. V, Goldman, Y. E. & Somlyo, A. P. Kinetics of contraction initiated by flash photolysis of caged adenosine triphosphate in tonic and phasic smooth muscles. *J. Gen. Physiol.* **94**, 769–781 (1989).
 149. Hypolite, J. A. *et al.* Regional variation in myosin isoforms and phosphorylation at the resting tone in urinary bladder smooth muscle. *Am. J. Physiol. Cell Physiol.* **280**, C254–64 (2001).
 150. Kong, F. & Singh, R. P. Disintegration of solid foods in human stomach. *J. Food Sci.* **73**, 67–80 (2008).
 151. Liao, D., Zhao, J. & Gregersen, H. A novel 3D shape context method based strain analysis on a rat stomach model. *J. Biomech.* **45**, 1566–1573 (2012).
 152. El-Serag, H. B. Time trends of gastroesophageal reflux disease: a systematic review. *Clin. Gastroenterol. Hepatol.* **5**, 17–26 (2007).
 153. Gawron, A. J., French, D. D., Pandolfino, J. E. & Howden, C. W. Economic evaluations

- of gastroesophageal reflux disease medical management. *Pharmacoeconomics* **32**, 745–758 (2014).
154. Hunt, R. H. *et al.* The stomach in health and disease. *Gut* **64**, 1650–1668 (2015).
 155. Masaoka, T. & Tack, J. Gastroparesis: current concepts and management. *Gut Liver* **3**, 166–173 (2009).
 156. Oustamanolakis, P. & Tack, J. Dyspepsia: organic versus functional. *J. Clin. Gastroenterol.* **46**, 175–190 (2012).
 157. Soffer, E. E. Gastric electrical stimulation for gastroparesis. *J. Neurogastroenterol. Motil.* **18**, 131–137 (2012).
 158. Azpiroz, F. & Malagelada, J. R. Physiological variations in canine gastric tone measured by an electronic barostat. *Am. J. Physiol.* **11**, G229–G237 (1985).
 159. Notivol, R. *et al.* Gastric tone determines the sensitivity of the stomach to distention. *Gastroenterology* **108**, 330–336 (1995).
 160. Azpiroz, F. & Malagelada, J. R. Importance of vagal input in maintaining gastric tone in the dog. *J. Physiol.* **384**, 511–524 (1987).
 161. Carniel, E. L. *et al.* A biomechanical approach to the analysis of methods and procedures of bariatric surgery. *J. Biomech.* **56**, 32–41 (2017).
 162. Gregersen, H. *et al.* Mechanical properties in the human gastric antrum using B-mode ultrasonography and antral distension. *Am. J. Physiol.* **283**, G368–G375 (2002).
 163. Liao, D., Zhao, J. & Gregersen, H. Regional surface geometry of the rat stomach based on three-dimensional curvature analysis. *Phys. Med. Biol.* **50**, 231–246 (2005).
 164. Penning, C., Vu, M. K., Delemarre, J. B. V. M. & Masclee, A. A. M. Proximal gastric motor and sensory function in slow transit constipation. *Scand. J. Gastroenterol.* **36**, 1267–1273 (1998).
 165. Schulze-Delrieu, K., Herman, R. J., Shirazi, S. S. & Brown, B. P. Contractions move contents by changing the configuration of the isolated cat stomach. *Am. J. Physiol.* **274**, G359–G369 (1998).
 166. Egorov, V. I., Schastlivtsev, I. V., Prut, E. V., Baranov, A. O. & Turusov, R. A. Mechanical properties of the human gastrointestinal tract. *J. Biomech.* **35**, 1417–1425 (2002).
 167. Rosen, J., Brown, J. D., De, S., Sinanan, M. & Hannaford, B. Biomechanical properties of abdominal organs in vivo and postmortem under compression loads. *J. Biomech. Eng.* **130**, 1–17 (2008).
 168. Du, P. *et al.* Effects of electrical stimulation on isolated rodent gastric smooth muscle cells evaluated via a joint computational simulation and experimental approach. *Am. J. Physiol.* **297**, G672–G680 (2009).

169. Ganitkevich, V. & Isenberg, G. Isolated guinea pig coronary smooth muscle cells, acetylcholine induces hyperpolarization due to sarcoplasmic reticulum calcium release activating potassium channels. *Circ. Res.* **67**, 525–528 (1990).
170. Yagi, S., Becker, P. L. & Fay, F. S. Relationship between force and Ca²⁺ concentration in smooth muscle as revealed by measurements on single cells. *Proc. Natl. Acad. Sci. U. S. A.* **85**, 4109–4113 (1988).
171. Batista-Lima, F. J. *et al.* A simple laboratory exercise with rat isolated esophagus and stomach fundus to reveal functional differences between striated and smooth muscle cells. *Adv. Physiol. Educ.* **41**, 291–297 (2017).
172. Daniel, E. E. & Sarna, S. K. Distribution of excitatory vagal fibers in canine gastric wall to control motility. *Gastroenterology* **71**, 608–613 (1976).
173. Milenov, K. & Golenhofen, K. Contractile responses of longitudinal and circular smooth muscle of the canine stomach to prostaglandin E and F₂Alpha. *Prostaglandins Leukot. Med.* **8**, 287–300 (1982).
174. Squecco, R., Garella, R., Francini, F. & Baccari, M. C. Influence of obestatin on the gastric longitudinal smooth muscle from mice: mechanical and electrophysiological studies. *Am. J. Physiol. Gastrointest. Liver Physiol.* **305**, G628-37 (2013).
175. Vogalis, F., Ward, S. M. & Sanders, K. M. Correlation between electrical and morphological properties of canine pyloric circular muscle. *Am. J. Physiol.* **260**, G390–G398 (1991).
176. Szurszewski, J. H. Mechanism of action of pentagastrin and acetylcholine on the longitudinal muscle of the canine antrum. *J. Physiol.* **252**, 335–361 (1975).
177. Zagorodnyuk, V. P., Chen, B. N. & Brookes, S. J. H. Intraganglionic laminar endings are mechano-transduction sites of vagal tension receptors in the guinea-pig stomach. *J. Physiol.* **534**, 255–268 (2001).
178. Paton, W. D. M. & Vane, J. R. An analysis of the responses of the isolated stomach to electrical stimulation and to drugs. *J. Physiol.* **165**, 10–46 (1963).
179. Armitage, A. K. & Dean, A. C. B. The effects of pressure and pharmacologically active substances on gastric peristalsis in a transmurally stimulated rat stomach-duodenum preparation. *J. Physiol.* **182**, 42–56 (1966).
180. Weisbrodt, N. W., Wiley, J. N., Overholt, B. F. & Bass, P. A relation between gastroduodenal muscle contractions and gastric emptying. *Gut* **10**, 543–8 (1969).
181. Geliebter, A. & Hashim, S. A. Gastric capacity in normal, obese, and bulimic women. *Physiol. Behav.* **74**, 743–746 (2001).
182. Schulze-Delrieu, K. & Shirazi, S. S. Pressure and length adaptations in isolated cat stomach. *Am. J. Physiol.* **252**, G92–G99 (1987).

183. Kelly, K. A. & Code, C. F. Canine gastric pacemaker. *Am. J. Physiol.* **220**, 112–118 (1971).
184. Kelly, K. A. & La Force, R. C. Pacing the canine stomach with electric stimulation. *Am. J. Physiol.* **222**, 588–594 (1972).
185. Azpiroz, F. & Malagelada, J. R. Gastric tone measured by an electronic barostat in health and postsurgical gastroparesis. *Gastroenterology* **92**, 934–943 (1987).
186. Paterson, C. A., Anvari, M., Tougas, G. & Huizinga, J. D. Nitrenergic and cholinergic vagal pathways involved in the regulation of canine proximal gastric tone: an in vivo study. *Neurogastroenterol. Motil.* **12**, 301–306 (2000).
187. Schwizer, W. *et al.* Noninvasive measurement of gastric accommodation in humans. *Gut* **51**, 59.62 (2002).
188. Poh, Y. C., Beyder, A., Strege, P. R., Farrugia, G. & Buist, M. L. Quantification of gastrointestinal sodium channelopathy. *J. Theor. Biol.* **293**, 41–48 (2012).
189. Sathar, S., Trew, M. L., Du, P., O’grady, G. & Cheng, L. K. A biophysically based finite-state machine model for analyzing gastric experimental entrainment and pacing recordings. *Ann. Biomed. Eng.* **42**, 858–870 (2014).
190. Yeoh, J. W., Corrias, A. & Buist, M. L. A mechanistic model of a PDGFR α + cell. *J. Theor. Biol.* **408**, 127–136 (2016).
191. Buist, M. L., Cheng, L. K., Sanders, K. M. & Pullan, A. J. Multiscale modelling of human gastric electric activity: can the electrogastrogram detect functional electrical uncoupling? *Exp. Physiol.* **91**, 383–390 (2006).
192. Corrias, A. & Buist, M. L. A quantitative model of gastric smooth muscle cellular activation. *Ann. Biomed. Eng.* **35**, 1595–1607 (2007).
193. Corrias, A. & Buist, M. L. Quantitative cellular description of gastric slow wave activity. *Am. J. Physiol.* **294**, G989–G995 (2008).
194. Du, P., Gao, J., O’Grady, G. & Cheng, L. K. A simplified biophysical cell model for gastric slow wave entrainment simulation. in *IEEE Engineering in Medicine and Biology Society. Annual Conference* **35**, 6547–6550 (2013).
195. Edwards, F. R. & Hirst, G. D. S. An electrical analysis of slow wave propagation in the guinea-pig gastric antrum. *J. Physiol.* **571**, 179–189 (2006).
196. Gajendiran, V. & Buist, M. L. A quantitative description of active force generation in gastrointestinal smooth muscle. *Int. j. numer. method. biomed. eng.* **27**, 450–460 (2011).
197. Hirst, G. D. S. & Edwards, F. R. Electrical events underlying organized myogenic contractions of the guinea pig stomach. *J. Physiol.* **576**, 659–665 (2006).
198. Hirst, G. D. S., Garcia-Londoño, A. P. & Edwards, F. R. Propagation of slow waves in the guinea-pig gastric antrum. *J. Physiol.* **571**, 165–177 (2006).

199. Panfilov, A. V., Keldermann, R. H. & Nash, M. P. Self-organized pacemakers in a coupled reaction-diffusion-mechanics system. *Phys. Rev. Lett.* **95**, 5–8 (2005).
200. Cherubini, C., Filippi, S. & Gizzi, A. Electroelastic unpinning of rotating vortices in biological excitable media. *Phys. Rev. E - Stat. Nonlinear, Soft Matter Phys.* **85**, 1–8 (2012).
201. Göktepe, S. & Kuhl, E. Electromechanics of the heart: A unified approach to the strongly coupled excitation-contraction problem. *Comput. Mech.* **45**, 227–243 (2010).
202. Ambrosi, D. & Pezzuto, S. Active stress vs. active strain in mechanobiology: constitutive issues. *J. Elast.* **107**, 199–212 (2012).
203. Giancesio, G., Musesti, A. & Riccobelli, D. A comparison between active strain and active stress in transversely isotropic hyperelastic materials. *J. Elast.* **137**, 63–82 (2019).
204. Brandstaeter, S. *et al.* Computational model of gastric motility with active-strain electromechanics. *ZAMM Zeitschrift für Angew. Math. und Mech.* **98**, 2177–2197 (2018).
205. Cheng, L. K. *et al.* A model of the electrical activity of the stomach: from cell to body surface. in *AIEEE Engineering in Medicine and Biology Society. Annual Conference* **3**, 2761–2764 (2003).
206. Du, P. *et al.* Progress in mathematical modeling of gastrointestinal slow wave abnormalities. *Front. Physiol.* **8**, (2018).
207. Wenzel, V. *et al.* Respiratory system compliance decreases after cardiopulmonary resuscitation and stomach inflation: Impact of large and small tidal volumes on calculated peak airway pressure. *Resuscitation* **38**, 113–118 (1998).
208. Wilson, R. L. & Stevenson, C. E. Anatomy and physiology of the stomach. in *Shackelford's Surgery of the Alimentary Tract, 2 Volume Set* (ed. Yeo, C. J.) 634–646 (Elsevier, 2019).
209. Schulze, K. Imaging and modelling of digestion in the stomach and the duodenum. *Neurogastroenterol. Motil.* **18**, 172–183 (2006).
210. Hertz, A. F. The motor functions of the stomach. *Qjm* **os3**, 373–394 (1910).
211. Guyton, A. C. *Textbook of medical physiology*. (Elsevier, 2006).
212. Tack, J., Caenepeel, P., Piessevaux, H., Cuomo, R. & Janssens, J. Assessment of meal induced gastric accommodation by a satiety drinking test in health and in severe functional dyspepsia. *Gut* **52**, 1271–1277 (2003).
213. Azpiroz, F. Control of gastric emptying by gastric tone. *Dig. Dis. Sci.* **39**, 18–19 (1994).
214. Cannon, W. B. The movements of the stomach, studied by means of the Röntgen rays. *J. Bost. Soc. Med. Sci.* **2**, 59–66 (1898).
215. Kwiatek, M. A. *et al.* Quantification of distal antral contractile motility in healthy human

- stomach with magnetic resonance imaging. *J. Magn. Reson. Imaging* **24**, 1101–1109 (2006).
216. Sanders, K. M., Koh, S. D. & Ward, S. M. Interstitial cells of Cajal as pacemakers in the gastrointestinal tract. *Annu. Rev. Physiol.* **68**, 307–343 (2006).
217. Kraichely, R. E. & Farrugia, G. Mechanosensitive ion channels in interstitial cells of Cajal and smooth muscle of the gastrointestinal tract. *Neurogastroenterol. Motil.* **19**, 245–252 (2007).
218. Angeli, T. R., O’Grady, G. & Lammers, W. J. E. P. The electrical regulation of GI motility at the whole-organ level. in *New Advances in Gastrointestinal Motility Research* (eds. Cheng, L. K., Farrugia, A. J. & Pullan, A. J.) 95–112 (Springer, 2013).
219. Cheng, L. K., Du, P. & O’Grady, G. Mapping and modeling gastrointestinal bioelectricity: from engineering bench to bedside. *Physiology* **28**, 310–317 (2013).
220. Hocke, M. *et al.* Every slow-wave impulse is associated with motor activity of the human stomach. *Am. J. Physiol.* **296**, G709–G716 (2009).
221. Xu, W. X. *et al.* Effect of stretch on calcium channel currents recorded from the antral circular myocytes of guinea pig stomach. *Pflüger’s Arch. - Eur. J. Physiol.* **432**, 159–164 (1996).
222. Won, K. J., Sanders, K. M. & Ward, S. M. Interstitial cells of Cajal mediate mechanosensitive responses in the stomach. *Proc. Natl. Acad. Sci. U. S. A.* **102**, 14913–14918 (2005).
223. Huizinga, J. D. & Lammers, W. J. E. P. Gut peristalsis is governed by a multitude of cooperating mechanisms. *Am. J. Physiol.* **296**, G1–G8 (2009).
224. Johnson, L. *et al.* *Physiology of the gastrointestinal tract*. **1**, (Elsevier, 2012).
225. Hinder, R. A. & Kelly, K. A. Human gastric pacesetter potential. Site of origin, spread, and response to gastric transection and proximal gastric vagotomy. *Am. J. Surg.* **133**, 29–33 (1977).
226. Sanders, K. M. Regulation of smooth muscle excitation and contraction. *Neurogastroenterol. Motil.* **20**, 39–53 (2008).
227. Farrugia, G. Interstitial cells of Cajal in health and disease. *Neurogastroenterol. Motil.* **20**, 54–63 (2008).
228. Borsdorf, M. *et al.* Locational and directional dependencies of smooth muscle properties in pig urinary bladder. *Front. Physiol.* **10**, 63 (2019).
229. Altomare, A. *et al.* Experimental evidence and mathematical modeling of thermal effects on human colonic smooth muscle contractility. *Am. J. Physiol.* **307**, G77–G88 (2014).
230. Essig, D. A., Segal, S. S. & White, T. P. Skeletal muscle protein synthesis and degradation in vitro: effects of temperature. *Am J Physiol* **249**, C464–70 (1985).

231. Sarna, S. K., Daniel, E. E. & Kingma, Y. J. Simulation of the electric-control activity of the stomach by an array of relaxation oscillators. *Am. J. Dig. Dis.* **17**, 477 (1972).
232. Holzapfel, G. A. Biomechanics of soft tissue. in *Handbook of Material Behavior* (ed. Lemaitre, J.) 1049–1063 (Academic Press, 2001).
233. Böl, M. & Schmitz, A. A coupled chemomechanical model for smooth muscle contraction. in *Computer Models in Biomechanics* (eds. Holzapfel, G. A. & Kuhl, E.) 63–75 (Springer, 2013).
234. Böl, M., Schmitz, A., Nowak, G. & Siebert, T. A three-dimensional chemo-mechanical continuum model for smooth muscle contraction. *J. Mech. Behav. Biomed. Mater.* **13**, 215–229 (2012).
235. Schmitz, A. & Böl, M. On a phenomenological model for active smooth muscle contraction. *J. Biomech.* **44**, 2090–2095 (2011).
236. Aliev, R. R., Richards, W. & Wikswo, J. P. A simple nonlinear model of electrical activity in the intestine. *J. Theor. Biol.* **204**, 21–28 (2000).
237. Fukuta, H., Kito, Y. & Suzuki, H. Spontaneous electrical activity and associated changes in calcium concentration in guinea-pig gastric smooth muscle. *J. Physiol.* **540**, 249–260 (2002).
238. Vogalis, F., Publicover, N. G., Hume, J. R. & Sanders, K. M. Relationship between calcium current and cytosolic calcium in canine gastric smooth muscle cells. *Am. J. Physiol.* **260**, C1012–C1018 (1991).
239. Gilchrist, M. D., Murphy, J. G., Pierrat, B. & Saccomandi, G. Slight asymmetry in the winding angles of reinforcing collagen can cause large shear stresses in arteries and even induce buckling. *Meccanica* **52**, 3417–3429 (2017).
240. Böl, M. *et al.* Three-dimensional surface geometries of the rabbit soleus muscle during contraction: input for biomechanical modelling and its validation. *Biomech. Model. Mechanobiol.* **12**, 1205–1220 (2013).
241. Lin, A. S. H., Buist, M. L., Smith, N. P. & Pullan, A. J. Modelling slow wave activity in the small intestine. *J. Theor. Biol.* **242**, 356–362 (2006).
242. Wali, M. A. & Munnur, U. The patient with a full stomach. in *Benumhof and Hagberg's Airway Management* (ed. Hagberg, Carin, A.) 705–722 (Elsevier, 2013).
243. Leung, P. S. *The gastrointestinal system: gastrointestinal, nutritional and hepatobiliary physiology*. (Springer, 2014).
244. Morgan, K. G., Muir, T. C. & Szurszewski, J. H. The electrical basis for contraction and relaxation in canine fundal smooth muscle. *J. Physiol.* **311**, 475–488 (1981).
245. Golenhofen, K. & Mandrek, K. Phasic and tonic contraction processes in the gastrointestinal tract. *Dig. Dis.* **9**, 341–346 (1991).

246. Kasai, Y., Tsutsumi, O., Taketani, Y., Endo, M. & Iino, M. Stretch-induced enhancement of contractions in uterine smooth muscle of rats. *J. Physiol.* **486**, 373–384 (1995).
247. Kim, S. J. *et al.* Changes in intracellular Ca²⁺ concentration induced by L-type Ca²⁺ channel current in guinea pig gastric myocytes. *Am. J. Physiol.* **273**, C1947–C1956 (1997).
248. Ozaki, H., Gerthoffer, W. T., Publicover, N. G., Fusetani, N. & Sander, K. M. Time-dependent changes in Ca²⁺ sensitivity during phasic contraction of canine antral smooth muscle. *J. Physiol.* **440**, 207–224 (1991).
249. van Mastrigt, R. & Glerum, J. J. In vitro comparison of isometric and stop-test contractility parameters for the urinary bladder. *Urol. Res.* **13**, 11–17 (1985).
250. Geliebter, A. Gastric distension and gastric capacity in relation to food intake in humans. *Physiol. Behav.* **44**, 665–668 (1988).
251. Herzog, W., Kamal, S. & Clarke, H. D. Myofilament lengths of cat skeletal muscle: theoretical considerations and functional implications. *J. Biomech.* **25**, 945–948 (1992).
252. Jansson, G. Vago-vagal reflex relaxation of the stomach in the cat. *Acta Physiol. Scand.* **75**, 245–252 (1969).
253. Du, P. *et al.* Tissue-specific mathematical models of slow wave entrainment in wild-type and 5-HT_{2B} knockout mice with altered interstitial cells of Cajal networks. *Biophys. J.* **98**, 1772–1781 (2010).
254. Fontanella, C. G. *et al.* Computational models for the mechanical investigation of stomach tissues and structure. *Ann. Biomed. Eng.* **47**, 1237–1249 (2019).
255. Lin, Z. Y., McCallum, R. W., Schirmer, B. D. & Chen, J. D. Z. Effects of pacing parameters on entrainment of gastric slow waves in patients with gastroparesis. *Am. J. Physiol.* **274**, G186–G191 (1998).
256. O’Grady, G. *et al.* High-resolution spatial analysis of slow wave initiation and conduction in porcine gastric dysrhythmia. *Neurogastroenterol. Motil.* **23**, 345–355 (2011).
257. Stålhand, J. & Holzapfel, G. A. Length adaptation of smooth muscle contractile filaments in response to sustained activation. *J. Theor. Biol.* **397**, 13–21 (2016).
258. Klemm, L., Seydewitz, R., Borsdorf, M., Siebert, T. & Böl, M. On a coupled electro-chemomechanical model of gastric smooth muscle contraction. *Acta Biomater.* **109**, 163–181 (2020).
259. Sjuve, R., Haase, H., Morano, I., Uvelius, B. & Arner, A. Contraction kinetics and myosin isoform composition in smooth muscle from hypertrophied rat urinary bladder. *J. Cell. Biochem.* **63**, 86–93 (1996).
260. Arner, A. Mechanical characteristics of chemically skinned guinea-pig taenia coli. *Pflüger’s Arch. - Eur. J. Physiol.* **395**, 277–284 (1982).

261. Meiss, R. A. Some mechanical properties of cat intestinal muscle. *Am. J. Physiol.* **220**, 2000–2007 (1971).
262. Arner, A. & Hellstrand, P. Effects of calcium and substrate on force-velocity relation and energy turnover in skinned smooth muscle of the guinea-pig. *J. Physiol.* **360**, 347–365 (1985).
263. Lowy, J. & Mulvany, M. J. Mechanical properties of guinea pig taenia coli muscles. *Acta Physiol. Scand.* **88**, 123–136 (1973).
264. Muinuddin, A., Shuwen, X. U. E. & Diamant, N. E. Regional differences in the response of feline esophageal smooth muscle to stretch and cholinergic stimulation. *Am. J. Physiol.* **281**, G1460–G1467 (2001).
265. Tøttrup, A., Forman, A., Uldbjer, N., Funch-Jensen, P. & Andersson, K. E. Mechanical properties of isolated human esophageal smooth muscle. *Am. J. Physiol.* **258**, G338–G343 (1990).
266. Herlihy, J. T. & Murphy, R. a. Length-tension relationship of smooth muscle of the hog carotid artery. *Circ. Res.* **33**, 275–283 (1973).
267. Wingard, C. J., Browne, A. K. & Murphy, R. A. Dependence of force on length at constant cross-bridge phosphorylation in the swine carotid media. *J. Physiol.* **488**, 729–739 (1995).
268. Peiper, U., Laven, R. & Ehl, M. Force velocity relationships in vascular smooth muscle. The influence of temperature. *Pflüger's Arch. - Eur. J. Physiol.* **356**, 33–45 (1975).
269. Davis, M. J. & Davidson, J. Force-velocity relationship of myogenically active arterioles. *Am. J. Physiol.* **282**, H165–H174 (2002).
270. Davis, M. J. & Gore, R. W. Length-tension relationship of vascular smooth muscle in single arterioles. *Am. J. Physiol.* **256**, H630–H640 (1989).
271. Sarriá, R. *et al.* Morphometric study of the layers of the canine small intestine at five sampling sites. *Vet. J.* **192**, 498–502 (2012).
272. Arner, A., Mattiasson, A., Radzizewski, P. & Uvelius, B. Shortening velocity is different in longitudinal and circular muscle layers of the rabbit urethra. *Urol. Res.* **26**, 423–426 (1998).
273. Chen, Y., Wang, H., Li, H. & Liu, S. Long-pulse gastric electrical stimulation repairs interstitial cells of cajal and smooth muscle cells in the gastric antrum of diabetic rats. *Gastroenterol. Res. Pract.* 6309157 (2018).
274. Liu, L. W. C., Thuneberg, L. & Huizinga, J. D. Selective lesioning of interstitial cells of Cajal by methylene blue and light leads to loss of slow waves. *Am. J. Physiol.* **266**, G485–G496 (1994).
275. Sanders, K. M., Burke, E. P. & Stevens, R. J. Effects of methylene blue on rhythmic

- activity and membrane potential in the canine proximal colon. *Am. J. Physiol.* **256**, G779–G784 (1989).
276. Hintze, J. L. & Nelson, R. D. Violin plots: a box plot-density trace synergism. *Am. Stat.* **52**, 181–184 (1998).
277. Malmqvist, U. & Arner, A. Correlation between isoform composition of the 17 kDa myosin light chain and maximal shortening velocity in smooth muscle. *Pflüger's Arch. - Eur. J. Physiol.* **418**, 523–530 (1991).
278. Van Loocke, M., Lyons, C. G. & Simms, C. K. Viscoelastic properties of passive skeletal muscle in compression: stress-relaxation behaviour and constitutive modelling. *J. Biomech.* **41**, 1555–1566 (2008).
279. Thuneberg, L. Interstitial cells of cajal: intestinal pacemaker cells? *Adv. Anatomy, Embryol. Cell Biol.* **71**, 1–130 (1982).
280. Thuneberg, L., Johansen, V., Rumessen, J. J. & Andersen, B. G. Interstitial cells of cajal: selective uptake of methylene blue inhibits slow wave activity. in *Gastrointestinal Motility* (ed. Roman, C.) 495–502 (MTP Press, 1984).
281. Murphy, R. A., Herlihy, J. T. & Megerman, J. Force-generating capacity and contractile protein content of arterial smooth muscle. *J. Gen. Physiol.* **64**, 691–705 (1974).
282. May, M. *et al.* Post-void residual urine as a predictor of urinary tract infection — is there a cutoff value in asymptomatic men? *J. Urol.* **181**, 2540–2544 (2009).
283. Jokandan, M. S. *et al.* Bladder wall biomechanics: a comprehensive study on fresh porcine urinary bladder. *J. Mech. Behav. Biomed. Mater.* **79**, 92–103 (2018).
284. Martins, P. A. L. S. *et al.* Uniaxial mechanical behavior of the human female bladder. *Int. Urogynecol. J.* **22**, 991–995 (2011).
285. Davis, N. F. *et al.* Urinary bladder vs gastrointestinal tissue: a comparative study of their biomechanical properties for urinary tract reconstruction. *Urology* **113**, 235–240 (2018).
286. Flood, H. D. *et al.* Long-term results and complications using augmentation cystoplasty in reconstructive urology. *Neurourol. Urodyn.* **14**, 297–309 (1995).
287. Schaefer, M., Kaiser, A., Stehr, M. & Beyer, H. J. Bladder augmentation with small intestinal submucosa leads to unsatisfactory long-term results. *J. Pediatr. Urol.* **9**, 878–883 (2013).
288. Pokrywczynska, M., Adamowicz, J., Sharma, A. K. & Drewa, T. Human urinary bladder regeneration through tissue engineering - an analysis of 131 clinical cases. *Exp. Biol. Med.* **239**, 264–271 (2014).
289. Chua, M. E., Farhat, W. A., Ming, J. M. & McCammon, K. A. Review of clinical experience on biomaterials and tissue engineering of urinary bladder. *World J. Urol.* **38**, 2081–2093 (2020).

290. Purslow, P. P. Positional variations in fracture toughness, stiffness and strength of descending thoracic pig aorta. *J. Biomech.* **16**, 947–953 (1983).
291. Sommer, G., Gasser, T. C., Regitnig, P., Auer, M. & Holzapfel, G. A. Dissection properties of the human aortic media: an experimental study. *J. Biomech. Eng.* **130**, 1–12 (2008).
292. Tong, J., Sommer, G., Regitnig, P. & Holzapfel, G. A. Dissection properties and mechanical strength of tissue components in human carotid bifurcations. *Ann. Biomed. Eng.* **39**, 1703–1719 (2011).
293. Pasta, S., Phillippi, J. A., Gleason, T. G. & Vorp, D. A. Effect of aneurysm on the mechanical dissection properties of the human ascending thoracic aorta. *J. Thorac. Cardiovasc. Surg.* **143**, 460–467 (2012).
294. Tong, J., Schriefl, A. J., Cohnert, T. & Holzapfel, G. A. Gender differences in biomechanical properties, thrombus age, mass fraction and clinical factors of abdominal aortic aneurysms. *Eur. J. Vasc. Endovasc. Surg.* **45**, 364–372 (2013).
295. Zhang, Y., Hermanson, M. E. & Eddinger, T. J. Tonic and phasic smooth muscle contraction is not regulated by the PKC α - CPI-17 pathway in swine stomach antrum and fundus. *PLoS One* **8**, e74608 (2013).
296. Seydewitz, R., Siebert, T. & Böl, M. On a three-dimensional constitutive model for history effects in skeletal muscles. *Biomech. Model. Mechanobiol.* **18**, 1665–1681 (2019).
297. Parekh, A. *et al.* Ex vivo deformations of the urinary bladder wall during whole bladder filling: contributions of extracellular matrix and smooth muscle. *J. Biomech.* **43**, 1708–1716 (2010).
298. Ali, F., Paré, P. D. & Seow, C. Y. Models of contractile units and their assembly in smooth muscle. *Can. J. Physiol. Pharmacol.* **83**, 825–831 (2005).
299. Gunst, J. Effect of length history on contractile of canine tracheal smooth muscle. *Am. Physiol. Soc.* **250**, C146–C154 (1986).
300. Abbott, B. C. & Aubert, X. M. The force exerted by active striated muscle during and after change of length. *J. Physiol.* **117**, 77–86 (1952).
301. Rode, C., Siebert, T. & Blickhan, R. Titin-induced force enhancement and force depression: A ‘sticky-spring’ mechanism in muscle contractions? *J. Theor. Biol.* **259**, 350–360 (2009).
302. Herzog, W., Schappacher, G., DuVall, M., Leonard, T. R. & Herzog, J. A. Residual force enhancement following eccentric contractions: a new mechanism involving titin. *Physiology* **31**, 300–312 (2016).
303. Chi, R. J., Olenych, S. G., Kim, K. & Keller, T. C. S. Smooth muscle α -actinin interaction with smitin. *Int. J. Biochem. Cell Biol.* **37**, 1470–1482 (2005).

304. Rode, C., Siebert, T., Tomalka, A. & Blickhan, R. Myosin filament sliding through the Z-disc relates striated muscle fibre structure to function. *Proc. R. Soc. B Biol. Sci.* **283**, 20153030 (2016).







7 Author Contributions

All authors listed below hereby certify that





- 1 they meet the criteria of co-authorship by having sufficiently participated in the conception, conduct or interpretation of the results of relevant research and its publication;
- 2 they assume responsibility for their respective contribution to the publication towards third parties;
- 3 that there are no other individuals who qualify for authorship other than the ones mentioned;
- 4 potential conflicts of interest have been disclosed to funding organizations, the publication bodies and the heads of the responsible academic units;
- 5 they agree that their contribution may be published as part of the dissertation.

Contribution Statement




Doctoral student	Mischa Borsdorf
Publication title I	Locational and directional dependencies of smooth muscle properties in pig urinary bladder
Publication medium	Frontiers in Physiology – Renal and Epithelial Physiology

Doctoral student's name	Specification of the author's contribution to the publication	Date and signature
Mischa Borsdorf	Performed the experiments on biomechanical properties; analyzed the data and interpreted the results; prepared the figures; drafted the first version of the manuscript; edited, revised and approved the final version of manuscript	06.10.21 
Co-author's name, Institution	Specification of the author's contribution to the publication	Date and signature
André Tomalka, University of Stuttgart	Conceived and designed the experiments; performed the experiments on biomechanical properties; analyzed the data and interpreted the results; drafted the manuscript; edited, revised and approved the final version of manuscript	15.07.21 
Norman Stutzig, University of Stuttgart	Analyzed the data and interpreted the results; drafted the manuscript; edited, revised and approved the final version of manuscript	04.10.21 
Enrique Morales- Orcajo, Braunschweig University of Technology	Performed the histochemical analysis; edited, revised and approved the final version of manuscript	20.07.21 
Markus Böl, Braunschweig University of Technology	Conceived and designed the experiments; edited, revised and approved the final version of manuscript	16.07.21 
Tobias Siebert, University of Stuttgart	Conceived and designed the experiments; analyzed the data and interpreted the results; drafted the manuscript; edited, revised and approved the final version of manuscript	14.07.21 

Doctoral student	Mischa Borsdorf
Publication title II	On a coupled electro-chemomechanical model of gastric smooth muscle contraction
Publication medium	Acta Biomaterialia

Doctoral student's name	Specification of the author's contribution to the publication	Date and signature
Mischa Borsdorf	Conducted, described, and analyzed the active and passive experiments; drafted the manuscript; edited and approved the final version of manuscript	06.10.21 
Co-author's name, Institution	Specification of the author's contribution to the publication	Date and signature
Lisa Klemm, Braunschweig University of Technology	Described the theoretical background; prepared the figures, modeled and identified the parameters; constructed the stomach geometry and performed simulations; described and discussed the results from simulations; drafted the manuscript; edited and approved the final version of manuscript	01.08.21 
Robert Seydewitz, Braunschweig University of Technology	Modeled and identified the parameters; drafted the manuscript; edited and approved the final version of manuscript	28.07.21 
Markus Böl, Braunschweig University of Technology	Described the theoretical background; prepared the figures; discussed the results; coordinated the study; drafted the manuscript; edited and approved the final version of manuscript	16.07.21 
Tobias Siebert, University of Stuttgart	Conducted, described, and analyzed the active and passive experiments; drafted the manuscript; edited and approved the final version of manuscript	14.07.21 

Doctoral student	Mischa Borsdorf
Publication title III	Influence of layer separation on the determination of stomach smooth muscle properties
Publication medium	Pflüger's Archiv - European Journal of Physiology

Doctoral student's name	Specification of the author's contribution to the publication	Date and signature
Mischa Borsdorf	Wrote the first version of the paper, conducted the experiments, analyzed the data	06.10.21 
Co-author's name, Institution	Specification of the author's contribution to the publication	Date and signature
Markus Böl, Braunschweig University of Technology	Reviewed, edited, coordinated the study	16.07.21 
Tobias Siebert, University of Stuttgart	Designed and coordinated the study, wrote the paper.	14.07.21 

8 Acknowledgements

I hereby thank Prof. Dr. Tobias Siebert, the supervisor of this thesis. Having mentored me already throughout my bachelor and master's education and now my doctoral promotion, he constantly supported me and taught me the skill and knowledge to complete this doctoral degree. I am grateful for the opportunities he provides for me, for his friendship, and for the privilege to continuously learn from him.

I would like to thank my co-authors and my co-workers, who became dear friends in the years we've been working together and from whom I could always seek advice. I hereby particularly thank Dr. André Tomalka and Dr. Norman Stutzig. They already excellently taught me during my days as an undergraduate student, and still give me great instructions and consultation with their large know-how and competence.

Thank You to the facility managers, to whom I could always come for help on various projects, as well as for some shared conversations and laughs together. Thereby, I especially thank Joseph Lopez, Ruzhdi Bylygbashi and the late Armin Kamm who sadly passed away, recently. They were already working at the institute, when I began my bachelor's degree and played a substantial part of why I've come to love it here so much.

Thank You to my parents, Helga and Heiner, for their endless support and trust in me. Without them, I would have never been able to accomplish as much in my life.

Thank You to my big brothers, Mario and Moritz, and my larger family, as they are a huge and important part of my life.

Thanks to my all my friends, particularly my closest friends Tobias Jetter, Florian Pernau, and Jonas Kraft, with whom I try to spend as much time as possible.

I dedicate this thesis to my grandmother, Theresia "Resel" Braun, who sadly passed away recently, but surely will be there at my doctoral graduation, smiling happily as I'm finally dressed properly.

9 Declaration

Declaration of Authorship

I hereby declare that this dissertation is solely my own work except where otherwise indicated. Passages and ideas from other sources have been identified as such and properly acknowledged.

Erklärung über die Eigenständigkeit der Dissertation

Ich versichere, dass ich die vorliegende Arbeit selbständig verfasst und keine anderen als die angegebenen Quellen und Hilfsmittel benutzt habe; aus fremden Quellen entnommene Passagen und Gedanken sind als solche kenntlich gemacht.

Name/Name: Mischa Borsdorf

Signature/Unterschrift: 

Datum/Date: 12.10.21